

# **DIFFUSION KINETICS FOR DRUG RELEASE AND FOOD PRESERVATION**



DISSERTATION

Submitted to the Graduate Faculty

In Partial Fulfilment of the Requirements for the

Degree of **Doctor of Philosophy** in the

Department of Materials Science and Engineering

African University of Science and Technology, Abuja, Nigeria

By:

**AINA TOYIN (ID No. 70174 B)**

October, 2022

**PhD Supervisor:**

Prof. Winston Soboyejo, Chair (Worcester Polytechnic Institute, MA, USA)

**PhD Dissertation Committee:**

Dr. Shola O. Odusanya (SHESTCO, Abuja, Nigeria)

Prof. Ali A. Salifu (Worcester Polytechnic Institute, MA, USA)

Prof. John D. Obayemi (Worcester Polytechnic Institute, MA, USA)

Dr. Abdulhakeem Bello (African University of Science and Technology, Abuja, Nigeria)

Dr. Madukwe Johnathan (National Hospital, Abuja, Nigeria)

DIFFUSION KINETICS FOR DRUG RELEASE AND FOOD PRESERVATION

By:

Aina Toyin

A THESIS APPROVED BY THE MATERIALS SCIENCE AND ENGINEERING  
DEPARTMENT

RECOMMENDED:  27-10-2022

.....  
**Supervisor, Professor Winston Oluwale Soboyejo**

 27-10-2022  
.....

**Committee Member: Dr. O. Shola Odusanya**

 29-10-2022  
.....

**Committee Member: Prof. Ali A. Salifu**

 29-10-2022  
.....

**Committee Member: Prof. John D. Obayemi**

 27-10-2022  
.....

**Committee Member: Dr. Abdulhakeem Bello**

 27-10-2022  
.....

**Committee Member: Dr. Madukwe Johnathan**

 27/10/2022  
.....

**Head, Department of Materials Science and Engineering: Dr. Vitalis C. Anye**

 29/10/2022  
.....

**Acting President: Professor Azikiwe Peter Onwualu**

Date: .....

Copyright by Aina Toyin, © October 2022.

**All Right Reserved**

## **Dedication**

To my late parents Mr Sunday Aina Asepo and Mrs Marion Modupe Aina, their sacrifice and effort will forever remain indelible in my heart because they strove, and supported me to ensure that I get to the zenith of my education.

## Abstract

This thesis presents silica nanoparticles for the controlled release of AMACR-conjugated doxorubicin for the inhibition of prostate cancer cell growth. Inorganic MCM-41 silica nanoparticles were synthesized, functionalized with phenylboronic groups (MCM-B), and capped with dextran (MCM-B-D). The nanoparticles were then characterized using Fourier-transform infrared spectroscopy (FTIR), scanning electron microscopy (SEM), transmission electron microscopy (TEM), zeta potential analysis, N<sub>2</sub> sorption, X-ray diffraction, and thermogravimetric analysis before exploring their potential for drug loading and controlled drug release. This was done using a model prostate cancer drug, doxorubicin (DOX), and a targeted prostate cancer biomarker to facilitate the localized delivery of the drug,  $\alpha$ -Methyl Acyl-CoA racemase (AMACR)-conjugated DOX, which attaches specifically to receptors that are overexpressed on the surfaces of prostate cancer cells. The kinetics of controlled drug release over 30 days was then studied using zeroth order, first order, second order, Higuchi, and the Korsmeyer-Peppas models, while the thermodynamics of drug release was elucidated by determining the entropy and enthalpy changes. The flux of the released DOX was also simulated using the COMSOL Multiphysics software package. Generally, the AMACR-conjugated DOX drug-loaded nanoparticles were more effective than the free DOX drug-loaded formulations in inhibiting the growth of prostate cancer cells (PC-3 cell line) *in vitro* over a 96-h period. Furthermore, the effectiveness of DOX-A cancer drug for the targeted treatment of prostate cancer was explored *in vivo*. AMACR-conjugated drug (AMACR-doxorubicin) and free doxorubicin drug injections into groups of 4-week-old athymic male nude mice were discovered to target and shrink tumors without any apparent cytotoxicity, as shown by *ex vivo* toxicity histopathology studies. Our findings demonstrate that prostate cancer cells/tumors with overexpressed AMACR receptors act as binding sites

for AMACR-conjugated drugs, which in both *in vitro* and *in vivo* tests prevented the growth of prostate cells/tumors. The ability to restrain the growth of prostate cancer cells/tumors effects are due to the adhesive contacts between the overexpressed AMACR receptors on the prostate cancer cells/tumors and the AMACR molecular recognition units on the drug doxorubicin, DOX and DOX-A. The implications of the results are then discussed for the development of drug-eluting structures for the localized and targeted treatment of prostate cancer.

The second phase of the work, presents the release kinetics (RK) of a fungicidal antimicrobial agent (AMA), potassium sorbate (PS), that prolongs the shelf life of packaged food. The effects of PS release are explored on peanuts and fresh bread to determine the effects of PS on *Aspergillus niger* (*A. niger*) microbial growth. The *A. niger* was cultured in a potato dextrose agar (PDA) medium to obtain AMA activity on the film. AMA activity of PS incorporated into cellulose acetate (CA) based film was tested on peanuts and fresh bread for an extended period of time. The RK of PS from the films was obtained by studying the deswelling properties of PS loaded film at room temperature (24°C) and at elevated temperature (37°C). The diffusion coefficients of PS released through the film network were obtained to be between  $8.32 \times 10^{-10}$  to  $7.3 \times 10^{-7}$  m<sup>2</sup>/s. The release exponents (n) of PS from the film occurred by anomalous transport with n values ranging from 0.13 to 0.16 at 24°C and 0.5 to 0.89 at 37°C. The average flux released from the CA film was consistent with the percentage PS release from the CA film showing that modelling the effective diffusion of PS from a porous media is feasible. The released PS was potent enough to inhibit the growth of *A. niger* for a week then over a period of 2 years. Thereafter, the implications of the results in designing smart food packaging for enhanced food preservation were discussed

**Keywords:** functionalized, kinetics, Doxorubicin, mesoporous, biomaterial, tumorigenic,  $\alpha$ -Methyl Acyl-CoA racemase, potassium sorbate, cellulose acetate, fungicidal anti-microbial agent, swelling, *Aspergillus niger*

## Table of Contents

All Right Reserved .....	iii
Dedication .....	iv
Abstract.....	v
Table of Contents.....	vii
Acknowledgements.....	xi
Publications in PhD focus.....	xii
Other publications and conference presentations .....	xiii
List of figures.....	xiv
List of tables .....	xviii
CHAPTER ONE .....	1
1.0. Background and Introduction to prostate cancer.....	1
1.1. Introduction .....	1
1.2. Prostate cancer statistics .....	2
1.3 Cancer Drugs .....	4
<b>1.3.1 Nanoparticles used in cancer drug delivery.....</b>	<b>4</b>
1.4 Mechanisms of mass transport.....	5
1.5 Scope of the projects .....	7
<b>1.5.1 Prostate cancer research .....</b>	<b>7</b>
1.6 Bibliography .....	8
CHAPTER TWO .....	11
2.0. Background and introduction to food preservation .....	11
2.1. Introduction .....	11
<b>2.1.1 Boiling: .....</b>	<b>12</b>
<b>2.1.2 Canning:.....</b>	<b>12</b>
<b>2.1.3 Burial: .....</b>	<b>12</b>
<b>2.1.4 Confit: .....</b>	<b>12</b>
<b>2.1.5 Cooling:.....</b>	<b>12</b>
<b>2.1.6 Curing: .....</b>	<b>12</b>
<b>2.1.7 Hurdle technology:.....</b>	<b>12</b>
<b>2.1.8 Non-thermal plasma: .....</b>	<b>13</b>
<b>2.1.9 High-pressure food preservation: .....</b>	<b>13</b>

<b>2.1.10 Pulsed electric field electroporation (PEF):</b> .....	13
2.2 Wasted food.....	13
2.3 Food preservatives.....	14
2.4 Mechanisms of mass transport.....	15
2.5 Scope of the projects.....	16
<b>2.5.1 Food preservation</b> .....	16
2.6 Bibliography.....	17
CHAPTER THREE.....	21
3.0 Literature review.....	21
3.1 Targeted drug release.....	21
<b>3.1.1. Active passive targeting</b> .....	22
<b>3.1.2. Nanotechnology</b> .....	23
<b>3.1.3. Biomarkers for prostate cancer</b> .....	24
<b>3.1.4 Prostate cancer targeted drug delivery</b> .....	25
3.2 Food preservation.....	26
<b>3.2.1. Food spoilage: mechanism</b> .....	27
<b>3.2.1.1. Physical spoilage</b> .....	27
<b>3.2.1.2 Microbial spoilage</b> .....	29
<b>3.2.1.3 Chemical spoilage</b> .....	29
3.3 Effectiveness of antimicrobial food packaging.....	30
3.4 Antimicrobial packaging.....	31
3.5 Antimicrobial agents.....	33
3.6 Bibliography.....	36
CHAPTER FOUR.....	40
4.0 Sustained Release of AMACR Antibody-Conjugated and Free Doxorubicin from Silica Nanoparticles for Prostate Cancer Cell Growth Inhibition.....	40
4.1. Introduction.....	40
4.2. Materials and methods.....	42
4.3. Materials.....	43
<b>4.3.1 Synthesis of MCM-41 silica nanoparticles</b> .....	43
<b>4.3.2. Synthesis of phenylboronic acid-functionalized MCM-41 silica nanoparticles:</b> .....	44
<b>4.3.3. Conjugation of doxorubicin with AMACR peptide</b> .....	45
<b>4.3.4. Preparation of drug-loaded silica nanoparticles</b> .....	46
<b>4.3.5. Characterization of the nanoparticles</b> .....	47
4.4 <i>In Vitro</i> drug release.....	48
4.5. Modeling of drug release.....	49

<b>4.5.1 <i>In vitro</i> drug release kinetics</b> .....	49
<b>4.5.2. <i>In vitro</i> drug release thermodynamics</b> .....	51
4.6 <i>In vitro</i> cell viability .....	52
<b>4.6.1 Immunofluorescence staining of AMACR receptors</b> .....	54
<b>4.6.2. Drug release simulations</b> .....	54
<b>4.6.3. Statistical analysis</b> .....	56
4.7. Results.....	56
<b>4.7.1. Physicochemical properties of the silica nanoparticles</b> .....	56
<b>4.7.2. Drug release from the nanoparticle formulations</b> .....	63
<b>4.7.3. Simulation of drug release</b> .....	68
4.8. Viability of prostate cancer cells .....	70
4.9. Discussion.....	72
4.10. Conclusions .....	81
4.11 Bibliography .....	82
CHAPTER FIVE .....	87
5.0 AMACR-Conjugated Drug as Targeted Therapeutic Agents for the Specific Targeting and Localized Treatment of Prostate Cancer Cells (PC-3) .....	87
5.1 Introduction .....	87
5.2 Materials and Methods.....	90
<b>5.2.1 Materials</b> .....	90
<b>5.2.2 Methods</b> .....	91
<b>5.2.2.1 Conjugation of doxorubicin with AMACR peptide</b> .....	91
<b>5.2.2.2 FTIR Investigation</b> .....	91
<b>5.2.2.3 UV-Vis</b> .....	92
<b>5.2.2.4 Cell culture</b> .....	93
<b>5.2.2.5 <i>In vitro</i> cell viability</b> .....	93
<b>5.2.2.6 Flow cytometry</b> .....	95
<b>5.2.3 <i>In vivo</i> Tumor Development and Targeted Drug Delivery</b> .....	96
<b>5.2.4 Studies on toxicity, histopathology, and electron microscopy</b> .....	97
<b>5.2.5 AMACR Receptor Staining and <i>In vitro</i> cell viability</b> .....	99
<b>5.2.6 Immunofluorescence Staining</b> .....	100
<b>5.2.7 Studies on toxicity, histopathology, and electron microscopy</b> .....	101
5.3 Results.....	102
<b>5.3.1 Results of IHC, IF, drug conjugation and characterization</b> .....	102
<b>5.3.2 <i>In vitro</i> cell viability</b> .....	103
<b>5.3.3 Result of tumor growth and shrinking <i>in vivo</i></b> .....	105

5.4 Implications of the results .....	106
5.5 Statistical analysis .....	108
5.6 Conclusion .....	108
5.8 Bibliography .....	110
CHAPTER SIX.....	113
6.0 Release kinetics of fungicidal antimicrobials into packaged foods.....	113
6.1 Introduction .....	113
6.2 Materials and methods.....	116
<b>6.2.1 Materials</b> .....	116
<b>6.2.2 Methods</b> .....	116
<b>6.2.3 Preparation of Cellulose Acetate (CA) Film</b> .....	116
<b>6.2.4 Characterization of the films</b> .....	117
<b>6.2.5 Release tests</b> .....	117
<b>6.2.6 Preparation of potato dextrose agar (PDA)</b> .....	118
<b>6.2.7 Morphology of Aspergillus niger (A. niger)</b> .....	120
<b>6.2.8 Preparation of test organism</b> .....	120
<b>6.2.8.1 Determination of number of <i>A. niger</i> spores</b> .....	121
<b>6.2.8.2 Test of zone of inhibition</b> .....	121
6.3 Modelling antimicrobial release mechanism from films .....	121
<b>6.3.1 Modelling the effect of diffusion from the porous film</b> .....	122
<b>6.3.2 Summary of the simulation</b> .....	124
6.4 Result and Discussion.....	126
<b>6.4.1 Film Microstructure and Morphology</b> .....	126
<b>6.4.2 Potassium sorbate release</b> .....	127
<b>6.4.3 Antimicrobial effects</b> .....	131
6.5 Implication .....	131
6.6 Bibliography .....	133
CHAPTER SEVEN.....	137
7.0 Perspectives and conclusions .....	137
7.1 Recommendations for future work .....	138
<b>7.1.1 Application of AMACR conjugated doxorubicin to treat colon cancer</b> .....	138
<b>7.1.2 Application of AMACR conjugated doxorubicin to treat glioblastoma</b> .....	139
<b>7.1.3 Application of polymer based antimicrobial agent in food preservation</b> .....	140

## **Acknowledgements**

I am particularly appreciative of the Pan-African Materials Institute (PAMI), which is one of the World Bank's African Centers of Excellence Projects. P126974), for the monetary assistance. The African University of Science and Technology (AUST), the Kogi state government, and the Nelson Mandela Institute (NMI) are also acknowledged by the writers for the scholarships they provided to me. I am grateful to Prof. Wole Soboyejo, Dr. Shola Odusanya, Prof. A. A. Salifu, and Prof. J. D. Obayemi of my PhD Dissertation Committee for their support and direction. The Biomedical Research Group at the African University of Science and Technology, Abuja, Nigeria, as well as the Chemistry and Physics of Materials Unit (CPMU) at the Jawarharlal Nehru Center for Advanced Scientific Research (JNCASR), India, and the life sciences and bioengineering center (LSBC) at Worcester Polytechnic Institute (WPI), deserve my sincere gratitude for allowing me to use their labs to complete my research. I also appreciate the Global Fellowship fund for the research Fellowship since it enabled me to finish my PhD research.

Last but not the least, I want to express my gratitude to my wife, Victoria Motunrayo Toyin for her support and inspiration throughout my PhD studies.

## **Publications in PhD focus**

**T. Aina**, A. A. Salifu, S. Kizhakkepura, Y. Danyuo, J. D. Obayemi, J. C. Oparah, T. C. Ezenwafor, K. C. Onwudiwe, C. J. Ani, S. S. Biswas, C. Onyekanne, O. S. Odusanya, J. Madukwe, and W. O. Soboyejo; “Sustained release of AMACR antibody-conjugated and free doxorubicin from silica nanoparticles for prostate cancer cell growth inhibition” Publisher (Wiley); Journal of Biomedical Materials Research - Part B, Applied Biomaterials, (2022) First published: 31<sup>st</sup> October, 2022, <https://doi.org/10.1002/jbm.b.35185>

1.

2. **T. Aina**, J. Oparah, J. D. Obayemi, S. Dozie-Nwachukwu, C. D. Onodugo, C. J. Ani, O. Odusanya, W. O. Soboyejo; “Release kinetics of fungicidal antimicrobials into packaged foods”. Publisher (Wiley); Journal of Food Safety (JFS), (2021) first published, 29<sup>th</sup> April 2021, <https://doi.org/10.1111/jfs.12904>

### **Other publications and conference presentations**

1. C. E. Onyekanne, O. K. Oyewole, A. A. Salifu, J. D. Obayemi, V. C. Anye, C. C. Nwazojie, K. C. Onwudiwe, J. C. Oparah, **T. Aina**, C. C. Ezeala, T. C. Ezenwafor, O. S. Odusanya, W. O. Soboyejo; “Mechanical and thermal properties of polydimethylsiloxane/magnetite nanocomposites for cancer treatment by localized hyperthermia and Photothermal ablation”. (John Wiley & Sons, Inc.); Journal of Applied Polymer Science, Vol. 139 (2022), Issue 30, Pages e52669, first published: 26<sup>th</sup> May 2022. <https://doi.org/10.1002/app.52667>
2. K. Onwudiwe, J. D. Obayemi, J. Hu, J. Oparah, C. Onyekanne, C. Nwazojie, **T. Aina**, V. Uzonwanne, A. Salifu, W. Soboyejo; “Investigation of creep properties and the cytoskeletal structures of non-tumorigenic breast cells and triple-negative breast cancer cells” (John Wiley & Sons, Inc.); Journal of Biomedical Materials Research Part A, Volume 110, Issue 5, first published: 29 December 2021, <https://doi.org/10.1002/jbm.a.37348>
3. **T. Aina**, J. C. Oparah, A. A. Salifu, J. D. Obayemi, K. C. Onwudiwe, C. J. Ani, O. S. Odusanya, W. O. Soboyejo Synthesis of Nano-Biomaterial and the Study of the Kinetics of Localized Cancer Drug Release from Silica Based Nanoparticles; November 2021, MRS 2021 Fall poster presentation (Boston) USA.

## List of figures

Figure 1.1: Prostate cancer, 3D illustration showing normal prostate gland and presence of tumor inside prostate gland which compresses urethra. (Picture by: Kateryna Kon / Shutterstock) .....	1
Figure 1.2: Most common type of cancer mortality by country in 2020 among men, with the numbers of countries represented in each ranking group being included in the legend. Source: GLOBOCAN 2020 .....	2
Figure 1.3: Incidence and mortality age-standardized rates in high/very high human development index (HDI) countries versus low/medium HDI countries among men in 2020. The 15 most common cancers in the world are shown in descending order of the overall age-standardized rate. Source: GLOBOCAN 2020 .....	3
Figure 1.4: Number of new cases of cancers in 2020, males, all ages .....	4
Figure 3.1: Scheme of nanoparticles based targeted drug delivery .....	5
Figure 3.2: Schematic of passive tissue targeting and active cellular delivery of anticancer medicines to tumors utilizing nanocarriers .....	6
Figure 3.3: Nanocarriers that are often used in drug delivery applications .....	7
Figure 4.1: A schematic showing the steps of silanizing the silica nanoparticles (MCM-41) with amino groups (MCM-N) and followed by phenylboronic acid functionalization (MCM-	

B) before loading them with cancer drugs (DOX and DOX-A) and then capping the MCM-B nanoparticles with dextran .....8

Figure 4.2: (a) FTIR spectra of the nanoparticles (b) TGA analysis of the nanoparticles .....9

Figure 4.3: Nitrogen sorption analysis of the nanoparticles, showing the (a) nitrogen adsorption and desorption isotherms and (b) the Barret-Joyner-Halenda pore size distribution curves of the nanoparticles .....10

Figure 4.4: The XRD patterns of the nanoparticles .....11

Figure 4.5: The morphology and elemental analysis of the silica nanoparticles, showing (a), (b) the FE-SEM micrographs of MCM-B nanoparticles. The presence of nitrogen and boron in the EDS spectrum in (c) confirms the possible functionalization of the silica nanoparticles with amino and phenylboronic acid, respectively and (d), (e) the FE-SEM micrographs of the MCM -B-D nanoparticles .....12

Figure 4.6: High-resolution transmission electron micrographs of (a) MCM-B nanoparticles before capping with dextran and (b) MCM-B-D nanoparticles (after capping the MCM-B nanoparticles with dextran) .....13

Figure 4.7: Cumulative AMACR-conjugated drug release from MCM-41-DOX-A, MCM-B-DOX-A and MCM-B-D-DOX-A of DOX-A nanoparticles in a buffer of pH 6.5 at (a) 37°C (b) 41°C (c) 44°C, and in a buffer of pH 7.4 at (d) 37°C (e) 41°C (f) 44°C. Furthermore, the cumulative drug release from MCM-41-DOX, MCM-B-DOX and MCM-B-D-DOX of DOX nanoparticles in a buffer of pH 6.5 at (g) 37°C (h) 41°C (i) 44°C, in a buffer at pH 7.4 at (j) 37°C (k) 41°C (l) 44°C .....14

Figure 4.8: (a) Average flux of the drugs through the multiple pores of the nanomaterial over a 30-day period and (b) Time-dependent transport of diluted species from the concentration boundary to the left down to the flux boundary to the right .....15

Figure 4.9: Confocal fluorescence images showing the expression AMACR receptors (green stains) from human prostate cancer cells (PC-3), showing (a) the blue staining of the nuclei of PC-3 cells (b) the green staining of the expressed AMACR receptors on the surfaces of the PC-3 cells and (c) the composite image .....16

Figure 4.10: The effects of the different drug-loaded nanoparticle formulations on the viability of prostate cancer cells treated with them, as measured by the percentage alamar blue reduction. The error bars represent the standard deviations for  $n = 3$  independent trials. \*  $p < 0.05$  .....17

Figure 4.11: Porous geometries used for the simulation: (a) multi-porous (b) horizontal pore alignment (c) vertical pore alignment (d) and (e) are both inclined at  $45^\circ$  to the horizontal.

Figure 5.1: FTIR spectra of AMACR, DOX and DOX-A drug.....11

Figure 5.2: UV-VIS spectra of DOX, DOX-A and AMACR dissolved in PBS pH7.4 .....12

Figure 5.3: Percentage (a) \*CGI for  $30\mu\text{M}$  (b) \*\*ABR for  $30\mu\text{M}$  (c) \*CGI for  $15\mu\text{M}$  (d) \*\*ABR for  $15\mu\text{M}$  drug (DOX and DOX-A). \*Cell Growth Inhibition; \*\*Alamar Blue Reduction .....13

Figure 5.4: Flow cytometry result showing the cell viability of PC-3 cell death in (a) control without drug (b) DOX treated PC-3 (c) DOX-A treated PC-3 (d) The apoptotic rates of PC-3 cells treated with DOX and DOX-A. Data are presented as means  $\pm$  SD ( $n = 3$ ).  $P < 0.05$  ..14

Figure 5.5: (a) PC3 cells (b) Overexpression of AMACR receptors (green) (c) Combined cells & AMACR stains (d) PNT-2 cells (e) Very low expression of AMACR receptors

(green) (f) Combined cells & AMACR stains  
 .....14

Figure 5.6. Optical micrograph of Immunohistochemistry staining of tissues at magnification of X40 (a) No expression of AMACR receptors on a benign prostatic hyperplasia (BPH) (b) Prostate tissue with overexpression of AMACR receptors (brown stains) .....15

Figure 5.7: Histopathological examination of tumour tissues and organs in PC-3 induced xenograft prostate tumour model mice after treatment (from 12-day treatment group) with unconjugated DOX and DOX-A drugs .....16

Figure 5.8: (a) Anti-tumour efficacy and tumour reduction in male athymic nude mice treated with two injections of DOX, DOX-A, and Saline over a 12-day trial period (b) percentage tumour shrinkage (n = 3, P<0.05) .....17

Figure 6.1: Optical micrograph of an *A. niger* .....18

Figure 6.2 (a) 3D CA porous structure with the gray colored portion as the surface that is accessible for diffusion. (b) 2D porous structure representing a segment of the surface of (a)

Figure 6.3: (a) Concentration flux in the 3D modelled CA porous film after 52 hr. (b) Surface concentration flux of a segment of the entire CA film in 2D after 72 min .....19

Figure 6.4: Generalized average flux at the flux boundary in the detailed 2D model (solid blue line) and the 1D homogenized approximation (dashed green line) .....20

Figure 6.5: Effect of cellulose acetate ratio on the pore sizes: (a) crystals of antimicrobial film, (b) 10% w/w Composition of CA, (c) 13% w/w Composition of CA and (d) 15% w/w Composition of CA .....21

Figure 6.6: Percentage release of potassium sorbate (PS) from 15 w/w% CA, 13 w/w% CA, and 10 w/w% CA .....22

Figure 6.6: Percentage release of potassium sorbate (PS) from 15 w/w% CA, 13 w/w% CA, and 10 w/w% CA .....23

Figure 6.7: (a) and (b) Presents linear fit plot of  $\ln\left(\frac{M_t}{M_i}\right)$  versus  $\ln(t)$ , for swelling and deswelling of antimicrobial film samples,  $M_{15}^+$ ,  $M_{13}^+$  and  $M_{10}^+$  respectively having antimicrobial agent added to it at room temperature 24°C, whereas, (c) and (d) was added at 37°C .....24

Figure 6.8: Zone of inhibition of CA film by the agar diffusion method .....25

**List of tables**

Table 3.1: Antimicrobial agents and packaging systems .....1

Table 4.1: A summary of the zeta potentials of the silica nanoparticles .....2

Table 4.2: The correlation coefficients ( $R^2$ ), the drug release exponents (n), and the diffusion coefficients (D) from the various drug-loaded silica nanoparticle formulations determined

from the drug release kinetic models  
.....3

Table 4.3: Thermodynamic parameters of MCM-41, MCM-B, and MCM-B-D nanoparticles loaded with doxorubicin (DOX) and doxorubicin conjugated with AMACR (DOX-A)  
.....4

Table 6.1: Types of films and their codes prepared at 24°C  
.....1

Table 6.2: (a) The values of the swelling and de-swelling ratios and the k, n, and D values of the antimicrobial films at room temperature 24°C. (b) The values of the swelling and de-swelling ratios and the k, n, and D values of the antimicrobial films at room temperature 37°C  
.....2

## CHAPTER ONE

### 1.0. Background and Introduction to prostate cancer

#### 1.1. Introduction

The prostate gland is a tiny gland located in the lower abdomen of a man. It surrounds the urethra and is placed beneath the bladder (Figure 1.1). The prostate gland generates seminal fluid, often known as semen, which is controlled by the hormone testosterone. During ejaculation, sperm-bearing semen exits the urethra [1].

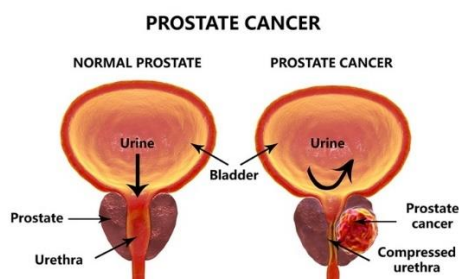


Figure 1.1: Prostate cancer: 3D illustration showing normal prostate gland and presence of tumor inside prostate gland which compresses urethra. (Picture by: Kateryna Kon / Shutterstock)

Prostate cancer occurs when an abnormal, malignant growth of cells known as a tumor arises in the prostate [2], [3]. This malignancy has the potential to spread to other parts of the body [4]. Because the cancer is made up of cells from the prostate in these circumstances, it is still referred to as prostate cancer. Prostate cancer was the second most common disease and the fifth major cause of cancer death among men in 2020, with an estimated 1.4 million new cases and 375,000 deaths worldwide[5]. Adenocarcinoma being the most common kind of PC [6] and PC could be aggressive or non-aggressive depending on the speed of growth. Some of the predisposing factors that may lead to PC includes but are not limited to old age, family history of prostate cancer, genetic mutations, obesity and race (e.g., men of African

descent are more predisposed to PC) are some of the factors that raises the likelihood of PC in men [7].

Hitherto, surgery, radiation therapy, cryotherapy, hormone therapy, chemotherapy, immune therapy and stereotactic radiosurgery are the known methods of treatment [8]. This research will focus on the aspect of chemotherapy and applying the knowledge of materials science to load the drug unto a nanomaterial and then control the drug delivery to the target site by conjugating it with molecular recognition units.

## 1.2. Prostate cancer statistics

The GLOBOCAN database conducted on 185 countries and 36 cancers by age and gender showed that in 2020, about 1,414,259 prostate cancer (PC) cases were recorded which amounts to 7.3% of the new cancer cases and about 375,304 deaths which amounts to 3.8% of deaths relative to the entire cancer cases globally [5], [9]. PC is also the most commonly diagnosed cancer among men in 112 nations [5]. Prostate cancer is the second leading cause of deaths in men in 48 countries, Figure 1.2.

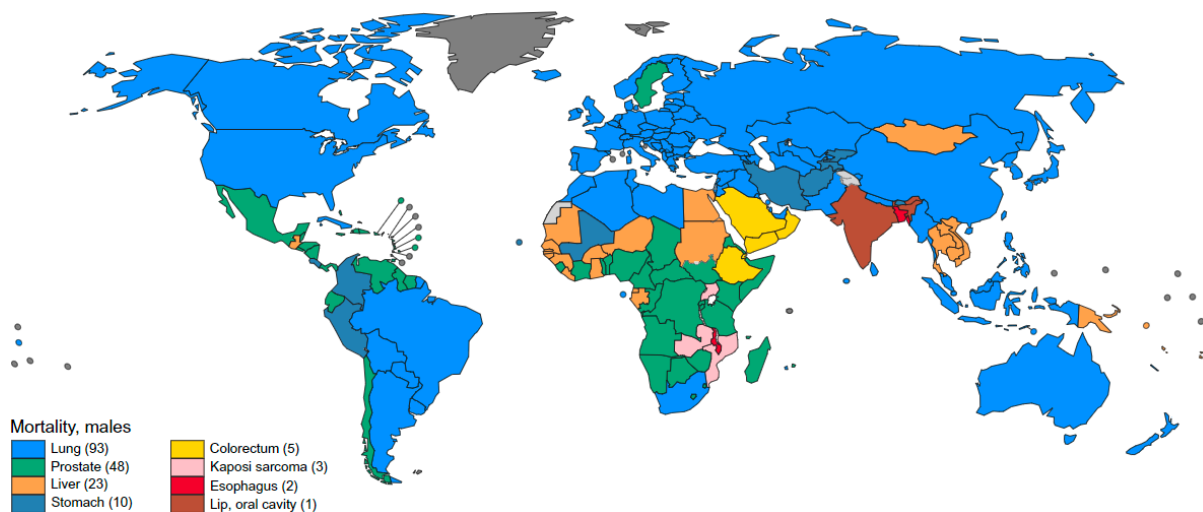


Figure 1.2: Most common type of cancer mortality by country in 2020 among men, with the numbers of countries represented in each ranking group being included in the legend. Source: GLOBOCAN 2020

In countries with a high human development index (HDI), prostate cancer mortality rate is the second being 37.5 per 100,000 after lung cancer (39 per 100,000). Whereas, in countries with low HDI the mortality rate of prostate cancer is the highest which is given as 11.3 per 100,000, Figure 1.3.

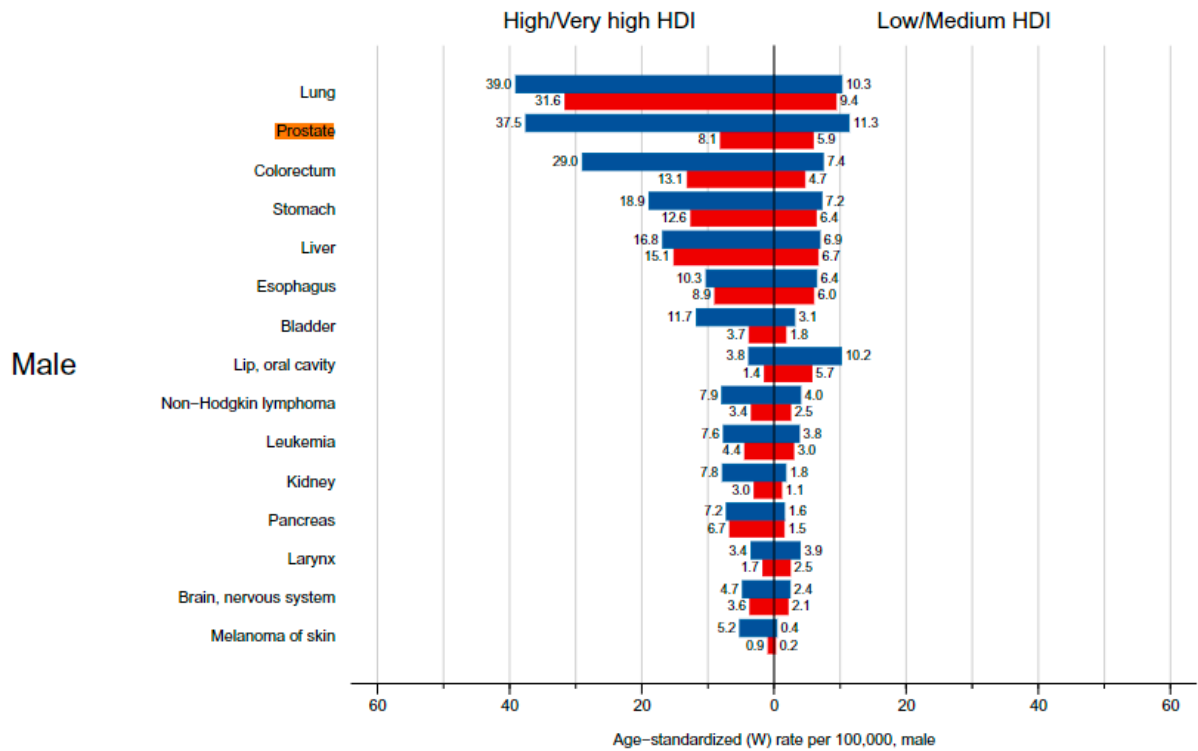


Figure 1.3: Incidence and mortality age-standardized rates in high/very high human development index (HDI) countries versus low/medium HDI countries among men in 2020. The 15 most common cancers in the world are shown in descending order of the overall age-standardized rate. Source: GLOBOCAN 2020.

The number of new cases of PC in Nigeria amounts to about 15,306 which is 12.3% of all the cancers in both sexes making it the second after breast cancer [10]. In males, PC takes first place among all the cancer reported in 2020, with about 15,306 new cases reported which amounts to 29.8% of all male cancers reported in Nigeria in 2020 [10] Figure. 1.4. Hence this statistical result provided the motivation for this project since Nigeria is in Africa and is classified under countries with low HDI.

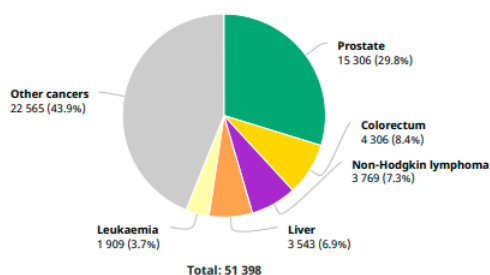


Figure 1.4: Number of new cases of cancers in 2020, males, all ages

### 1.3 Cancer Drugs

The Food and Drug Administration (FDA) has authorized the medications listed below for the treatment of prostate cancer. Generic and brand names are included in the list. Degarelix (degarelix for injection) [11], eligard (leuprolide acetate) [12], erleada (apalutamide)[13], jevtana (cabazitaxel) [14], lupro depot (leuprolide acetate for depot suspension) [15], lynparza (olaparib) [16], nubeqa (darolutamide) [17], orgovyx (relugolix) [18], provenge (sipuleucel-T) [19], rubraca (rucaparib) [20], trelstar (triptorelin pamoate) [18], xofigo (radium Ra 223 dichloride) [21], xtandi (enzalutamide) [22], zoladex (goserelin acetate implant) [23], zytiga (abiraterone acetate) [24] and Doxorubicin hydrochloride [25].

#### 1.3.1 Nanoparticles used in cancer drug delivery

A nanoparticle is a tiny particle with a diameter of 1 to 100 nanometres in size. Some of the treatment method involves the use of several kinds of nanoparticles as follows; a self-assembled simple nanoparticle approach for delivering siRNA to silence the Skp2 gene in vivo for cancer therapy. The nanoparticles, dubbed siSkp2/Que NPs, are made by self-assembly of siRNA targeting Skp2 (siSkp2) and the natural chemical quercetin (Que). The siSkp2/Que NPs offer a number of benefits: (a) carrier-free siRNA administration with rapid self-assembly and simple synthesis; (b) synergistic silencing effect with concomitant target degradation of Skp2 mRNA and protein; (c) efficient cellular internalization and tumor site

enrichment; and d) excellent biocompatibility and decreased toxicity [26]. In another work, a chemical precipitation approach was used to make superparamagnetic magnetite nanoparticle anchored on graphene oxide (GO/Fe<sub>3</sub>O<sub>4</sub>) nanoparticle hybrids with varied GO/Fe<sub>3</sub>O<sub>4</sub> ratios. Physical ultrasound and vibration are used to prepare magnetic drug microspheres (GO/Fe<sub>3</sub>O<sub>4</sub>-DXR). The temperature of suspensions containing GO/Fe<sub>3</sub>O<sub>4</sub>-DXR nanoparticles with different mass ratios of Fe<sub>3</sub>O<sub>4</sub> and GO (1:1, 1:1.5, 1:2) after 9 minutes in an AC magnetic field is 88.3°C, 70.6°C, and 54.9°C, respectively, which meets the temperature requirements of magnetic materials in medical applications. GO/Fe<sub>3</sub>O<sub>4</sub>-DXR nanocomposites can be employed as thermosteds in magnetic hyperthermia therapy (MHT) as well as for targeted treatment to release anti-cancer medicines. Cancer can be treated more precisely and effectively using a combination of hyperthermia and targeted therapy [27].

#### **1.4 Mechanisms of mass transport**

Usually, the regulation of molecule release involves two principal mass transport systems. The first and most noticeable one is internal mass transfer, also known as diffusion, within the material. The second one is external mass transfer, which involves moving material's mass toward an external medium (atmosphere, food simulant, or biological material (*in vitro/in vivo*)). When the solution is thoroughly churned around the device, diffusional mass transport is typically thought of as the major stage and is virtually always involved in the regulation of active species release (external mass transfer resistance becomes thus negligible). The apparent coefficient of diffusion, also known as diffusivity, shows the capacity of the migrant to disperse through the material and is commonly thought to depict this process according to Fick's law (equation 1.1 and 1.2). For simulating the release from two media in contact, a different mass transfer parameter is especially significant. The partition coefficient  $k$  describes how the migrant is split across the two mediums at equilibrium. It is a sign of migratory affinities for the subject of the inquiry. Along with mass

transport of active species, diffusion of the simulant in contact with the material may also be involved, leading to swelling and/or plasticization of the polymer/material in use. So, it can prevent the release from happening [28]. The efficacy of controlled release systems for pharmaceutical applications has been predicted using mathematical models that have been applied to simulating the release of active species from biocompatible material and some polymers of known geometries [29] such as Polydimethylsiloxane (PDMS) [30], [31] and bio composites films and microcapsules [32].

$$J = -D \frac{\partial C}{\partial x} \quad 1.1$$

$$\frac{\partial C}{\partial t} = D \frac{\partial^2 C}{\partial x^2} \quad 1.2$$

Where J is the flux (moles/area/time), D is the diffusion coefficient/diffusivity, and C is the concentration. Equation 1.1 illustrates Fick's first law (one dimensional diffusion). Contrarily, when concentration varies over time, equation 1.2 reflects Fick's second law. utilizing the power law or Peppas equation, equation 1.3 is a well-liked and straightforward empirical model for describing the release of drugs and active compounds [33].

$$\frac{m_t}{m_\infty} = kt^n \quad 1.3$$

At time t and infinite time, respectively,  $m_t$  and  $m_\infty$  represent the absolute cumulative quantity of drug/active species released;  $k$  is a constant combining the structural and geometric properties of the system; and n is the release exponent, reflecting the method of release.

The mathematical value of n and the structure of the system provide details on the ensuing release mechanism. In terms of slab geometry alone, equation (1.3) has two distinct physical implications for  $n = 0.5$  and  $n = 1$ . For  $n = 1$ , the system presents a way for controlled molecule release. The equation makes reference to a Fickian diffusion and a diffusion-controlled drug release mechanism when  $n = 0.5$  [34]. Since diffusional mass movement is

commonly considered of as the major component of the release mechanism, the release of active species intended for use in biological systems is most frequently studied using these types of models. Zero-order, first-, second-, and Higuchi models are further models. The initial and boundary conditions that are given, along with the specific geometry of the device under investigation, allow for the solution of Fick's second law-based models [28].

## **1.5 Scope of the projects**

### **1.5.1 Prostate cancer research**

- a) To decrease the pore diameters of silica nanoparticles in order to limit the in vitro release of the prostate cancer medications DOX and DOX-A, as well as to identify the kinetics and thermodynamic parameters of drug release from the drug-loaded nanoparticles. Both the dextran-capped and uncapped nanoparticles will go through these procedures.
- b) Doxorubicin conjugated to AMACR will be examined as a representative cancer treatment in this research. By conjugating doxorubicin hydrochloride and cysteine AMACR, the synthesis will be completed and the result characterized. Using the PC-3 PC cell line and an athymic nude mouse model that has been generated with PC xenograft tumors, the effect of the AMACR-conjugated medication will be examined on cancer cells and tissues in vitro. It will be investigated whether the conjugated medication may target and reduce PC xenograft tumors over a period of twelve days throughout the progression of the prostate cancer.

## 1.6 Bibliography

- [1] R. W. Cotton and M. B. Fisher, “Review: Properties of sperm and seminal fluid, informed by research on reproduction and contraception,” *Forensic Science International: Genetics*, vol. 18. pp. 66–77, 2015, doi: 10.1016/j.fsigen.2015.03.009.
- [2] D. J. Grignon, “Unusual subtypes of prostate cancer,” *Springer Nat.*, vol. 17, p. 12, 2004, doi: 10.1038/modpathol.3800052.
- [3] I. Mitsogiannis, L. Tzelves, A. Dellis, H. Issa, A. Papatsoris, and M. Moussa, “Prostate cancer immunotherapy,” <https://doi.org/10.1080/14712598.2022.2027904>, 2022, doi: 10.1080/14712598.2022.2027904.
- [4] S. H. Hussain, C. S. Huertas, A. Mitchell, A. L. Deman, and E. Laurenceau, “Biosensors for circulating tumor cells (CTCs)-biomarker detection in lung and prostate cancer: Trends and prospects,” *Biosens. Bioelectron.*, vol. 197, p. 113770, Feb. 2022, doi: 10.1016/J.BIOS.2021.113770.
- [5] H. Sung *et al.*, “Global Cancer Statistics 2020: GLOBOCAN Estimates of Incidence and Mortality Worldwide for 36 Cancers in 185 Countries,” *CA. Cancer J. Clin.*, vol. 71, no. 3, pp. 209–249, 2021, doi: 10.3322/caac.21660.
- [6] P. T. Scardino, R. Weaver, and M. A. Hudson, “Early detection of prostate cancer,” *Hum. Pathol.*, vol. 23, no. 3, pp. 211–222, Mar. 1992, doi: 10.1016/0046-8177(92)90102-9.
- [7] A. Barsouk *et al.*, “Epidemiology, Staging and Management of Prostate Cancer,” *Med. Sci. 2020, Vol. 8, Page 28*, vol. 8, no. 3, p. 28, Jul. 2020, doi: 10.3390/MEDSCI8030028.
- [8] M. J. Connor *et al.*, “Additional Treatments to the Local tumour for metastatic prostate cancer-Assessment of Novel Treatment Algorithms (IP2-ATLANTA): protocol for a multicentre, phase II randomised controlled trial,” *BMJ Open*, vol. 11, no. 2, p. e042953, Feb. 2021, doi: 10.1136/BMJOPEN-2020-042953.
- [9] P. Hyuna Sung, PhD; Jacques Ferlay, MSc, ME; Rebecca L. Siegel, MPH; Mathieu Laversanne, MSc; Isabelle Soerjomataram, MD, MSc, PhD; Ahmedin Jemal, DMV, PhD; Freddie Bray, BSc, MSc, “(No Title),” *Cancer J.*, vol. 71, p. 41, 2021, doi: 10.3322/caac.21660.
- [10] IARC, “International Agency for Research on Cancer, in collaboration with World Health Organisation, Source: Globocan 2020,” 2021.
- [11] L. Klotz *et al.*, “Title: The efficacy and safety of degarelix: a 12-month, comparative, randomized, open-label, parallel-group phase III study in patients with prostate cancer,” *BJU Int.*, p. 9, 2008, doi: 10.1111/j.1464-410X.2008.08183.x.
- [12] “Eligard (leuprolide acetate) | CenterWatch.” [Online]. Available: <https://www.centerwatch.com/directories/1067-fda-approved-drugs/listing/3441-eligard-leuprolide-acetate>. [Accessed: 01-Mar-2022].

- [13] “Erleada (apalutamide) | CenterWatch.” [Online]. Available: <https://www.centerwatch.com/directories/1067-fda-approved-drugs/listing/3472-erleada-apalutamide>. [Accessed: 01-Mar-2022].
- [14] X. Shi *et al.*, “Synergistic nanoassemblies constructed from a STAT3 inhibitor and a cabazitaxel prodrug with enhanced cancer chemo-immunotherapy,” 2021, doi: 10.1016/j.mtnano.2021.100155.
- [15] W. Li, J. Tang, D. Lee, T. R. Tice, S. P. Schwendeman, and M. R. Prausnitz, “Clinical translation of long-acting drug delivery formulations,” *Nat. Rev. Mater.*, p. 15, 2022, doi: 10.1038/s41578-021-00405-w.
- [16] U. A. Degboe *et al.*, “Pain and health-related quality of life with olaparib versus physician’s choice of next-generation hormonal drug in patients with metastatic castration-resistant prostate cancer with homologous recombination repair gene alterations (PROfound): an open-label, randomised, phase 3 trial,” *Artic. Lancet Oncol*, vol. 23, pp. 393–405, 2022, doi: 10.1016/S1470-2045(22)00017-1.
- [17] M. C. Nigro *et al.*, “Current androgen receptor antagonists under investigation for resistant prostate cancer,” <https://doi.org/10.1080/14737140.2022.2020651>, vol. 22, no. 2, pp. 191–202, 2021, doi: 10.1080/14737140.2022.2020651.
- [18] E. mi Yu and J. B. Aragon-Ching, “Advances with androgen deprivation therapy for prostate cancer,” *Taylor Fr.*, 2022, doi: 10.1080/14656566.2022.2033210.
- [19] X. X. Wei *et al.*, “Outcomes in men with metastatic castration-resistant prostate cancer who received sipuleucel-T and no immediate subsequent therapy: experience at Dana Farber and in the PROCEED Registry,” *Clin. Res.*, doi: 10.1038/s41391-022-00493-x.
- [20] B. W. Labadie *et al.*, “Guidelines for Management of Treatment-Emergent Adverse Events During Rucaparib Treatment of Patients with Metastatic Castration-Resistant Prostate Cancer,” *Cancer Manag. Res.*, p. 14, 2022, doi: 10.2147/CMAR.S335962.
- [21] W. C. Weng, L. H. Huang, N. C. Tseng, and Y. C. Ou, “Radium-223 for metastatic, castration-resistant prostate cancer: A retrospective chart review study of real-world use in a tertiary hospital in Taiwan,” *J. Formos. Med. Assoc.*, Feb. 2022, doi: 10.1016/J.JFMA.2022.01.020.
- [22] L. Wang *et al.*, “Comparison of Treatments for Nonmetastatic Castration-Resistant Prostate Cancer: Matching-Adjusted Indirect Comparison and Network Meta-Analysis,” *JNCI J. Natl. Cancer Inst.*, vol. 114, no. 2, pp. 191–202, Feb. 2022, doi: 10.1093/JNCI/DJAB071.
- [23] D. L. Citrin *et al.*, “A comparison of Zoladex® and DES in the treatment of advanced prostate cancer: Results of a randomized, multicenter trial,” *Prostate*, vol. 18, no. 2, pp. 139–146, Jan. 1991, doi: 10.1002/PROS.2990180206.
- [24] M. Reza *et al.*, “Bone Scan Index as an Imaging Biomarker in Metastatic Castration-resistant Prostate Cancer: A Multicentre Study Based on Patients Treated with Abiraterone Acetate (Zytiga) in Clinical Practice,” *Eur. Urol. Focus*, vol. 2, no. 5, pp. 540–546, 2016, doi: 10.1016/j.euf.2016.02.013.
- [25] G. Wang, D. Zhang, S. Yang, Y. Wang, Z. Tang, and X. Fu, “Co-administration of genistein with doxorubicin-loaded polypeptide nanoparticles weakens the metastasis of malignant prostate cancer by amplifying oxidative damage,” *Biomater. Sci.*, vol. 6, no.

- 827, p. 9, 2018, doi: 10.1039/c7bm01201b.
- [26] H. Liang *et al.*, “Synergistic Silencing of Skp2 by siRNA Self-Assembled Nanoparticles as a Therapeutic Strategy for Advanced Prostate Cancer,” *Small*, 2022, doi: 10.1002/SMLL.202106046.
- [27] M. X. Ren *et al.*, “Magnetite nanoparticles anchored on graphene oxide loaded with doxorubicin hydrochloride for magnetic hyperthermia therapy,” *Ceram. Int.*, vol. 47, no. 14, pp. 20686–20692, 2021, doi: 10.1016/j.ceramint.2021.04.080.
- [28] N. Lavoine, V. Guillard, I. Desloges, N. Gontard, and J. Bras, “Active bio-based food-packaging: Diffusion and release of active substances through and from cellulose nanofiber coating toward food-packaging design,” *Carbohydr. Polym.*, vol. 149, pp. 40–50, 2016, doi: 10.1016/j.carbpol.2016.04.048.
- [29] A. C. Seydim and G. Sarikus, “Antimicrobial activity of whey protein based edible films incorporated with oregano, rosemary and garlic essential oils,” doi: 10.1016/j.foodres.2006.01.013.
- [30] C. J. Ani, Y. Danyuo, O. S. Odusanya, and W. O. Soboyejo, “Computational modeling of drug diffusion and inductive heating in an implantable biomedical device for localized thermo-chemotherapy of cancer cells/tissue,” *Taylor Fr.*, vol. 5, p. 19, 2018, doi: 10.1080/23311916.2018.1463814.
- [31] Y. Danyuo *et al.*, “Swelling of poly(N-isopropylacrylamide) P(NIPA)-based hydrogels with bacterial-synthesized prodigiosin for localized cancer drug delivery,” *Mater. Sci. Eng. C*, vol. 59, pp. 19–29, 2016, doi: 10.1016/j.msec.2015.09.090.
- [32] F. V. Leimann, O. H. Gonçalves, R. A. F. Machado, and A. Bolzan, “Antimicrobial activity of microencapsulated lemongrass essential oil and the effect of experimental parameters on microcapsules size and morphology,” *Mater. Sci. Eng. C*, vol. 29, no. 2, pp. 430–436, Mar. 2009, doi: 10.1016/J.MSEC.2008.08.025.
- [33] R. W. Korsmeyer, R. Gurny, E. Doelker, P. Buri, and N. A. Peppas, “Mechanisms of solute release from porous hydrophilic polymers,” *Int. J. Pharm.*, vol. 15, no. 1, pp. 25–35, 1983, doi: 10.1016/0378-5173(83)90064-9.
- [34] S. Dash, P. N. Murthy, L. Nath, and P. Chowdhury, “Kinetic modeling on drug release from controlled drug delivery systems,” *Acta Pol. Pharm. - Drug Res.*, vol. 67, no. 3, pp. 217–223, 2010.

## CHAPTER TWO

### 2.0. Background and introduction to food preservation

#### 2.1. Introduction

Food preservation procedures include those that limit the growth of microorganisms like yeasts [1](although other methods work by adding harmless bacteria or fungus to the food) and reduce the oxidation of lipids that produce rancidity [2]. Processes that prevent visible deterioration, such as the enzymatic browning reaction in apples after they are chopped during meal preparation, are examples of food preservation [3]. Food waste can be decreased by preserving food, which is an important approach to lower production costs and improve food system efficiency, improve food security and nutrition, and contribute to environmental sustainability [4][5]. Many food preservation systems combine many food preservation methods. Boiling (to lower the fruit's moisture content and kill bacteria, for example), sugaring (to inhibit re-growth), and sealing in an airtight container are all steps in the process of preserving fruit by converting it into jam (to prevent recontamination) [6][7]. The quality of food and food systems is affected differently by various food preservation technologies. When compared to modern techniques of food preservation, several old methods have been demonstrated to use less energy and produce a smaller carbon impact [8][9]. Carcinogens have been discovered in some food preservation procedures. Processed meat, defined as meat that has been salted, cured, fermented, and smoked, was classed as "carcinogenic to humans" by the World Health Organization's International Agency for Research on Cancer in 2015 [10]. Some traditional technics of food preservation includes the following:

**2.1.1 Boiling:** Any existing microorganisms can be killed by boiling liquids. To destroy any hazardous bacteria that may be present in milk and water, they are frequently heated [11].

**2.1.2 Canning:** As a kind of sterilization, canning entails preparing food, sealing it in sterilized cans or jars, then boiling the containers to kill or weaken any remaining microorganisms [12].

**2.1.3 Burial:** Due to a multitude of variables, such as a lack of light, oxygen, cool temperatures, pH level, or desiccants in the soil, food can be preserved by being buried. Other procedures, such as salting or fermentation, can be used in conjunction with burial [13].

**2.1.4 Confit:** Involves preserving meat by salting it, frying it in a fat (such as lard or tallow) at or near 100°C, and then keeping it in the fat [14].

**2.1.5 Cooling:** Slows the growth and reproduction of microbes, as well as the action of enzymes that cause the food to decay [15].

**2.1.6 Curing:** Dehydration or drying, which was utilized as early as 12,000 BC, was the first type of curing followed by smoking and salting procedures which improves the drying process by adding antimicrobial agents [16]. Other traditional technics of food preservation includes the following; Fermentation [17], freezing [18], gelling [19], heating [20], lye [21] and pickling [21].

Modern industrial techniques of food preservation include the following:

**2.1.7 Hurdle technology:** is defined as an intelligent combination of barriers that ensures food product microbiological safety and stability, as well as organoleptic and nutritional quality and economic viability. Some of the hurdles used for food preservation includes the following; high temperature, low temperatures, reduced water activity, increased acidity, reduced redox potential, bio preservatives and other preservatives like sorbates [22],

**2.1.8 Non-thermal plasma:** here the surface of the food is exposed to a "flame" of ionized gas molecules, such as helium or nitrogen, in this process. Microorganisms on the surface die as a result of the flame [23].

**2.1.9 High-pressure food preservation:** here food is being processed to ensure that it preserves its fresh appearance, flavour, texture, and nutrients while inhibiting unwanted microbes and reducing deterioration by pressing it inside a vessel with a pressure of 70,000 pounds per square inch (480 MPa) or more. By 2005, the method had been widely used for a variety of items, including orange juice, guacamole, and deli meats [24].

**2.1.10 Pulsed electric field electroporation (PEF):** is a form of low-temperature pasteurization procedure used to sterilize food. A substance is placed between two electrodes in PEF processing, and then a pulsed electric field is applied. The electric field causes the holes in cell membranes to expand, causing the cells to die and their contents to leak out [25]. Other methods of modern food preservation include; pasteurization [26], vacuum packing [27], freeze drying [28], artificial food additives [29], irradiation and modified atmosphere [30]

## **2.2 Wasted food**

At several phases of the food production, consumption, and supply chain, food is lost or wasted [31]. According to the Food and Agricultural Organisation, “ Food loss is the decrease in the quantity or quality of food resulting from decisions and actions by food suppliers in the chain, excluding retailers, food service providers and consumers”(FAO 2019) [31], [32]. Whereas, “Food waste refers to the decrease in the quantity or quality of food resulting from decisions and actions by retailers, food service providers and consumers” (FAO 2019). According to the FAO's Food Loss Index (FLI), 13.8 percent of food produced in 2016 was lost from the farm to the retail stage [31]. In the US, Losses on farms are likely to be between 15 and 35 percent, depending on the sector. The retail industry has a loss rate

of over 26%, but supermarkets, unexpectedly, only lose approximately 1% with annual losses estimated to be between US\$90 billion and US\$100 billion [33], [34]. Food waste in Africa is a result of inefficient processing and drying, inadequate storage, and a lack of infrastructure. Post-harvest food losses in Sub-Saharan Africa are estimated to be worth \$4 billion annually, enough to feed at least 48 million people [34].

### **2.3 Food preservatives**

Food preservatives can be referred to any of a number of chemical additions used in foods to prevent or delay spoiling caused by chemical changes such as oxidation or mold development [35]. Preservatives come in a variety of forms, each of which is suited to certain products and effective against specific chemical changes [36]. Drying, salting, use of sugar and fermentation are some of the oldest ways of preservation. Food preservation has a number of advantages, including the ability to avoid deterioration and spoilage caused by mold, yeast, botulism, and other foodborne illnesses. Food preservation also saves money by extending the shelf life of the food product [37]. Physical and chemical methods of food preservation are the two methods available [38]. Physical preservation techniques include drying, refrigeration, and freezing [38]. Chemical preservation on the other hand involves adding substances to food to avoid oxidation, rancidity, bacterial development, and other problems [38], [39]. Some of the chemical agents are substances that can kill bacteria or inhibit mold development like benzoates, sorbates (including potassium sorbate, calcium sorbate and sodium sorbate), propionates, nitrites, antioxidants and inhibit oxidation, sulphites, (sodium sulphite, sodium bisulfite, sodium metabisulfite, potassium bisulfite and potassium metabisulfite, vitamin E (tocopherol), vitamin C (ascorbic acid), butylated hydroxyanisole (BHA), butylated hydroxytoluene (BHT), disodium ethylenediaminetetraacetic acid (EDTA) Polyphosphates and citric acid [40]–[42]

## 2.4 Mechanisms of mass transport

The regulation of molecule release typically involves two primary mass transport systems. Internal mass transport, also known as diffusion, is the earliest and most evident one. The external mass transfer from the substance to the external medium is the second one (atmosphere, food simulant, or real food). When the solution is vigorously churned around the device, diffusional mass transport is virtually always involved in the regulation of active species release and is frequently regarded as the primary step (external mass transfer resistance becomes thus negligible). This behavior is often modeled by Fick's law first and second law (equation 1.1 and 1.2), and the apparent coefficient of diffusion, also known as diffusivity, indicates how well the migrant may permeate the material. Unusually important for simulating the discharge from two media in contact is another mass transport parameter. The migrant's distribution between the two mediums at equilibrium is represented by the partition coefficient  $K$ . It is a sign of migrating affinities for the assumed medium. Along with the mass transit of active species, the diffusion of the simulant in contact with the material may also get in the way, causing the polymer to expand and/or become plastic. As a result, it could prevent the release [43]. When modelling the release of active species from food-packaging materials like protein films, mathematical models that were originally created to predict the performance of controlled release systems for pharmaceutical applications have been employed [44]. Cellulose acetate membranes [45] or biocomposite films and microcapsules [46]

$$J = -D \frac{\partial C}{\partial x} \quad 1.1$$

$$\frac{\partial C}{\partial t} = D \frac{\partial^2 C}{\partial x^2} \quad 1.2$$

Where equation 1.1 represents Fick's first law (one dimensional diffusion),  $J$ , the flux (moles/area/time),  $D$  is the diffusion coefficient/diffusivity,  $C$  represents the concentration. Equation two on the other hand represents Fick's second law when concentration changes

with time. The Peppas equation or power law Equation 1.3 is one of the empirical models that is highly popular and simple to use to describe the release of drugs and active substances [47].

$$\frac{m_t}{m_\infty} = kt^n \quad 1.3$$

$m_t$  and  $m_\infty$  are the absolute cumulative amounts of drugs or active species released at time  $t$  and infinite time, respectively;  $k$  is a constant combining the system's structural and geometric properties; and  $n$  is the release exponent, indicating the method of release.

The system's shape and the numerical value of  $n$  give information about the resulting release mechanism. Equation (1.3) has two unique physical realistic implications for  $n = 0.5$  and  $n = 1$  for slab geometry alone. The system describes a controlled molecular release method for  $n = 1$ . When  $n = 0.5$ , the equation alludes to a Fickian diffusion and a diffusion-controlled drug release mechanism [48]. The release of active species intended for use in food packaging is most typically modelled using these models since diffusional mass movement is generally thought of as the key component of the release mechanism. Other models include the Higuchi, first-, second-, and zero-order models. Fick's second law-based models may be solved with the help of the provided initial and boundary conditions, as well as the precise geometry of the device under study [43].

## **2.5 Scope of the projects**

### **2.5.1 Food preservation**

Here, the effects of the regulated release of fungicidal antimicrobials on the preservation of packaged goods (peanuts and bread) are examined in this work. In order to control the release of AM agents into packaged meals, they are encapsulated in films that are 2 mm thick. There are five sections in the article. After the introduction (section 1), Section 2 presents the materials and procedures. The theoretical foundation for the modelling of antimicrobial

release is then described in Section 3, which follows. Findings of the current study are addressed in Section 4, and the conclusions drawn from the current work in Section 5.

## 2.6 Bibliography

- [1] C. Andreu, · Robert Zarnowski, · Marcel·lí, and D. Olmo, “Recent developments in the biology and biotechnological applications of halotolerant yeasts,” *World J. Microbiol. Biotechnol.*, vol. 38, pp. 27–28, 2022, doi: 10.1007/s11274-021-03213-0.
- [2] F. Li, X. Wu, and W. Wu, “Rancidity-induced rice bran protein oxidation causes kidney injury in mice via oxidative stress and inflammatory response,” *J. Cereal Sci.*, vol. 104, p. 103424, Mar. 2022, doi: 10.1016/J.JCS.2022.103424.
- [3] Q. He, Y. Luo, and P. Chen, “Elucidation of the mechanism of enzymatic browning inhibition by sodium chlorite,” *Food Chem.*, vol. 110, no. 4, pp. 847–851, Oct. 2008, doi: 10.1016/J.FOODCHEM.2008.02.070.
- [4] B. Lipinski, C. Hanson, J. Lomax, L. Kitinoja, R. Waite, and T. Searchinger, “Reducing food loss and waste,” *Science (80-. )*, vol. 352, no. 6284, pp. 424–426, 2016, doi: 10.1126/science.352.6284.424-p.
- [5] FAO, “MOVING FORWARD ON FOOD LOSS AND WASTE REDUCTION FOOD AND AGRICULTURE FOOD AND,” *FAO*, p. 24, 2019.
- [6] A. M. Khaneghah, S. Mohammad, B. Hashemi, and S. Limbo, “Antimicrobial agents and packaging systems in antimicrobial active food packaging: an overview of approaches and interactions,” *Food Bioprod. Process.*, vol. 111, pp. 1–19, 2018, doi: 10.1016/j.fbp.2018.05.001.
- [7] D. Kamalakar, L. N. Rao, K. Siva, P. Rao, and M. Venkateswara Rao, “E-ISSN: 2249-1929 Journal of Chemical, Biological and Physical Sciences An International Peer Review E-3 Journal of Sciences Available online atwww.jcbpsc.org Section B: Biological Science CODEN (USA): JCBPAT Research article,” *J. Chem. Bio. Phy. Sci.; Sec. B*, vol. 3, no. 3, 2013.
- [8] “Good food for a better future | Sustainable Development Goals Fund.” [Online]. Available: <https://www.sdgifund.org/good-food-better-future>. [Accessed: 23-Feb-2022].
- [9] J. Salatin, “Joel Salatin Fields of Farmers: Interning , Mentoring , Partnering , Germinating,” 2013.

- [10] A. Jeyakumar, L. Dissabandara, and V. Gopalan, "A critical overview on the biological and molecular features of red and processed meat in colorectal carcinogenesis," *Journal of Gastroenterology*, vol. 52, no. 4. pp. 407–418, 2017, doi: 10.1007/s00535-016-1294-x.
- [11] M. Gallo, L. Ferrara, A. Calogero, D. Montesano, and D. Naviglio, "Relationships between food and diseases: What to know to ensure food safety," *Food Res. Int.*, vol. 137, Nov. 2020, doi: 10.1016/J.FOODRES.2020.109414.
- [12] M. Yadav, Y. Ahmadi, and F.-C. Chiu, "Food and bioprocessing industry," *Handb. Polym. Nanocomposites Ind. Appl.*, pp. 295–324, 2021, doi: 10.1016/B978-0-12-821497-8.00009-5.
- [13] W. Fox-Turnbull and E. Reinsfield, "Technology across boundaries: preserve or perish," *International Journal of Technology and Design Education*. 2021, doi: 10.1007/s10798-021-09700-7.
- [14] W.-S. Chen, "Duck Slaughter Processing and Meat Quality Measurements," *Duck Prod. Manag. Strateg.*, pp. 403–442, 2022, doi: 10.1007/978-981-16-6100-6\_11.
- [15] "Review Article on; Traditional and Modern Techniques For Food Preservation | International Journal of Modern Agriculture." [Online]. Available: <http://modern-journals.com/index.php/ijma/article/view/1535>. [Accessed: 23-Feb-2022].
- [16] B. Lebret and M. Čandek-Potokar, "Review: Pork quality attributes from farm to fork. Part II. Processed pork products," *Animal*, p. 100383, Nov. 2021, doi: 10.1016/J.ANIMAL.2021.100383.
- [17] M. Mannaa, G. Han, Y. S. Seo, and I. Park, "Evolution of food fermentation processes and the use of multi-omics in deciphering the roles of the microbiota," *Foods*, vol. 10, no. 11. 2021, doi: 10.3390/foods10112861.
- [18] S. Nida, J. A. Moses, and C. Anandharamakrishnan, "Isochoric Freezing and Its Emerging Applications in Food Preservation," *Food Engineering Reviews*, vol. 13, no. 4. pp. 812–821, 2021, doi: 10.1007/s12393-021-09284-x.
- [19] L. Wang, V. Fogliano, J. Heising, and M. Dekker, "The effect of pore size on the diffusion of volatile antimicrobials is a key factor to preserve gelled foods," *Food Chem.*, vol. 351, p. 129316, Jul. 2021, doi: 10.1016/J.FOODCHEM.2021.129316.
- [20] V. A. Vaclavik, E. W. Christian, and T. Campbell, "Food Preservation," *Springer Nat.*, pp. 327–346, 2021, doi: 10.1007/978-3-030-46814-9\_16.
- [21] H. A. Abdulmumeen, A. N. Risikat, and A. R. Sururah, "Food: Its preservatives, additives and applications," *Ijcbs*, vol. 1, pp. 36–47, 2012.
- [22] "Handbook of Seafood Quality, Safety and Health Applications - Google Books." [Online]. Available: [https://books.google.com/books?id=l-APOWUVp-8C&pg=PT232&dq=%22hurdle+technology%22%7C%22hurdle+technologies%22&hl=en&ei=5GSFTaTGCJCSuAOj66zGCA&sa=X&oi=book\\_result&ct=result&resnum=3&ved=0CDgQ6AEwAg#v=onepage&q=%22hurdle+technology%22%7C%22hurdle+technologies%22&f=false](https://books.google.com/books?id=l-APOWUVp-8C&pg=PT232&dq=%22hurdle+technology%22%7C%22hurdle+technologies%22&hl=en&ei=5GSFTaTGCJCSuAOj66zGCA&sa=X&oi=book_result&ct=result&resnum=3&ved=0CDgQ6AEwAg#v=onepage&q=%22hurdle+technology%22%7C%22hurdle+technologies%22&f=false). [Accessed: 24-Feb-2022].
- [23] M. Saiful and I. Khan, "Applicability of non-thermal plasma as an emerging technology on pathogen inactivation in food industry Nonthermal Plasma Sterilization View project," University of Science and Technology, 2017.

- [24] P. K. Gruchelski Marek , Gruchelski Marcin, “The use of pascalization in the Polish food industry – characteristics and prospects® - Postępy Techniki Przetwórstwa Spożywczego - Tom nr 2 (2020) - BazTech - Yadda,” *High. Sch. Manag.*, vol. 2, 2020.
- [25] J. Blahovec, E. Vorobiev, and N. Lebovka, “Pulsed Electric Fields Pretreatments for the Cooking of Foods,” *Food Eng. Rev.*, vol. 9, no. 3, pp. 226–236, 2017, doi: 10.1007/s12393-017-9170-x.
- [26] G. Saldaña, I. Álvarez, S. Condón, J. Raso, and I. Alvarez, “Microbiological Aspects Related to the Feasibility of PEF Technology for Food Pasteurization Microbiological Aspects Related to the Feasibility of PEF Technology for Food Pasteurization,” *Food Sci. Nutr.*, vol. 8398, p. 13, 2014, doi: 10.1080/10408398.2011.638995.
- [27] S. I. Ekonomou, F. F. Parlapani, M. Kyritsi, C. Hadjichristodoulou, and I. S. Boziaris, “Preservation status and microbial communities of vacuum-packed hot smoked rainbow trout fillets,” *Food Microbiol.*, vol. 103, no. July 2021, pp. 1–11, 2022, doi: <https://doi.org/10.1016/j.fm.2021.103959>.
- [28] R. B. Waghmare *et al.*, “Trends in Approaches to Assist Freeze-Drying of Food : A Cohort Study on Innovations Trends in Approaches to Assist Freeze-Drying of Food : A Cohort Study on Innovations,” *Food Rev. Int.*, p. 23, 2021, doi: 10.1080/87559129.2021.1875232.
- [29] L. Wu, Q. C. Chenghui Zhang, yingxi long, and weimin Z. and G. Liu, “Food additives\_ From functions to analytical methods,” *Food Sci. Nutr.*, p. 22, 2021, doi: <https://doi.org/10.1080/10408398.2021.1929823>.
- [30] E. Chouliara, A. Badeka, I. Savvaidis, and M. G. Kontominas, “Combined effect of irradiation and modified atmosphere packaging on shelf-life extension of chicken breast meat: Microbiological, chemical and sensory changes,” *Eur. Food Res. Technol.*, vol. 226, no. 4, pp. 877–888, 2008, doi: 10.1007/s00217-007-0610-3.
- [31] D. Patra, P. T. Leisnham, C. K. Tanui, and A. K. Pradhan, “Evaluation of global research trends in the area of food waste due to date labeling using a scientometrics approach,” *Food Control*, vol. 115, Sep. 2020, doi: 10.1016/J.FOODCONT.2020.107307.
- [32] “Africa – Regional Overview of Food Security and Nutrition 2021,” *Africa – Reg. Overv. Food Secur. Nutr. 2021*, Dec. 2021, doi: 10.4060/CB7496EN.
- [33] “Digital Library Of The Commons.” [Online]. Available: <http://dlc.dlib.indiana.edu/dlc/handle/10535/5088>. [Accessed: 28-Feb-2022].
- [34] “Worldwide food waste | ThinkEatSave.” [Online]. Available: <https://www.unep.org/thinkeatsave/get-informed/worldwide-food-waste>. [Accessed: 28-Feb-2022].
- [35] C. Novais *et al.*, “Natural Food Colorants and Preservatives: A Review, a Demand, and a Challenge,” doi: 10.1021/acs.jafc.1c07533.
- [36] Y. Lu *et al.*, “Application of Gelatin in Food Packaging: A Review,” *Polymers (Basel)*, vol. 14, no. 3, p. 19, Jan. 2022, doi: 10.3390/POLYM14030436.
- [37] D. Patra, S. C. Henley, E. O. Benefo, A. K. Pradhan, and A. Shirmohammadi, “Understanding and addressing food waste from confusion in date labeling using a stakeholders’ survey,” *J. Agric. Food Res.*, vol. 8, p. 7, Jun. 2022, doi:

- 10.1016/J.JAFR.2022.100295.
- [38] E. Luck, “[Chemical preservation of food].,” *Zentralbl. Bakteriol. Mikrobiol. Hyg. B.*, vol. 180, no. 2–3, pp. 311–318, Feb. 1985.
- [39] Q. Xie *et al.*, “Active edible films with plant extracts: a updated review of their types, preparations, reinforcing properties, and applications in muscle foods packaging and preservation,” *Taylor Fr.*, p. 24, 2022, doi: 10.1080/10408398.2022.2092058.
- [40] G. Rizzello, P. De Bellis, A. Nasrollahzadeh, S. Mokhtari, M. Khomeiri, and P. E. J. Saris, “Antifungal Preservation of Food by Lactic Acid Bacteria,” 2022, doi: 10.3390/foods11030395.
- [41] S. Dey and B. H. Nagababu, “Applications of food color and bio-preservatives in the food and its effect on the human health,” *Food Chem. Adv.*, vol. 1, p. 13, Oct. 2022, doi: 10.1016/J.FOCHA.2022.100019.
- [42] S. Singh, P. K. Chaurasia, and S. L. Bharati, “Functional roles of Essential oils as an effective alternative of synthetic food preservatives: A review,” *J. Food Process. Preserv.*, p. 15, Jun. 2022, doi: 10.1111/JFPP.16804.
- [43] N. Lavoine, V. Guillard, I. Desloges, N. Gontard, and J. Bras, “Active bio-based food-packaging: Diffusion and release of active substances through and from cellulose nanofiber coating toward food-packaging design,” *Carbohydr. Polym.*, vol. 149, pp. 40–50, 2016, doi: 10.1016/j.carbpol.2016.04.048.
- [44] A. C. Seydim and G. Sarikus, “Antimicrobial activity of whey protein based edible films incorporated with oregano, rosemary and garlic essential oils,” doi: 10.1016/j.foodres.2006.01.013.
- [45] S. Gemili, A. Yemenicioğlu, and S. A. Altinkaya, “Development of antioxidant food packaging materials with controlled release properties,” *J. Food Eng.*, vol. 96, no. 3, pp. 325–332, 2010, doi: 10.1016/j.jfoodeng.2009.08.020.
- [46] F. V. Leimann, O. H. Gonçalves, R. A. F. Machado, and A. Bolzan, “Antimicrobial activity of microencapsulated lemongrass essential oil and the effect of experimental parameters on microcapsules size and morphology,” *Mater. Sci. Eng. C*, vol. 29, no. 2, pp. 430–436, Mar. 2009, doi: 10.1016/J.MSEC.2008.08.025.
- [47] R. W. Korsmeyer, R. Gurny, E. Doelker, P. Buri, and N. A. Peppas, “Mechanisms of solute release from porous hydrophilic polymers,” *Int. J. Pharm.*, vol. 15, no. 1, pp. 25–35, 1983, doi: 10.1016/0378-5173(83)90064-9.
- [48] J. Siepmann and F. Siepmann, “Mathematical modeling of drug delivery,” *Int. J. Pharm.*, vol. 364, no. 2, pp. 328–343, Dec. 2008, doi: 10.1016/J.IJPHARM.2008.09.004.

## CHAPTER THREE

### 3.0 Literature review

#### 3.1 Targeted drug release

The term "drug delivery system" (DDS) refers to a method of distributing a pharmaceutical compound, formulation, or delivery system that is utilized to distribute a drug to humans or animals in order to have a therapeutic effect [1]–[3].

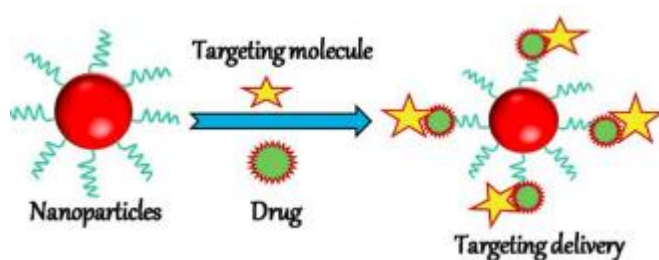


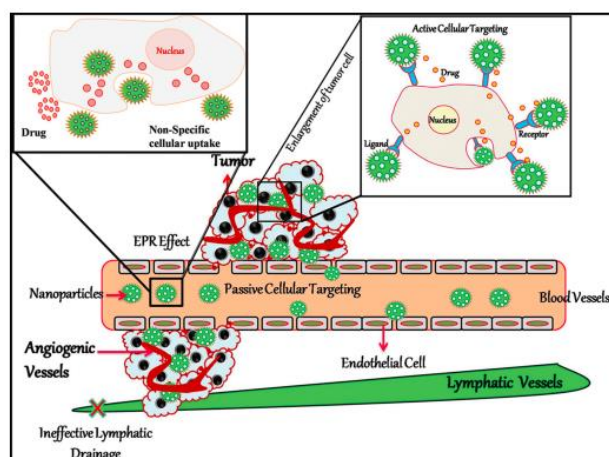
Figure 3.1: Scheme of nanoparticles based targeted drug delivery [1]

By regulating the timing, pace, and location of drug release in the body, it increases the therapeutic substance's effectiveness and safety. It mostly includes site targeting within the body [4]. The procedure of targeted drug delivery (TDD) primarily combines the drug dose type and mode of administration. It entails putting the therapeutic substance or formulation

into the body, allowing it to release its active elements, then moving those compounds to the site of action by passing them across biological membranes [3]. TDD is superior to traditional drug dose forms in several ways, including higher effectiveness, better drug bioavailability, less toxicity, and improved patient comfort. TDD is a recognized and legitimate treatments approach that creates platforms and nanoscale devices for the targeted delivery of tiny medicinal molecules and therapeutic genes to target cells. Figure 3.1 shows a scheme of targeted medication administration using nanoparticles. Molecular approaches to developing such delivery systems differ a great deal. When delivering treatments to the desired cells, the use of nanometer-sized entities or other types of nanocarriers is crucial [5], [6]. Three mechanistic components combine to form the basis of the nano drug delivery idea; each one is crucial to effective delivery. First, specific cellular binding via a receptor-ligand interaction, secondly, the targeted cells' intracellular absorption of drug-carrying nanomaterials through receptor-mediated endocytosis and lastly regulated intracellular release of drug molecules that were transported in their active state. In order for the drug to only display its biological activity in the targeted cell, the third phase, which involves drug release, must be carried out in a carefully regulated way [1]. Due to the improved permeability and retention effect, these drug carriers are suitable because tumors are passively targeted by them ideally suitable for chemotherapeutic drug delivery in cancer therapy

### 3.1.1. Active passive targeting

The "enhanced permeability and retention effect" (EPR) effect, a distinctive property of tumor cells, is used to deliver anticancer drugs to specific areas of the body [1]. The nanoparticle surface



may be altered with a range of ligands that would bind with certain receptors overexpressed on the surface of the tumor cells, providing selectivity for active targeting in addition to this passive targeting based primarily on size. Another cutting-edge technique for targeted administration is the site-specific release of a drug that is present in a nanoparticulate system when external stimuli, such as hyperthermia, are applied to a thermosensitive device [7], [8].

Figure 3.2: Schematic of passive tissue targeting and active cellular delivery of anticancer medicines to tumors utilizing nanocarriers. Reproduced from [68], D. Peer et al., *Nat. Nanotechnol.* 2, 751, with permission (2007). Nature Publishing Group, 2007. [1]

Two methods are often used to deliver therapeutic drugs using nanocarriers, as shown in Figure 3.2. The first is, non-targeted delivery (passive targeting) and targeted delivery (active targeting)

Passive targeting makes use of the greater interstitial gaps greater than (200 –1200 nm) between nearby endothelial cells in tumors, which enhances the permeability of the endothelial blood microvasculature compared to normal tissue. On the other hand, active targeting tries to target specific cancer cells while also utilizing the EPR effect.

### **3.1.2. Nanotechnology**

Nanotechnology is a new and effective therapeutic approach that employs nanoparticles (NPs) for disease detection to nanoparticle drug delivery systems that can circumvent life-

threatening illnesses like cancer and associated treatments [9], [10]. 2 NPs have the potential to provide solutions to the current difficulties in conventional cancer therapy due to their unique size, which is generally falls into a size range (1–100 nm) which is similar to basic biological materials such as DNA, proteins and other macromolecular structures found inside living cells. Nanocarriers are a promising means of delivering anti-cancer medications to tumors, as shown in Figure 3.3's schematic of passive tissue targeting and active cellular use.

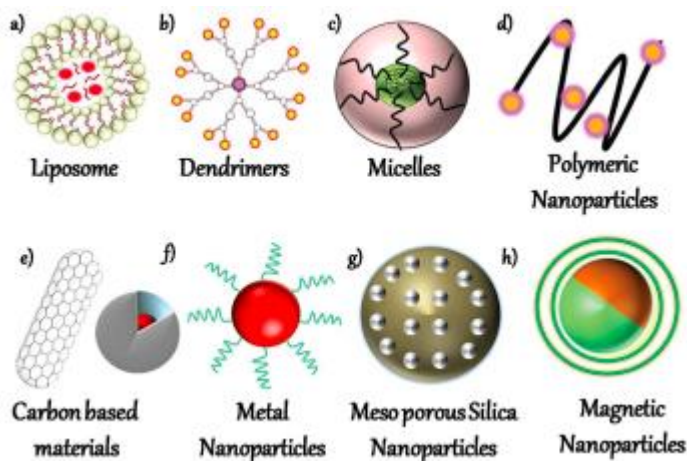


Figure 3.3: Nanocarriers that are often used in drug delivery applications.

### 3.1.3. Biomarkers for prostate cancer

Prostate cancer detection and treatment has undergone a radical change thanks to the emergence of biomarkers for the disease prognosis, diagnosis, treatment and screening. PSA is a helpful, but non-specific, biomarker for identifying prostate cancer. Prostate cancer biomarkers could be classified based on their location. Serum biomarkers are the biomarkers that are found in the blood such as: prostatic acid phosphatase (PAP) [11], [12], total prostate specific antigen (tPSA), free prostate specific antigen (fPSA) [13], prostate specific antigen

(PSA), prostate specific antigen density (PSAD) [14], prostate specific antigen velocity (PSAV) [15], prostate specific antigen doubling time (PSADT) [16], EPCA, and EPCA-2 in the blood [17], AMACR in the tissues [18], [19], methylation GSTP1 [20], [21], and the TMPRSS2-ETS gene rearrangement in the urine [22], and DD3PCA3/UPM-3 in the serum [23].

#### **3.1.4 Prostate cancer targeted drug delivery**

Several work has been carried out to validate the expression of AMACR on PC to enhance targeted/localized delivery of drug to targeted site. Candidate biomarkers and regulatory genes have been found as a result of molecular profiling of prostate cancer. The examination of prostate diagnostic specimens may be able to benefit from the discoveries made by these genome-scale techniques. To ascertain the expression and clinical relevance of alpha-methylacyl coenzyme A racemase (AMACR), a gene discovered by global profiling techniques as being overexpressed in prostate cancer [19]. To carry out this analysis (n = 128 specimens), four gene expression data sets from separate deoxyribonucleic acid (DNA) microarray investigations were analysed. Reverse transcriptase polymerase chain reaction (RT-PCR) was used to confirm the transcript level of the lead candidate gene AMACR, and immunoblot and immunohistochemistry analyses were used to confirm the protein level. In 342 samples spanning various phases of prostate cancer growth, AMACR levels were assessed utilizing prostate cancer tissue microarrays. Protein expression was scored negatively (score = 1), weakly (score = 2), moderately (score = 3), or strongly (score = 4). Using 94 prostate needle biopsy samples, the clinical usefulness of AMACR was assessed. Using several experimental techniques and prostate cancer tissues, it was demonstrated that AMACR is overexpressed in prostate cancer. When interpreting prostate needle biopsy samples that provide a diagnostic challenge, AMACR may be helpful [19].

In another research to inhibit the growth of Prostate cancer cell fluorescence imaging was used coupled with gelatin-doxorubicin conjugate (GLT-DOX) and epigallocatechin gallate (EGCG)-coated with gold nanoparticles (DOX-GLT/EGCG AuNPs) [24]. In another research targeting prostate cancer cells with mesoporous silica nanoparticles containing doxorubicin that have been functionalized with decapeptide yielded an improved apoptotic activity in breast and prostate cancer cells [25].

### **3.2 Food preservation**

Acquiring the expertise to preserve foods was one of the key revolutionary breakthroughs of human civilization since it was a requirement for man to settle down in one area and create a community. However, it remains crucial and difficult to extend food items' shelf life without sacrificing their original nutritional qualities. Food is a perishable organic product that can degrade as a result of microbiological, chemical, or physical processes [26]. In the past, a variety of traditional methods, including drying, chilling, freezing, and fermenting, have been developed to preserve food while preserving its nutritional content and texture [26]. Preservation methods have evolved and become more modernized throughout time in response to increasing needs. The newest developments in food preservation include pulsed electric field effect, high pressure food preservation, and irradiation [26]. Modern advancements are employed to extend food's shelf life. Additionally, other chemical agents have been developed as food additives and preservatives. However, due to potential health risks, there are rising worries about the use of chemical additives and preservatives in food products [26]. The food processing and preservation industry has been rapidly increasing in order to keep up with consumer demand. Understanding food deterioration mechanisms and food preservation procedures is vital for ensuring food safety and a long shelf life for foods.

### **3.2.1. Food spoilage: mechanism**

The process through which food loses its edibility is called food deterioration. Colour, smell, flavour, texture, or the appearance of the food can all indicate early food spoiling [26]. Food spoilage can result from a variety of physical, microbiological, or chemical events. Since the deterioration brought can trigger another, it therefore, implied that these mechanisms are not mutually exclusive. The main causes of food deterioration include temperature, pH, air, nutrition, and the presence of various compounds [27].

#### **3.2.1.1. Physical spoilage**

Physical food spoilage/deterioration is the degradation of food brought on by physical changes or instability. Physical deterioration includes, but is not limited to, moisture loss or gain, moisture migration between various components, and physical separation of ingredients or components [26], [28], [29]. Moisture content, temperature, glass transition temperature, crystal development, and crystallization are the main elements influencing physical deterioration.

- **Moisture content**

A frequent cause of degradation of food products is the change in their water content. It may occur in the form of water loss, water gain, or migration of water [30]. Water activity ( $a_w$ ) is a thermodynamic property which is expressed as the ratio of the vapor pressure of water in a system to the vapor pressure of pure water at the same temperature [15, 27]. It is also possible to substitute equilibrium relative humidity at the same temperature for pure water vapour pressure. With increasing temperature, water activity in food items decreases. Generally speaking, foods have a water activity of 1 at room temperature, compared to 0.82 and 0.68 at 20 and 40 °C, respectively. Alternatives to pure water vapor pressure include equilibrium relative humidity at the same temperature. As the temperature rises, the water activity in food

products decreases. The water activity of meals is typically 1.0 at room temperature, but it is 0.82 and 0.68 at 20 and 40 °C, respectively.

- **Temperature**

The most important component in the deterioration of fruits and vegetables is temperature. For gradual ripening and to extend post-harvest life, there is a preferred temperature range. Optimal relative humidity and air flow around fruit and vegetables are also necessary for slow ripening. These ideal circumstances appear to be known as modified atmospheres (MA) [31]. Foods that are prone to freeze damage may suffer unfavourable effects as a result of low temperatures. Food goods become damaged when their cells break when partly frozen at lower temperatures. The majority of tropical fruits and vegetables are vulnerable to damage from chilling. When the temperature is between 5 and 15 degrees Celsius, this often happens before the food product begins to freeze [29].

- **Glass transition temperature**

The shelf life of food items is influenced by the glass transition temperature (T<sub>g</sub>). Both crystalline and amorphous metastable solids can be found in food products. This behaviour is dependent on the temperature, relative humidity, and solids composition [32]. The shift from a glassy to a rubbery state takes place at the glass transition temperature. This process of second-order phase change occurs at a temperature that varies depending on the food. The glass transition temperature and food physical stability are connected. The concentration of water and other plasticizers has a significant impact on the glass transition temperature (T<sub>g</sub>) [33]. Due to the glass transition phenomenon, dry food items that are stored in extremely humid environments change in state [29].

- **Crystal growth and crystallization**

Food deterioration can also be a result of freezing. Foods that are slowly frozen or frozen several times suffer greatly as a result of crystal development. They have significant extracellular ice accumulation. These foods are more stable than processed foods with gradual freezing because rapid freezing creates ice inside food cells [34]. Emulsifiers and other water binding agents can be applied during freezing cycles to reduce the formation of big ice crystals [35]. Foods with a high sugar content can crystallize sugar when the temperature rises or moisture builds up. As a result, sugar rises to the surface from within and takes on a gray or white colour. The effects of sugar crystallization include the staling of sugar cookies and graininess in candies and ice creams [29]. Fructose or starch can be added to sugar solutions to prevent crystallization. Time is also a key factor in the crystallization of sugar in food products above the appropriate glass transition temperature [24].

### **3.2.1.2 Microbial spoilage**

Whenever food spoilage occurs as a result of the action of microorganisms such as bacteria, mould and yeast etc. it is referred to as microbial spoilage [26], [36]. Additionally, it is the main source of foodborne diseases. Different microbes frequently damage perishable foods, so by adjusting storage temperature, lowering water activity, lowering pH, adding preservatives, and using the right packaging may all slow or stop the growth of most microbes [37]. Microbial food spoilage is affected by some intrinsic properties like endogenous enzymes, substrates, light sensitivity, oxygen, pH, water activity, nutrient content oxidation and reduction potential while the extrinsic properties that affects the microbial food spoilage includes relative humidity, temperature and the activities of other harmful microbes [26], [38].

### **3.2.1.3 Chemical spoilage**

Chemical spoilage occurs whenever there is a chemical or biochemical reactions in food items thereby leading to some unpleasant sensory results in food products [26]. Both

chemical and microbial food spoilage are affected by factors such as: oxidation (Ammonia and organic acids are produced when there is oxygen present in amino acids)[38], proteolysis (Proteolysis is a common and permanent post-translational modification that affects just a few, very specific peptide and iso-peptide links in a protein)[39], putrefaction (Putrefaction is a sequence of anaerobic processes in which amino acids divert to a combination of amines, organic acids, and sulphur compounds with foul-smelling aromas, such mercaptans and hydrogen sulfide) [40], Maillard reaction (This reaction happens in the amino acid or amino group of proteins when dry milk, dry whole eggs, and breakfast cereals are stored and this reaction is known as enzymatic browning) [26], Pectin hydrolysis (During fruit ripening, indigenous pectinases are produced or activated, causing pectin hydrolysis, which weakens the structure of food. And this can cause Mechanical damage on fruits and vegetables and it can also trigger pectinases and start a microbial attack)[41] and Hydrolytic rancidity (by using lipolytic enzymes, hydrolytic rancidity degrades lipids. In this process, free fatty acids are separated from triglyceride molecules while being in the presence of water. These free fatty acids have rotten tastes or odours)[42].

### **3.3 Effectiveness of antimicrobial food packaging**

For a long time, antimicrobial compounds have been utilized as direct food additives with success. Evidence from the literature suggests that some of these additives could work well when used as indirect food additives in food packaging materials. Antimicrobial food packaging aims to reduce surface contamination of processed, prepared foods like sliced meats, peanuts and Frankfurter sausages (hot dogs). It is important to note that antimicrobial additives are not intended to replace basic sanitation methods, but rather to increase food shelf life by providing an extra barrier to the growth of harmful microorganisms. Studies have concentrated on developing procedures for coating barrier films or low-density

polyethylene (LDPE) film with methyl cellulose as a nisin carrier. *Listeria monocytogenes* has been greatly decreased using nisin antimicrobial films in solutions and vacuum-sealed hot dogs. Other studies have concentrated on the use of chitosan to prevent *L. monocytogenes* growth and chlorine dioxide sachets to reduce *Salmonella* on fresh chicken breasts packaged in modified atmospheres. Hence, antimicrobial packaging has a lot of potential as a way to stop certain microorganisms from growing in food, but there are still obstacles in the way of its widespread commercial use [43].

### **3.4 Antimicrobial packaging**

Active packaging has a variety of uses, including antimicrobial packaging [44]. When active substances are added to the packaging system or functional polymers are used, the packaging system achieves qualities above and beyond basic barrier properties [45]. The packaging technology known as antimicrobial packaging has the ability to destroy or suppress the microbes that contaminate food and causes food deterioration. By using antimicrobial agents in the packaging system and/or employing antimicrobial polymers that meet standard packaging criteria, the novel antimicrobial function can be accomplished [46]. Antimicrobial packaging is particularly made to manage microorganisms that often have a negative impact on the shelf-life extension, quality maintenance, and safety assurance. Hence, the primary objectives of an antimicrobial packaging system are (i) safety assurance, (ii) quality maintenance, and (iii) shelf-life extension, in that order. Antimicrobial packaging could contribute to food safety. All antimicrobial agents have unique properties that influence microbes in various ways. There isn't a single antimicrobial substance that can successfully combat all harmful and spoilage microorganism. Due to the distinctive antimicrobial processes and the diverse physiologies of the microorganisms. Selecting particular antimicrobial agent may benefit greatly from simple microbe categorization. These

classifications could include the need for oxygen (for aerobes and anaerobes), the composition of the cell wall (for Gram positive and negative bacteria), the growth stage (for spores and vegetative cells), the ideal growth temperature (for thermophilic, mesophilic, and psychrotropic bacteria), and the resistance to acid and osmosis. Understanding the antimicrobial agent's distinctive antimicrobial function is crucial for determining the activity's effectiveness and bounds. Some antimicrobial substances inhibit vital metabolic (or genetic reproduction) processes in microorganisms, while others change the composition of cell membranes and walls. For instance, lactoferrin and EDTA operate as coupling agents for essential cationic ions charged polymers, whereas lysozyme causes physical damage to cell walls without inhibiting metabolic processes. Microbial-cidal and microbial-static effects are two of the main purposes of microbial inhibition. To prevent the regrowth of the target microorganisms in the case of a microbial-static effect, the packaging system must actively maintain the concentration above the minimal inhibitory concentration during the whole storage period of shelf life. When antimicrobial properties are accomplished by the use of antimicrobial polymeric materials or by incorporating antimicrobial agents into the packaging system, there are typically three different modes of action: release, absorption, and immobilization. Antimicrobial drugs may enter foods or the headspace of packaging with certain types of release, which prevents the development of microorganisms. The antibacterial substances might either be a gas or a solute. But unlike gaseous antimicrobial agents, which may pass through any area, soluble antimicrobial agents cannot migrate through air gaps or across the voids between a packaging and a food product. The antimicrobial system's absorption mode stops the development of germs by removing crucial ingredients from food systems. For instance, the oxygen-absorbing device helps stop mold from growing within containers. Instead of dispersing antimicrobial agents, an immobilization system inhibits bacteria growth on the contact surface. Due to the lower

likelihood of interaction between the antimicrobial package and the complete food items, immobilization systems for solid foods may be less effective than those for liquid foods [45].

### 3.5 Antimicrobial agents

Antimicrobial agents are many and have been employed in various food preservation purposes. The industry must abide by the rules and regulations of the nation in which it intends to utilize antimicrobial agents, such as the food and drug administration (FDA) and/or EPA in the United States, in order to do so. This indicates that only compounds that are FDA-approved or notified-to-use within the concentration limitations for food safety enhancement or preservation may be used in the development of novel antimicrobial packaging materials. Chemical antimicrobials, antioxidants, biotechnology products, antimicrobial polymers, natural antimicrobials, and gas are only a few examples of the antimicrobial agents that may be used in the packaging system. The most often utilized materials in the sector are chemical antimicrobial agents. They comprise antibiotics, fungicides, organic acids, and alcohols [45]. As shown in the table below.

Table 3.1: Antimicrobial agents and packaging systems [45]

Antimicrobials	Packaging materials	Foods	Microorganisms	References
<b>Organic acids</b>				
Benzoic acids	PE	Tilapia fillets	Total bacteria	Huang <i>et al.</i> , 1997
Benzoic acids	Ionomer	Culture media	<i>Pen. Spp.</i> , <i>Asp. niger</i>	Weng <i>et al.</i> , 1997
Benzoic & sorbic acids	PE-co-met-acrylates	Culture media	<i>Asp. niger</i> , <i>Pen. Spp.</i>	Weng <i>et al.</i> , 1999
<b>Enzymes</b>				
Lysozyme, nisin, EDTA	SPI, zein	Culture media	<i>E. coli. Lb. plantarum</i>	Padgett <i>et al.</i> , 1998
EDTA, propyl	WPI	Culture media	<i>Typhimurium</i> , <i>E. coli</i> , <i>B. thermosph.</i> ,	

paraben			<i>aueus</i>	Rodrigues <i>et al.</i> , 2002
Immobilized lysozyme	PVOH, nylon, cellulose acetate	Culture media	Lysozyme activity test	Appendini & Hotchkiss, 1996; 1997
<b>Bacteriocins</b>				
Nisin	PE	Beef	<i>B. thermosph.</i>	Siragusa <i>et al.</i> , 1999
Nisin, lauric acid	Zein	Simulant	Migration test	Hoffman <i>et al.</i> , 2001
Nisin, citrate, EDTA	PVC, nylon, LLDPE	Chicken	<i>Sal. typhimurium</i>	Tatrajan & Sheldon 2000
<b>Fungicides</b>				
Imazalil	LDPE	Bell pepper	Molds	Miller <i>et al.</i> , 1984
Imazalil	PE	Cheese	Molds	Weng & Hotchkiss, 1992
Benomyl	Ionomer	Culture media	Molds	Halek & Garg, 1989
<b>Polymers</b>				
Chitosan	Chitosan/paper	Strawberry	<i>E. coli</i>	Yi <i>et al.</i> , 1998
Chitosan, herb extract	LDPE	Culture media	<i>Lb. plantarum</i> , <i>E. coli</i> , <i>S. cerevisiae</i> , <i>fusarium oxysporum</i>	Hong <i>et al.</i> , 2000
UV/excimer laser irradiated nylon	Nylon	Culture media	<i>S. aureus</i> , <i>Pseudo. fluorescens</i> , <i>Enterococcus faecalis</i>	Paik <i>et al.</i> , 1998; Paik & Kelly 1995
<b>Natural extract</b>				
Grapefruit seed extract	LDPE, nylon	Ground beef	Aerobes, coli-forms	Ha <i>et al.</i> , 2001
Clove extract	LDPE	Culture media	<i>L. plantaru</i> , <i>E. coli</i> , <i>F. oxysporum</i> , <i>S. cerevisiae</i>	Hong <i>et al.</i> , 1998
Eugenol, cinnam aldehyde	Chitosan	Bologna, ham	Enterobac., lactic acid bacteria, <i>L.b.</i>	Outtara <i>et al.</i> , 2000b

sakei, *Serratia* spp.

### Oxygen adsorber

Ageless	Sachet	Bread	Molds	Smith <i>et al.</i> , 1989
BHT	HDPE	Breakfast cereal	Molds	Hoojjatt <i>et al.</i> , 1987

### Gas

Ethanol	Silica gel sachet	Culture media	Molds	Shapero <i>et al.</i> , 1978
Hinokithiol	Cyclodextrin/plactic (Seiwa) sachet	Bakery	Molds	Gontard, 1997
ClO <sub>2</sub>	Plastic films	Bakery	Migration test	Ozen & Floros 2001

### Others

Hexamethylenetetramine	LDPE	Orange juice	Yeast, lactic acid & bacteria	Devlieghere <i>et al.</i> , 2000b
Silver Zeolite siver nitrate	LDPE	Culture media	<i>S. cerevisiae</i> , <i>E. coli</i> , <i>S. aureus</i> , <i>Sal. typhimurium</i> , <i>Vibrio parahyhaemolyticus</i>	Ishitani, 1995
Antibiotic	PE	Culture media	<i>E. coli</i> , <i>S. aureus</i> , <i>Sal. typhimurium</i> , <i>Klebsiella neumoniae</i>	Han & moon, 2002

PE: polyethylene; LDPE: low density polyethylene; WPI: whey protein isolates; HDPE: high density polyethylene; BHT: Butylated hydroxytoluene; EDTA; Ethylenediamine tetraacetic acid; PCV: polyvinyl chloride; UV: ultra violet; PVOH: poly(vinyl alcohol); LLDPE: linear low density polyethylene

Hence, Antimicrobial packaging system can inhibit the growth of spoilage and pathogenic microorganisms, and contribute to the improvement of food safety and the extension of shelf life of the packaged food. Many factors are involved in designing the antimicrobial packaging system, however, most factors are closely related to the characteristics of antimicrobial agents, packaged foods and target microorganisms [45].

### 3.6 Bibliography

- [1] S. Hema, S. Thambiraj, and D. R. Shankaran, “Nanoformulations for Targeted Drug Delivery to Prostate Cancer: An Overview,” *J. Nanosci. Nanotechnol.*, vol. 18, no. 8, pp. 5171–5191, Feb. 2018, doi: 10.1166/JNN.2018.15420.
- [2] T. M. Allen and P. R. Cullis, “Liposomal drug delivery systems: From concept to clinical applications,” *Adv. Drug Deliv. Rev.*, vol. 65, no. 1, pp. 36–48, 2013, doi: 10.1016/j.addr.2012.09.037.
- [3] K. K. Jain, “Drug delivery systems - An overview,” *Methods Mol. Biol.*, vol. 437, pp. 1–50, 2008, doi: 10.1007/978-1-59745-210-6\_1/COVER.
- [4] G. Tiwari *et al.*, “Drug delivery systems: An updated review,” *Int. J. Pharm. Investig.*, vol. 2, no. 1, p. 11, 2012, doi: 10.4103/2230-973X.96920.
- [5] R. Ravichandran, “Studies on Dissolution Behaviour of Nanoparticulate Curcumin Formulation,” *Adv. Nanoparticles*, vol. 2013, no. 01, pp. 51–59, Feb. 2013, doi: 10.4236/ANP.2013.21010.
- [6] P. T. Wong and S. K. Choi, “Mechanisms of Drug Release in Nanotherapeutic Delivery Systems,” 2015, doi: 10.1021/cr5004634.
- [7] N. Bertrand, J. Wu, X. Xu, N. Kamaly, and O. C. Farokhzad, “Cancer nanotechnology: The impact of passive and active targeting in the era of modern cancer biology,” *Adv.*

- Drug Deliv. Rev.*, vol. 66, pp. 2–25, 2014, doi: 10.1016/J.ADDR.2013.11.009.
- [8] V. Torchilin, “Tumor delivery of macromolecular drugs based on the EPR effect ☆,” vol. 63, p. 6, 2010, doi: 10.1016/j.addr.2010.03.011.
- [9] V. Sanna and M. Sechi, “Nanoparticle therapeutics for prostate cancer treatment,” *Maturitas*, vol. 73, no. 1, pp. 27–32, Sep. 2012, doi: 10.1016/J.MATURITAS.2012.01.016.
- [10] H. S. Nalwa, “A special issue on reviews in nanomedicine, drug delivery and vaccine development,” *J. Biomed. Nanotechnol.*, vol. 10, no. 9, pp. 1635–1640, 2014, doi: 10.1166/JBN.2014.2033.
- [11] A. B. Gutman and E. B. Gutman, “AN ‘ACID’ PHOSPHATASE OCCURRING IN THE SERUM OF PATIENTS WITH METASTASIZING CARCINOMA OF THE PROSTATE GLAND.”
- [12] S. Veeramani *et al.*, “Cellular prostatic acid phosphatase: a protein tyrosine phosphatase involved in androgen-independent proliferation of prostate cancer,” *Endocr. Relat. Cancer*, vol. 12, no. 4, pp. 805–822, Dec. 2005, doi: 10.1677/ERC.1.00950.
- [13] H. B. Carter *et al.*, “Percentage of free prostate-specific antigen in sera predicts aggressiveness of prostate cancer a decade before diagnosis,” *Urology*, vol. 49, no. 3, pp. 379–384, May 1997, doi: 10.1016/S0090-4295(96)00629-2.
- [14] J. I. Epstein, P. C. Walsh, M. Carmichael, and C. B. Brendler, “Pathologic and Clinical Findings to Predict Tumor Extent of Nonpalpable (Stage T1 c) Prostate Cancer,” *JAMA*, vol. 271, no. 5, pp. 368–374, Feb. 1994, doi: 10.1001/JAMA.1994.03510290050036.
- [15] H. B. Carter *et al.*, “Detection of Life-Threatening Prostate Cancer With Prostate-Specific Antigen Velocity During a Window of Curability,” *JNCI J. Natl. Cancer Inst.*, vol. 98, no. 21, pp. 1521–1527, Nov. 2006, doi: 10.1093/JNCI/DJJ410.
- [16] S. J. Freedland *et al.*, “Risk of prostate cancer-specific mortality following biochemical recurrence after radical prostatectomy,” *JAMA*, vol. 294, no. 4, pp. 433–439, Jul. 2005, doi: 10.1001/JAMA.294.4.433.
- [17] D. W. Lin, “EPCA-2: A highly specific serum marker for prostate cancer. Leman ES, Cannon GW, Trock BJ, Sokoll LJ, Chan DW, Mangold L, Partin AW, Getzenberg RH, Brady Urological Institute, Johns Hopkins University School of Medicine, Baltimore, MD,” *Urol. Oncol. Semin. Orig. Investig.*, vol. 25, no. 6, p. 528, Nov. 2007, doi: 10.1016/J.UROLONC.2007.10.011.
- [18] H. Lee *et al.*, “Alpha-Methylacyl-CoA Racemase (AMACR), a Potential New Biomarker for Glioblastoma,” *Front. Oncol.*, vol. 10, no. October, pp. 1–7, 2020, doi: 10.3389/fonc.2020.550673.
- [19] M. A. Rubin *et al.*, “alpha-Methylacyl coenzyme A racemase as a tissue biomarker for prostate cancer,” *JAMA*, vol. 287, no. 13, pp. 1662–1670, Apr. 2002, doi: 10.1001/JAMA.287.13.1662.
- [20] W.-H. Lee *et al.*, “Cytidine methylation of regulatory sequences near the a-class glutathione S-transferase gene accompanies human prostatic carcinogenesis,” *Proc.*

*Nati. Acad. Sci. USA*, vol. 91, pp. 11733–11737, 1994.

- [21] S. V. Harden, Z. Guo, J. I. Epstein, and D. Sidransky, “Quantitative Gstp1 Methylation Clearly Distinguishes Benign Prostatic Tissue And Limited Prostate Adenocarcinoma,” *J. Urol.*, vol. 169, no. 3, pp. 1138–1142, Mar. 2003, doi: 10.1097/01.JU.0000049627.90307.4D.
- [22] S. A. Tomlins *et al.*, “Recurrent Fusion of TMPRSS2 and ETS Transcription Factor Genes in Prostate Cancer.”
- [23] M. J. Bussemakers *et al.*, “DD3: a new prostate-specific gene, highly overexpressed in prostate cancer - PubMed,” *public*, 1999.
- [24] L. C. Tsai, H. Y. Hsieh, K. Y. Lu, S. Y. Wang, and F. L. Mi, “EGCG/gelatin-doxorubicin gold nanoparticles enhance therapeutic efficacy of doxorubicin for prostate cancer treatment,” <https://doi.org/10.2217/nnm.15.183>, vol. 11, no. 1, pp. 9–30, Dec. 2015, doi: 10.2217/NNM.15.183.
- [25] P. Tambe, P. Kumar, K. M. Paknikar, and V. Gajbhiye, “Decapeptide functionalized targeted mesoporous silica nanoparticles with doxorubicin exhibit enhanced apoptotic effect in breast and prostate cancer cells,” *Int. J. Nanomedicine*, vol. 13, p. 7669, 2018, doi: 10.2147/IJN.S184634.
- [26] S. Kamal Amit, M. Mezbah Uddin, R. Rahman, S. M. Rezwanul Islam, and M. Samad Khan, “A review on mechanisms and commercial aspects of food preservation and processing,” *Agric. Food Secur.*, vol. 6, p. 51, 2017, doi: 10.1186/s40066-017-0130-8.
- [27] G. Liu, R. Nie, Y. Liu, and A. Mehmood, “Combined antimicrobial effect of bacteriocins with other hurdles of physicochemic and microbiome to prolong shelf life of food: A review,” *Sci. Total Environ.*, vol. 825, p. 154058, Jun. 2022, doi: 10.1016/J.SCITOTENV.2022.154058.
- [28] Y. ROOS and M. KAREL, “Plasticizing Effect of Water on Thermal Behavior and Crystallization of Amorphous Food Models,” *J. Food Sci.*, vol. 56, no. 1, pp. 38–43, Jan. 1991, doi: 10.1111/J.1365-2621.1991.TB07970.X.
- [29] R. Steele, *Understanding and Measuring the Shelf-Life of Food - Google Books*. Boca Raton, Fla.: CRC Press, 2009.
- [30] O. A. FABUNMI, Z. D. OSUNDE, B. A. ALABADAN, and A. A. JIGAM, “INFLUENCE OF MOISTURE CONTENT AND TEMPERATURE INTERACTION ON MECHANICAL PROPERTIES OF DESMA (Novella pentadesma) SEED,” *J. Adv. Food Sci. Technol.*, pp. 81–85, Jul. 2015, doi: 10.2/JQUERY.MIN.JS.
- [31] A. A. Kader, D. Zagory, and E. L. Kerbel, “Modified atmosphere packaging of fruits and vegetables,” <http://dx.doi.org/10.1080/10408398909527490>, vol. 28, no. 1, pp. 1–30, Jan. 2009, doi: 10.1080/10408398909527490.
- [32] G. W. WHITE and S. H. CAKEBREAD, “The glassy state in certain sugar-containing food products \*,” *Int. J. Food Sci. Technol.*, vol. 1, no. 1, pp. 73–82, Mar. 1966, doi: 10.1111/J.1365-2621.1966.TB01031.X.
- [33] H. Levine and L. Slade, “A polymer physico-chemical approach to the study of commercial starch hydrolysis products (SHPs),” *Carbohydr. Polym.*, vol. 6, no. 3, pp. 213–244, Jan. 1986, doi: 10.1016/0144-8617(86)90021-4.

- [34] D. S. REID, "Optimizing the quality of frozen foods : understanding and minimizing the effects of each stage in the production of frozen foods, particularly blanching and frozen storage, can optimize their quality," *Food Technol.*, vol. 44, no. 7, pp. 78,80-82 [4 p.], 1990.
- [35] H. Levine and L. Slade, "PRINCIPLES OF 'CRYOSTABILIZATION' TECHNOLOGY FROM STRUCTURE/PROPERTY RELATIONSHIPS OF CARBOHYDRATE/WATER SYSTEMS-A REVIEW," *Cryo-Letters*, vol. 9, p. 43, 1986.
- [36] S. Rawat, "Food Spoilage: Microorganisms and their prevention," *Pelagia Res. Libr. Asian J. Plant Sci. Res.*, vol. 5, no. 4, p. 11, 2015.
- [37] Y. Tianli, Z. Jiangbo, and Y. Yahong, "Spoilage by Alicyclobacillus Bacteria in Juice and Beverage Products: Chemical, Physical, and Combined Control Methods," *Compr. Rev. Food Sci. Food Saf.*, vol. 13, no. 5, pp. 771–797, Sep. 2014, doi: 10.1111/1541-4337.12093.
- [38] J. M. Jay, *Modern Food Microbiology Sixth Edition*, 6th ed. Gaithersburg, Maryland: An Aspen, 2000.
- [39] L. D. Rogers and C. M. C. Overall, "Proteolytic post-translational modification of proteins: Proteomic tools and methodology," *Mol. Cell. Proteomics*, vol. 12, no. 12, pp. 3532–3542, Dec. 2013, doi: 10.1074/mcp.M113.031310.
- [40] P. Format and P. Isbn, "Herbal Foods and its Medicinal Values," pp. 1–25.
- [41] S. S.- and O. Enfors, "Food. Sven-Olof Enfors KTH - Biotechnology Stockholm S.-O. Enfors: Food microbiology - PDF Free Download," 2008. [Online]. Available: <https://docplayer.net/28034400-Food-sven-olof-enfors-kth-biotechnology-stockholm-s-o-enfors-food-microbiology.html>. [Accessed: 27-Aug-2022].
- [42] F. Rodriguez and R. Mesler, "Some drops don't splash," *J. Colloid Interface Sci.*, vol. 106, no. 2, pp. 347–352, 1985, doi: 10.1016/S0021-9797(85)80008-4.
- [43] K. Cooksey, "Effectiveness of antimicrobial food packaging materials," <https://doi.org/10.1080/02652030500246164>, vol. 22, no. 10, pp. 980–987, Oct. 2007, doi: 10.1080/02652030500246164.
- [44] J. H. Han and J. D. Floros, "Casting antimicrobial packaging films and measuring their physical properties and antimicrobial activity," *J. Plast. Film Sheeting*, vol. 13, no. 4, pp. 287–298, 1997, doi: 10.1177/875608799701300405.
- [45] R. Ahvenainen, Ed., *Novel Food Packaging Techniques - Google Books*. 2003.
- [46] A. L. Brody, E. R. Strupinsky, and L. R. Kline, *Active packaging for food application*. New York,: Tehnomic Publishing, 2001.

## **CHAPTER FOUR**

### **4.0 Sustained Release of AMACR Antibody-Conjugated and Free Doxorubicin from Silica Nanoparticles for Prostate Cancer Cell Growth Inhibition**

#### **4.1. Introduction**

Prostate cancer (PC) is the most frequently diagnosed cancer second most common type of cancer in men [1][2]. It was also the fifth major cause of cancer death in 2020, with about 1.4 million new cases and 375,000 deaths worldwide. Unfortunately, the pathogenesis of prostate cancer is not well understood [3], although age, family history of prostate cancer patients, and certain genetic mutations (e.g., BRCA1 and BRCA2) are known risk factors [1]. The highest incidence rates of PC are found in men of African descent that are also known to

be highly susceptible to high risks of PC [1]–[3]. However, PC is most likely to develop in men during the later stages of life [1]–[3]. Commonly used PC treatment methods include minimally invasive ablation therapies [4]–[6]; radiation therapy [7]; surgery, such as radical prostatectomy [7], [8]; hormone therapy [9]; cryotherapy [10], and chemotherapy [11].

In the case of bulk chemotherapy, significant side effects (erectile dysfunction, low libido, obesity, and bone mass loss) are often associated with the administration of relatively high concentrations of cancer drugs that need to diffuse through the blood vessels, capillaries, and pores to reach the intended cancer sites [12]. Furthermore, only a small fraction of the injected drugs reaches the intended tumour sites to induce the desired killing and shrinkage of prostate tumours. This makes the conventional bulk chemotherapy of PC difficult to achieve in practice.

There is, therefore, a need for improved methods for the localized delivery of cancer drugs to prostate tumour sites. This can be achieved by the combined use of localized drug delivery methods, and the sustained targeted delivery of cancer drugs with molecular recognition units that can interact directly with receptors that are overexpressed on the surfaces of prostate cancer cells. This need has stimulated several studies in which nanotechnology and targeted drugs have been used to develop novel methods for the detection and treatment of prostate cancer [13]–[16].

Mesoporous silica nanoparticles have been widely studied as sustained release cancer drug nanocarriers to inhibit cancer cell growth. [17]–[21] This is due to their unique properties, such as high total specific surface area, high pore volume, large loading capacity, biocompatibility, and easy surface modification [21].

Alpha-methylacyl-CoA racemase (AMACR) is a mitochondrial and peroxisomal enzyme involved in the beta-oxidation of dietary-branched fatty acids and C-27 bile acid intermediates [22]. An alyses of 22 studies involving 4385 participants concluded that

AMACR receptors are overexpressed in prostate cancers compared to lower expression in normal and benign prostatic tissue [22]. A recent study found that AMACR knockdown in prostate cancer cells resulted in decreased cell proliferation and increased apoptosis, suggesting that AMACR has an oncogenic role in prostate cancer [23]. Thus, AMACR could be used as a biomarker of prostate cancer [22], [24], [25], and AMACR receptors could be targeted to increase the uptake of anticancer drugs, such as doxorubicin (DOX), through receptor-mediated endocytosis to specifically kill prostate cancer cells.

The possibility of developing localized drug delivery structures for inhibiting the growth of prostate cancer cells will be explored in the current work using silica nanoparticles in which a model free cancer drug (doxorubicin, DOX) and a model targeted cancer drug (AMACR-conjugated DOX, DOX-A) will be released locally to target overexpressed AMACR receptors on the surfaces of prostate cancer cells. The localized and targeted release will be used to reduce the viability of prostate cancer cells under *in vitro* conditions. The thermodynamics and kinetics of drug release will also be discussed, along with the implications of the results for the development of sustained-release drug delivery systems for the targeted and localized treatment of prostate cancer.

In this study, we will test the hypotheses that reducing the pore sizes of the silica nanoparticles will slow down the *in vitro* release of the drugs (DOX and DOX-A), while capping the drug-loaded nanoparticles with dextran will further slowdown and prolong drug release to inhibit prostate cancer cell growth *in vitro*. Hence, mesoporous silica nanoparticles will be synthesized and functionalized with phenylboronic acid groups to reduce their pore sizes. The nanoparticles will then be loaded with the model cancer drugs (DOX and DOX-A) and capped with dextran to produce different drug-loaded nanoparticle formulations.

## **4.2. Materials and methods**

### **4.3. Materials**

Tetraethyl orthosilicate (TEOS, 99%), N-cetyltrimethylammonium bromide (CTAB), 4-carboxyphenylboronic acid (CPBA), 1-ethyl-3-(3-dimethylaminopropyl) carbodiimide hydrochloride (EDC), N-hydroxysuccinimide (NHS), dextran and ethanol were purchased from Sigma-Aldrich, St. Louis, MO, USA. Alpha methyl Acyl-CoA racemase (AMACR) peptide (~54 kDa) was procured from Bio SB, Santa Barbara, CA, USA. Sodium hydrophosphite hydrated LR, sodium hydrogen orthophosphate dehydrates, succinic anhydride, N, N-dimethylformamide (DMF), paraffin liquid heavy and sodium hydroxide flakes were purchased from Fisher Scientific, Waltham, MA, USA. Dextran from *Leuconostoc mesenteroides* (MW approx. 50 kDa), was purchased from Sigma Aldrich, Saint Louis, MO, USA. 3-Aminopropyl triethoxysilane (APTES) was obtained from Alfa Aesar, Haverhill, MA, USA, whereas doxorubicin hydrochloride salt was supplied by LC Laboratories, Woburn, MA, USA. Toluene and hydrochloric acid were purchased from Merck, Darmstadt, Germany. All chemicals were used as received. All cell culture reagents were procured from Thermo Fisher Scientific, Waltham, MA, USA, unless otherwise stated.

#### **4.3.1 Synthesis of MCM-41 silica nanoparticles**

MCM-41 (Mobil Composition of Matter No.41) silica nanoparticles were synthesized according to the method reported by the Mobil group [26]. Briefly, 1.0 g of N-cetyltrimethylammonium bromide (CTAB) and 0.28 g of sodium hydroxide (NaOH) were both dissolved in 480 mL of Millipore water under continuous stirring at 600 rpm at 80°C in a glass bath containing paraffin and a magnetic bead to ensure homogeneity in the heating process. Next, 5 mL of tetraethyl orthosilicate (TEOS) solution was added dropwise to the CTAB/NaOH solution. After 2 hours of stirring, the white solution formed was centrifuged at

12000 rpm for 5 minutes and the white precipitate was washed with Millipore water and ethanol and dried in oven at 60°C overnight. To knockoff the CTAB surfactant, 50 mL of ethanol was added to the white substance and the pH was adjusted to 1 with concentrated hydrochloric acid. Then, the mixture was refluxed for 6 hours and washed with ethanol three times to obtain MCM-41 silica nanoparticles, which were dried in a vacuum oven at 60°C for 6 hours. The dried sample was ground with a mortar and pestle to obtain a white powdered product.

#### **4.3.2. Synthesis of phenylboronic acid-functionalized MCM-41 silica nanoparticles:**

First, silanization of the silica nanoparticles was by adding 1.0 mL of 3-aminopropyl triethoxysilane (APTES) to 1.0 g of the synthesized MCM-41 in a nitrogen gas environment, followed by the addition of 80 mL of anhydrous toluene and refluxing under stirring for 24 hours to introduce amino groups to the nanoparticles. Afterwards, the resulting mixture was centrifuged at 12 000 rpm for 5 minutes and the pellet washed extensively with toluene, hexane and ethanol, and dried in a vacuum oven at 80°C for 6 hours. The amount of amino groups in 1.0 mg of the silanized MCM-41 nanoparticles (referred to as MCM-N), was estimated by the ninhydrin test [27], [28] to be approximately 30.27 wt.%.

Subsequently, phenylboronic acid acid groups were attached to the MCM-N nanoparticles through the amino groups. First, 0.4 g of EDC and 0.2 g of NHS were dissolved in 10 mL of dry DMF in nitrogen gas inert environment, followed by the addition of 0.3 g of 4-carboxyphenylboronic acid (CPBA) under continuous stirring at 500 rpm at room temperature for 15 minutes. Afterwards, a dispersion of MCM-N in 40 mL of dry DMF was added to the mixture and stirred for another 24 hours to tether the phenylboronic acid groups from CPBA to the amine groups attached to the MCM-N nanoparticles.

The functionalization process is illustrated in Figure 4.1. The resulting mixture was centrifuged at 12000 rpm for 5 minutes. The pellet was washed with DMF, Millipore water and ethanol, and dried at 60°C in a vacuum oven for 6 hours to obtain the phenylboronic acid -functionalized MCM-41 silica nanoparticles (herein referred to as MCM-B in this paper).

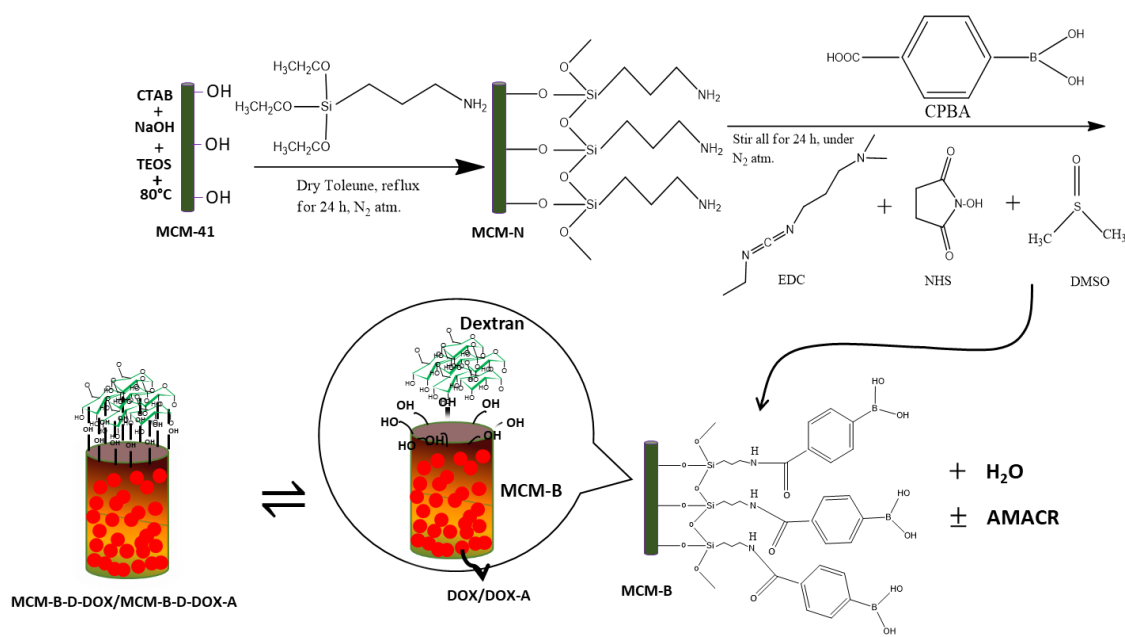


Figure 4.1: A schematic showing the steps

of silanizing the silica nanoparticles (MCM-41) with amino groups (MCM-N) and followed by phenylboronic acid functionalization (MCM-B) before loading them with cancer drugs (DOX and DOX-A) and then capping the MCM-B nanoparticles with dextran.

#### 4.3.3. Conjugation of doxorubicin with AMACR peptide

The conjugation was done by weighing 1.0 mg of DOX and adding it to 0.5 ml of dimethyl sulfoxide (DMSO) and 88.2 µl of 2 mg/ml EDC in 0.1 M MES buffer (pH 6.0) under vigorous stirring for 40 minutes in the dark. 105.9 µl of 2 mg/ml NHS in 0.1 M MES buffer (pH 6.0) was then added to the reaction mixture under stirring for 20 minutes. AMACR solution was prepared by adding 15 µl AMACR to 1.2 ml of a 0.1 M NaPO<sub>4</sub>/0.15 M NaCl solution with a pH of 7.5. The AMACR solution was added to the reaction mixture in the dark. Then, 0.4ml of DMSO: Water (7.5: 2.5) was added to the reaction under gradual stirring

in ice for 5 hours to complete the conjugation process. Excess AMACR was removed from the conjugated DOX solution using a combination of 3 kDa Amicon Ultra-4 Centrifugal Filters Units, and Amicon Pro Purification System.

#### **4.3.4. Preparation of drug-loaded silica nanoparticles**

The free doxorubicin (DOX) and AMACR-conjugated DOX (DOX-A) drugs were loaded into the bare (MCM-41) and phenylboronic acid -functionalized (MCM-B) silica nanoparticles. This was done by adding 1 ml solutions of 2 mg/mL (in terms of their doxorubicin content only) of DOX or DOX-A (in PBS pH 7.40) to 10 mg of the different nanoparticles, stirring for 24 hours at room temperature, and centrifuging at 4000 rpm for 5 minutes. The pellet was then frozen at -80°C for 2 hours and lyophilized at -105°C for 48 hours using a VirTis SP Scientific BenchTop Pro Lyophilizer. The DOX-loaded MCM-41 and MCM-B nanoparticles were designated as MCM-41-DOX and MCM-B-DOX, respectively. On the other hand, their DOX-A-loaded counterparts were designated as MCM-41-DOX-A and MCM-B-DOX-A, respectively. Prior to drug loading, the concentration of doxorubicin in DOX-A was estimated through UV-Vis measurements at 484 nm (UV-1900, Shimadzu, Tokyo, Japan).

Some of the drug-loaded MCM-B nanoparticles were capped with dextran to slow down the release of drugs from the silica nanoparticle pores after loading with drugs, as illustrated in Figure 4.1. The capping was done by adding 20% dextran (MW approx. 50 kDa) (in PBS pH 7.4) to the drug-loaded MCM-B nanoparticles and homogenizing with an Ultra Turrax T10 basic homogenizer at 30000 rpm for 30 seconds. After centrifuging at 1000 rpm for 5 minutes, excess dextran solution was removed, and the pellet was lyophilized for 48 hours. The dextran-capped MCM-B, MCM-B-DOX, and MCM-B-DOX-A nanoparticles were designated as MCM-B-D, MCM-B-D-DOX, and MCM-B-D-DOX-A, respectively. The amount of drug effectively loaded into each nanoparticle formulation was estimated through

UV-Vis measurements at 484 nm (UV-1900, Shimadzu, Tokyo, Japan) to determine the concentrations of the stock drug suspension before and after drug loading. The encapsulation efficiency (EE) was then determined from equation 1.

$$EE = \frac{C_i - C_f}{C_i} \times 100 \quad 4.1$$

where  $C_i$  is the concentration of the stock drug suspension before loading and  $C_f$  is the concentration of the stock drug suspension after loading.

#### **4.3.5. Characterization of the nanoparticles**

Fourier-transform infrared spectroscopy (FTIR) was used to determine the chemical bonds/functional groups that were associated with the drug-loaded and unloaded silica nanoparticles. FTIR spectra of the lyophilized samples were obtained from an FTIR spectrometer (IRSpirit, Shimadzu, Kyoto, Japan) from an average of 128 scans at a resolution of  $2 \text{ cm}^{-1}$  over a wavenumber range of  $400 - 4000 \text{ cm}^{-1}$ .

Thermogravimetric analysis (TGA) was used to characterize the thermal stability of the nanoparticles. Thermograms of the lyophilized samples were obtained from a TG 209 F1 Libra thermogravimetric analyzer (NETZSCH Instruments, Selb, Germany) in the temperature range of room temperature (RT) –  $900 \text{ }^\circ\text{C}$  at a heating rate of  $10^\circ\text{C}/\text{min}$  in a nitrogen atmosphere with a  $20 \text{ ml}/\text{min}$  flow rate.

Nitrogen sorption analysis was carried out on the nanoparticles to determine their specific surface areas using BET (Brunauer-Emmett-Teller) theory, and their pore diameters and pore volumes using the BJH (Barrett-Joyner-Halenda) method. To this effect,  $40 \text{ mg}$  of the nanoparticles were weighed and degassed for 6 hours under vacuum at  $105^\circ\text{C}$ . The degassed samples were then placed in sample tubes for nitrogen adsorption-desorption measurements at different relative pressures ( $P/P_0$ ) using the Quantachrome Autosorb iQ gas sorption analyzer. Nitrogen adsorption-desorption isotherms were obtained at  $77 \text{ K}$  and the BET

theory and BJH method were used to estimate the specific surface area and pore distribution, respectively.

X-ray diffraction (XRD) analysis was carried out on the samples using a Rigaku D/max-3A diffractometer (Rigaku Corporation, Tokyo, Japan). XRD diffractograms were obtained using a using Cu K $\alpha$  radiation ( $\lambda = 1.54 \text{ \AA}$ ). The samples were scanned over a range of  $2\theta$  angles between  $1^\circ$  and  $10^\circ$  at a step size of  $0.05^\circ$  and scan speed of 1.0 second per step.

The morphologies of the nanoparticles were examined using field emission scanning electron microscopy (FE-SEM) and transmission electron microscopy (TEM). For FE-SEM analysis, the nanoparticles were suspended in deionized water (1 mg/mL), sonicated for 30 minutes, and deposited on a freshly cleaved mica surface to dry. After drying, the samples were coated with gold/palladium and loaded into an FE-SEM microscope (Zeiss Gemini SEM 560, Jena, Germany) equipped with energy dispersive X-ray spectroscope (EDS) to visualize the surface morphology of the nanoparticles before and after functionalization and to determine the elemental composition of the nanoparticles. In the case of TEM analysis, the nanoparticles were dispersed in ethanol and left overnight to dry before being collected with lacey carbon films and deposited on TEM grids. Detailed morphologies of the nanoparticles were then visualized using a JEOL 4000EX high-resolution TEM microscope (JEOL, Tokyo, Japan).

Zeta potential measurements were carried out on the nanoparticles to determine their surface charge. Samples were prepared by dispersing 3 mg of the nanoparticles in 1 ml of deionized water under sonication for 30 minutes. 200  $\mu\text{L}$  of the suspensions were loaded into folded capillary zeta cells (DTS1070, Malvern Instruments, Malvern, UK) and run in a Zetasizer Nano ZS analyzer (Malvern Instruments, Malvern, UK).

#### **4.4 *In Vitro* drug release**

*In vitro* drug release studies were used to characterize the release profiles of DOX and DOX-A and to determine the kinetics and thermodynamics of sustained drug release from the silica nanoparticles. For each drug-loaded nanoparticle formulation, 5 mg of the lyophilized DOX- and DOX-A-loaded nanoparticles (MCM-41 and MCM-B) were suspended in a centrifuge tube containing 5 ml PBS buffer (at pH 6.50 and 7.40). This was used to replicate the tumor microenvironment, which is usually acidic at about pH 6.50, and the physiological condition of the body at pH 7.40 [29]. The samples were prepared in triplicates. The centrifuge tubes were placed on orbital shakers within an incubator shaker (Innova 44 Incubator, Console Incubator Shaker, New Brunswick, NJ, USA) that was operated at 60 rpm at temperatures of 37°C, 41°C and 44°C. After 3, 6, 12 and then subsequently at 24-hour intervals over 30 days, 750 µl aliquots were taken out of the tubes after centrifuging them for 5 minutes at 4000 rpm. The tubes were replenished with 750 µl of fresh PBS, before returning them to the incubator shaker to continue the drug release studies. The absorbance values of the released drugs (DOX or DOX-A) in the aliquots were measured using a UV-Vis spectrophotometer (UV-1900, Shimadzu, Tokyo, Japan) at a wavelength of 484 nm. The concentrations of the released drugs (DOX or DOX-A) from the drug-loaded silica nanoparticle formulations were then interpolated from their respective standard curves.

## **4.5. Modeling of drug release**

### **4.5.1 *In vitro* drug release kinetics**

To understand the drug release kinetics, various mathematical models were used to fit the *in vitro* drug release data. These included: the zeroth order, first order, second order, Higuchi, and Korsmeyer-Peppas models [30], [31] that are described briefly in this section.

Zeroth order release describes the release of drugs from a material medium that does not disintegrate with time. It also takes time for the medium to elute its content under equilibrium conditions [32], [33]. The zeroth-order model can be expressed as:

$$C_t = C_0 + k_0 t \quad 4.2$$

where  $C_t$  represents the amount of active agent released in time  $t$ ,  $C_0$  is the initial concentration of the active agent released and  $k_0$  is the zero-order constant [32], [34].

The first order model, describes the rate at which active agents gets used up or the rate of release of the agent from a biomaterial [31], [32]. First order kinetics can be represented by:

$$\frac{dC}{dt} = -k_1 C \quad 4.3$$

Hence, the rate of change in concentration with respect to change in time is dependent only on concentration, where  $k_1$  is the first order release constant [32].

Second order kinetics model, on the other hand, can be represented by the following expression [35]–[37]:

$$\frac{1}{C_t} = \frac{1}{C_0} + k_2 t \quad 4.4$$

where  $k_2$  represents the second order rate constant,  $C_0$  and  $C_t$  represents the initial and the final concentration of the drug at time  $t$ .

Furthermore, the Higuchi model describes the release of active agents from a solid and/or a semi-solid matrix under conditions in which the active agent is less soluble or very soluble in the matrix. Hence, the amount of drug released (e.g. concentration) is proportional to the square root of time [32], [34], [38]. This is given by:

$$C_t = k_H \sqrt{t}$$

4.5

In cases in which there is a change in concentration from  $C_0$  to  $C_t$  and  $k_H$ , the Higuchi release constant, then the Higuchi model can be expressed as:

$$C_t = C_0 + k_H\sqrt{t}$$

4.6

Finally, the Korsmeyer-Peppas model describes the rate at which a polymeric material elutes its content. This model is also called the power law model, which provides a relationship between the release of the active agent (from the drug formulation) and the time taken for the release [32], [39], [40],[41].

$$\frac{M_t}{M_\infty} = kt^n \quad 4.7$$

where,  $M_\infty$ ,  $M_t$ ,  $t$ ,  $k$  and  $n$  represent the amount of drug released at equilibrium, the quantity of drug release in time  $t$ , period of drug release, release rate constant and release exponent, respectively. The above equation can also be represented in terms of concentration, where  $C_i$  is the concentration of the active agent at time  $t$  and  $C_\infty$  represents the as shown below.

$$\frac{C_t}{C_\infty} = kt^n$$

4.8

Hence, by taking the natural logarithm of both sides of equation 4.8, we obtain equation 4.9

$$\ln\left(\frac{C_t}{C_\infty}\right) = \ln k + n \ln t$$

4.9

The mechanism of drug release from the various silica nanoparticle formulations was examined by fitting the drug release results to the five kinetic models presented above. The  $R^2$  values closest to 1 were used to identify the models with the best fit [31].

#### **4.5.2. *In vitro* drug release thermodynamics**

This section presents the theoretical framework that was used to determine the thermodynamic parameters associated with controlled drug release from the silica nanoparticles. These include: the activation energy ( $E_a$ ) [42]; the enthalpy change ( $\Delta H$ ); the sum of the internal energy change and the change in the product of the pressure and volume

of a thermodynamic system [43]; the Gibbs free energy change ( $\Delta G$ ) [44], and the change in entropy ( $\Delta S$ ) [44]. These were determined using methods described in detail in prior studies [15]. The Arrhenius equation (equation 10) was used to determine the activation energy ( $E_a$ ) from the slope of the plot of  $\ln k_t$  versus  $1/T$ .

$$k_t = D_f e^{-\frac{E_a}{RT}} \quad 4.10$$

$$\ln k_t = \ln D_f - \frac{E_a}{R} \frac{1}{T} \quad 4.11$$

The Eyring equation (equation 4.12) was used to calculate the enthalpy change ( $\Delta H$ ) (from the slope) and the entropy change ( $\Delta S$ ) (from the intercept) of the plot of  $\ln k_t$  versus  $1/T$

$$\ln \frac{k_t}{T} = -\frac{\Delta H}{R} \frac{1}{T} + \ln \frac{\kappa k_B}{h} + \frac{\Delta S}{R} \quad 4.12$$

The change in Gibbs free energy ( $\Delta G$ ) was obtained from the following expression:

$$\Delta G = \Delta H - T\Delta S \quad 4.13$$

where  $R$  is the universal gas constant  $8.314 \text{ J mol}^{-1} \text{ K}^{-1}$ ,  $T$  is the absolute temperature in Kelvin,  $k_t$  is the thermodynamic equilibrium constant,  $E_a$  is the activation energy,  $\Delta S$  is the change in entropy,  $\Delta H$  is the change in enthalpy,  $\kappa$  is the transmission coefficient,  $k_B$  represents the Boltzmann constant,  $1.38065 \times 10^{-23} \text{ m}^2 \text{ kgs}^{-2} \text{ K}^{-1}$  and  $h$  represents the Planck's constant,  $6.626 \times 10^{-34} \text{ J sec}$ .

#### 4.6 *In vitro* cell viability

The *in vitro* viability of the prostate cancer cells with or without treatment with the DOX and DOX-A drug-loaded nanoparticles were determined using alamar blue assay to assess the cell metabolic activities, expressed as the percentage alamar blue reduction, as described previously [13], [31]. A larger percentage alamar blue reduction indicates that the cells are growing faster and, as a result, are more viable. Human prostate cancer cells (PC-3 cell line, ATCC-CRL-1435) was obtained from American Type Culture Collection (ATCC),

Manassas, VA, USA, and grown in a complete culture medium consisting of Kaighn's modification of Ham's medium (F-12K) supplemented with 10% fetal bovine serum (FBS) and 1% penicillin/streptomycin. The cells were maintained in a humidified incubator at 37 °C and 5% CO<sub>2</sub>. Cells were harvested at 70-80% confluence using 0.25% trypsin-EDTA solution and subcultured in fresh T75 flasks.

At passages 5-7, approximately 10<sup>4</sup> cells/well were seeded in 24-well plates (n = 3) and incubated overnight at 37 °C and 5% CO<sub>2</sub>. Subsequently, the culture medium in each well was replaced with 1 ml of culture medium containing 1.0 mg/ml of the drug-loaded nanoparticles. The amount of drugs contained in 1 mg of each drug-loaded nanoparticle formulation is summarized in Table S1. The cells were also treated with 1 ml of 15 µM of free DOX, 1 ml of 15 µM DOX-A and 1 ml of 1.0 mg/ml bare nanoparticles (MCM-41, MCM-B and MCM-B-D) as controls. The nanoparticles and drugs were exposed to UV light for 3 hours to sterilize them prior to adding them to the cells in the well plates.

At predetermined time intervals (0, 6, 24, 48, 72, and 96 hours) after treating the cells, the culture medium was replaced with culture medium containing 10% alamar blue reagent. After incubating for 3 hours at 37 °C and 5% CO<sub>2</sub>, 100 µL aliquots were transferred into black opaque 96-well plates for fluorescence intensity measurements (excitation/emission: 544/590 nm) using a 1420 Victor3 multilabel plate reader (Perkin Elmer, Waltham, MA, USA). The percentage alamar blue reduction was calculated using equations 4.14.

$$\% \text{ Alamar Blue Reduction} = \frac{FI_{\text{sample}} - FI_{10\%AB}}{FI_{100\%R} - FI_{10\%AB}} \times 100 \quad 4.14$$

where  $FI_{\text{sample}}$ ,  $FI_{10\%AB}$  and  $FI_{100\%R}$  represent the fluorescence intensity of treated cells, fluorescence intensity of 10% alamar blue, and fluorescence intensity of 100% reduced alamar blue, respectively.

#### **4.6.1 Immunofluorescence staining of AMACR receptors**

Immunofluorescence (IF) staining was used to study the distribution of AMACR receptors on the surfaces of the PC-3 prostate cancer cell lines. IF staining of the AMACR receptors on the PC-3 cancer cell lines were carried out as previously reported [13], [14] with modifications. Briefly,  $1 \times 10^5$  PC-3 cells were cultured on sterile coverslips (CELLTREAT, Pepperell, MA, USA) in 60 ×15 mm cell culture Petri dishes (CELLTREAT, Pepperell, MA, USA) containing 2 ml of culture medium. After incubating them in a humidified incubator at 37 °C and 5% CO<sub>2</sub> until 70-80% confluence, the cells were washed twice with 10% PBS solution and fixed with 4% paraformaldehyde for 15 minutes. The cells were then incubated with 0.1% Triton X-100 for 15 minutes to permeabilize them, followed by blocking with 5% normal goat serum (in PBS) for 1 hour at room temperature (25 °C). The cells were further incubated with the anti-AMACR (primary) antibody (Bio SB, Santa Barbara, CA, USA) for 3 hours at room temperature and rinsed with 10% PBS solution. This was followed by incubation with the secondary antibody (Goat anti-Mouse IgG (H + L) Superclonal, Alexa Fluor 488 conjugate) for 1 hour at room temperature and rinsing again thrice with 10% PBS solution. Finally, the nuclei were counterstained with 1 µg/mL of DAPI (in PBS) for 10 minutes and rinsed again four times with 10% PBS solution. The coverslips were then mounted with mounting medium on glass slides and sealed with nail polish. The stained cells were then visualized with a Leica SP5 Point Scanning Confocal Microscope (Leica, Buffalo Grove, IL, USA) to obtain representative fluorescence images of the nuclei (blue color) and AMACR receptors on the surface of the PC-3 cells (green colour).

#### **4.6.2. Drug release simulations**

The flux of drugs from the porous nanoparticle structures was modeled using the COMSOL 5.5 Multiphysics software package. Porous structures with different pore orientations were

considered in the models in which simplified homogeneity was assumed with appropriate transport across the porous surfaces [30].

That gives:

$$\frac{\partial c}{\partial x} + \nabla \cdot (-D\nabla c) = 0 \quad 4.15$$

where  $c$  represents concentration in mol/m<sup>3</sup> and the diffusivity  $D$  is given in m<sup>2</sup>/s of the solute. The use of the correct initial and boundary conditions is critical in fluid exchange and diffusion studies [45]. Three boundary conditions were chosen based on the initial entry point of the fluid into the nanoparticle either from the left, right, upper part or the lower part of the geometry, with the flux exit point being the point directly opposite the entry point in a 2D geometry and the insulating boundary, while the diffusion process is ongoing [30]. In the first phase of this simulation, the boundary conditions would be set based on some defining equations.

The first boundary condition corresponds to the fluid entry boundary, and it is set as the concentration boundary. This was expressed as [30], [46]:

$$c = c_0 \quad 4.16$$

where  $c_0$  is the initial concentration of the drug.

The second boundary condition represents the flux exit boundary [30], [46]. This was represented as:

$$(-D\nabla c) \cdot \mathbf{n} = k_m(c - c_1) \quad 4.17$$

Outside the porous nanoparticle,  $c_1$  is the concentration in the bulk solution and  $k_m$  represents the mass transfer coefficient in m/s.

The third boundary condition represents the insulating boundaries [45], [47], as show below.

$$(-D\nabla c) \cdot \mathbf{n} = 0 \quad 4.18$$

The initial condition is represented by an exponential function as shown below

$$c(t_0) = c_0 \exp(-ax^2) \quad 4.19$$

The second phase of this simulation uses a homogenous model which is in one dimension. It uses the effective properties for the modeling of fluid transport and as a result, the model equation becomes similar to the inhibited nano bubble transported through a porous medium [45], [48].

$$\varepsilon \frac{\partial c}{\partial x} + \nabla \cdot (-D^{\text{eff}} \nabla c) = 0 \quad 4.20$$

where  $\varepsilon$  and  $D^{\text{eff}}$  represent the average porosity and the effective diffusion coefficient, respectively.

### **4.6.3. Statistical analysis**

The results are presented as mean  $\pm$  standard deviation for three independent trials ( $n = 3$ ), unless otherwise indicated. One-way ANOVA was used to analyze the differences in drug release from the various nanoparticle formulations, whereas two-way ANOVA was used to analyze the differences in cell viability after treatment with the nanoparticle formulations. Post hoc Tukey tests were used to identify the statistically significant groups, where  $p$  values  $< 0.05$  were considered statistically significant. The analyses were carried out using the SPSS package (v28).

## **4.7. Results**

### **4.7.1. Physicochemical properties of the silica nanoparticles**

To confirm the silanization and functionalization of the silica nanoparticles, the FTIR spectra of the MCM-41, MCM-N, MCM-B, and MCM-B-D are compared in Figure 4.2.

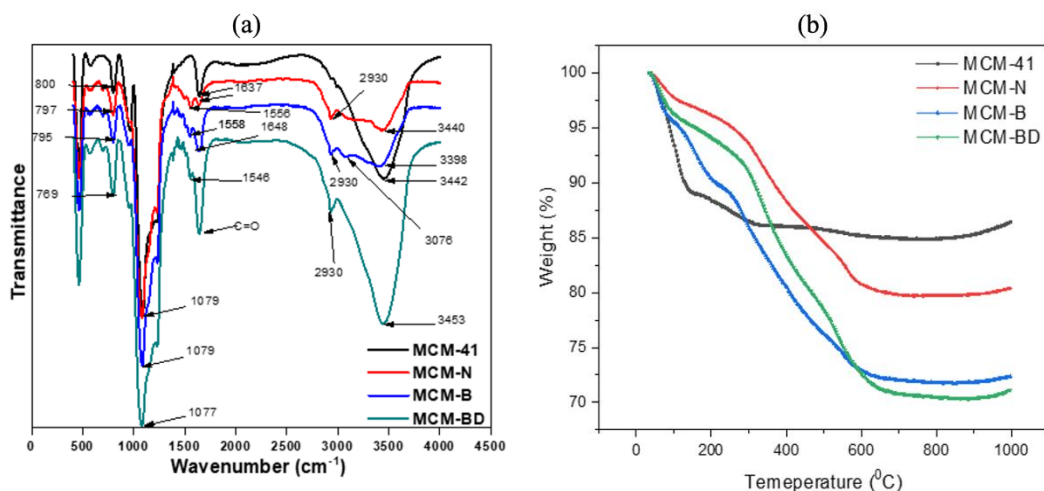


Figure 4.2: (a) FTIR spectra of the nanoparticles (b) TGA analysis of the nanoparticles

The spectra confirmed the existence of the amino groups, the O-H group and the presence of phenylboronic acid on the silica nanoparticles [48]. The characteristic peaks for silica were observed at 798, 960, and 1079 cm<sup>-1</sup> due to Si-O-Si symmetric stretching, Si-OH stretching, Si-O-Si asymmetric stretching vibrations, respectively, in all the nanoparticles. After grafting amino groups, obvious changes occurred in their spectra. The distinct bands appeared at 3364, 2930 and 1559.8 cm<sup>-1</sup> owing to vibrations of the -NH<sub>2</sub> and N-H<sup>+</sup> while the Si-OH band at 960 cm<sup>-1</sup> was attenuated, suggesting that most of surface silanols were reacted with aminosilane [49]. The formation of MCM-B and attachment of phenylboronic acid can also be seen (Figure 4.2a). A sharp band of an amine group is present at 3440 cm<sup>-1</sup> in MCM-N nanoparticles, which disappears in the MCM-B nanoparticles and a broad peak appears at 3453 cm<sup>-1</sup>, indicating hydroxyl groups of phenylboronic acid [50]. The C-H stretching vibrations are also present at 3042 cm<sup>-1</sup>.

Amide bond formation of 4-carboxy phenylboronic acid with MCM-N and carbonyl at 1627 cm<sup>-1</sup> and 1654 cm<sup>-1</sup>, respectively, confirm the formation of MCM-B [51], [52]. The signals corresponding to the C=O and C-N stretches of the formed APTES linkages between the silica and the phenylboronic acid functionality in compound silica at 1654 cm<sup>-1</sup> may be

merged with the band of surface hydroxyl groups of silica and Si–O–Si band, respectively [48], [53].

The characteristic peaks of both dextran and MCM-B are seen in Figure 4.2a where the spectrum for the dextran-capped MCM-B-D is shown. In this, the distinctive vibration bands at  $3453\text{cm}^{-1}$  aligns with the classical signal of the polysaccharide dextran [54], [55]. We also observed bands at  $942$  and  $800\text{ cm}^{-1}$  representing the pyranose ring and  $\alpha$ -D-glucose, respectively[55]. The thermal stability of the nanoparticles was tested before functionalization, and after functionalization, using thermogravimetric analysis. From Figure 4.2b, the percentage weight loss due to decomposition of the nanoparticles; MCM-41, MCM-N, MCM-B and MCM-B-D were determined to be approx. 15%, 20%, 27.5%, and 30%, respectively. These imply that functionalizing the silica nanoparticles increased the rate of decomposition owing to the decomposition of the additional groups like the amine group ( $-\text{NH}_2$ ) in MCM-N, phenylboronic acid group (B-O) in MCM-B, and dextran,  $(\text{C}_6\text{H}_{10}\text{O}_6)_n$ , in MCM-B-D nanoparticles.

The results of the nitrogen sorption analysis [56] are also presented in this section and summarized in Figure 4.3.

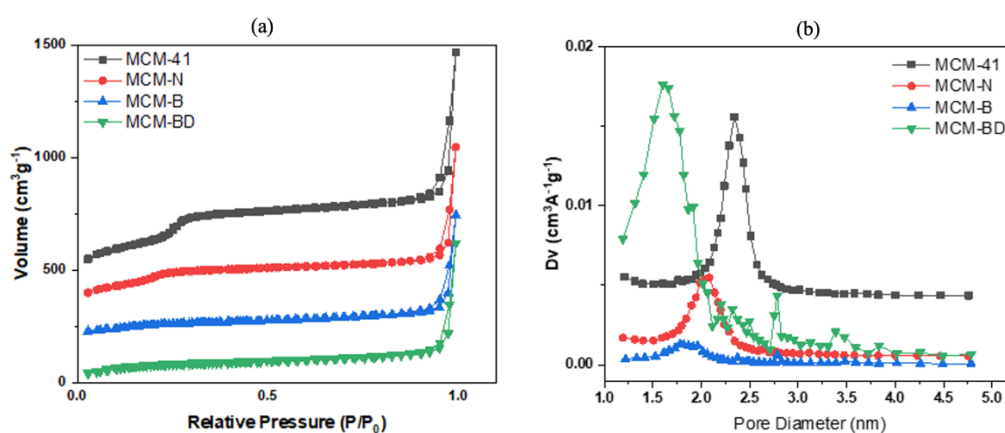


Figure 4.3: Nitrogen sorption analysis of the nanoparticles, showing the (a) nitrogen adsorption and desorption isotherms and (b) the Barret-Joyner-Halenda pore size distribution curves of the nanoparticles.

The synthesized MCM-41 nanoparticles had a specific surface area, pore volume and pore diameter of  $1123.335 \text{ m}^2\text{g}^{-1}$ ,  $1.701 \text{ m}^3\text{g}^{-1}$  and  $2.342 \text{ nm}$ , respectively. The BJH pore diameter was between  $2 - 50 \text{ nm}$ , indicating that the synthesized MCM-41 silica nanoparticles were mesoporous, according to the IUPAC nomenclature [57]. The silanized nanoparticle, MCM-N, had lower specific surface area, pore volume and pore diameter values of  $712.773 \text{ m}^2\text{g}^{-1}$ ,  $1.175 \text{ m}^3\text{g}^{-1}$  and  $2.0842 \text{ nm}$ , respectively, than the MCM-41 nanoparticles.

Further functionalization of MCM-N nanoparticle with the phenylboronic acid groups to MCM-B caused further reductions in the specific surface area, pore volume, and pore diameter to  $285.568 \text{ m}^2\text{g}^{-1}$ ,  $0.869 \text{ m}^3\text{g}^{-1}$  and  $1.781 \text{ nm}$ , respectively. Upon using dextran polymer to cap the pores of the MCM-B nanoparticles, slight increases were observed for the MCM-B-D than the MCM-B nanoparticles, such that the specific surface area and pore volume of MCM-B-D were greater than MCM-B by  $102.261 \text{ m}^2\text{g}^{-1}$ ,  $0.123 \text{ m}^3\text{g}^{-1}$ , whereas the pore diameter was  $0.178 \text{ nm}$  less than that of MCM-B. The increase in the specific surface area showed that there was proper capping of the pores and the reduction in pore diameter was also due to the interaction of the matrix of the functionalized silica with the dextran that lowered the diameter.

The hexagonal symmetry of the pore ordering is shown in the X-ray diffraction pattern of MCM-41 in Figure 4.4, which typically has four main reflection lines (d100, d110, d200, and d210) at low angles ( $2\theta = 10$ ). MCM-41 has no atomic crystallinity since it is made up of amorphous silica [58]. From the XRD spectra in Figure 4.4, the peak for MCM-N, MCM-B and MCM-B-D reduces in intensity, attributed to the functionalization effect of the amine group, phenylboronic acid group, and dextran capping, respectively. Hence, their peaks (100) occur at  $\sim 2.11^\circ$ , whereas that of MCM-BD occurs at  $1.57^\circ$ . Furthermore, there were two other peaks that occur at  $3.62^\circ$ ,  $4.18^\circ$  and at  $5.68^\circ$ , which correspond to (110), (200) and

(210), respectively. The peaks noticed at (110) and (200) are wide for MCM-41 and gradually disappear with further functionalization.

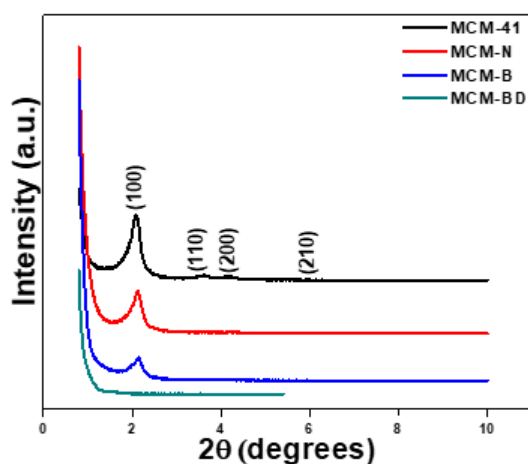


Figure 4.4: The XRD patterns of the nanoparticles

From the XRD spectra of all the nanoparticles, it is clear that surface functionalization of the MCM-41 with APTES and CPBA did not cause much alteration in the lattice of the silica. The broadening and gradual disappearance of the secondary peak could be due to the presence of some ligands on the pore surface of MCM-41 and or the functional groups that occupy the MCM-41 pores [59].

Figure 4.5 presents the surface morphologies and elemental analysis from representative FE-SEM images and EDS spectra of the synthesized MCM-B and MCM-B-D nanoparticles.

Figure 4.5a shows that the particles are spherical as reported in the literature [32], [60]. The EDS spectrum (Figure 4.5c) reveals the presence of silica (19.77 wt.%), confirming that the material is silica based; oxygen (52.21 wt.%), suggesting the existence of the Si-O-Si bond; nitrogen (2.54 wt.%), from the silanization that led to the formation of MCM-N, and boron (0.54 wt.%) from the functionalization with the phenylboronic acid groups from CPBA to form the MCM-B nanoparticles. Figure 4.5d presents an FE-SEM image of MCM-B-D nanoparticles. The observed agglomeration of the nanoparticles shows that the gating agent,

dextran, was responsible for the structure.

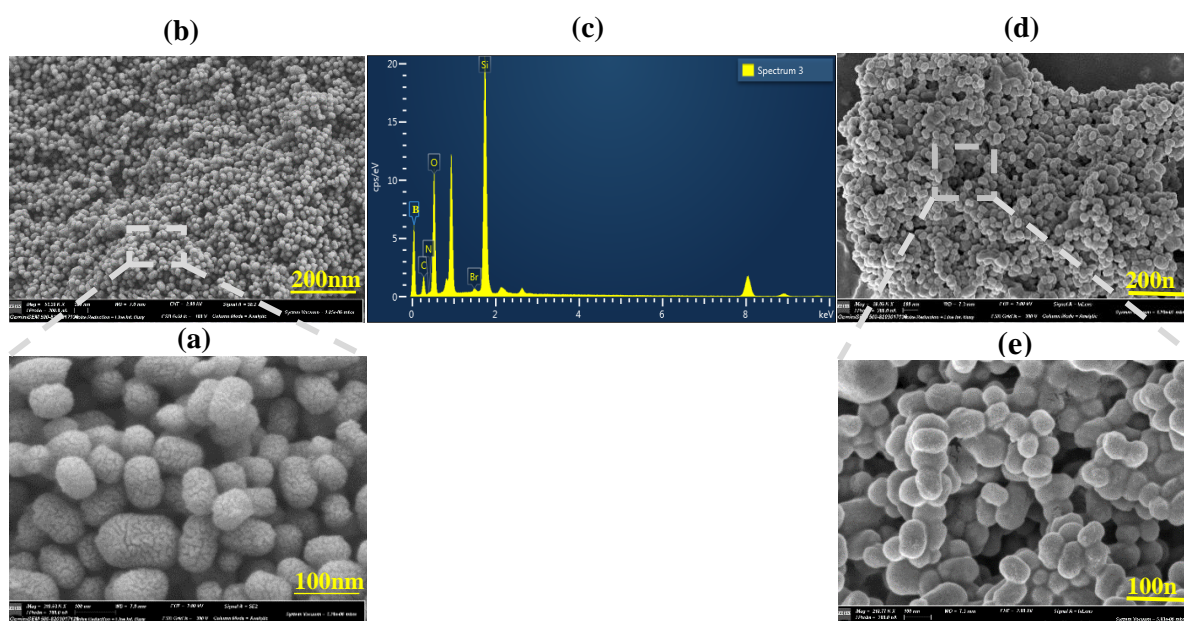
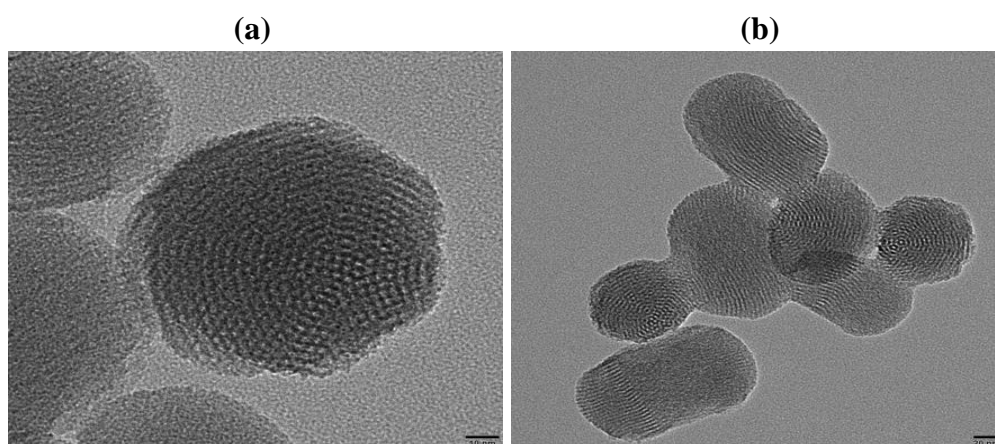


Figure 4.5: The morphology and elemental analysis of the silica nanoparticles, showing (a), (b) the FE-SEM micrographs of MCM-B nanoparticles. The presence of nitrogen and boron in the EDS spectrum in (c) confirms the possible functionalization of the silica nanoparticles with amino and phenylboronic acid, respectively and (d), (e) the FE-SEM micrographs of the MCM -B-D nanoparticles.

High resolution transmission emission microscopy (TEM) images are presented in Figure 4.6. These reveal spherical nanoparticles. When these images were analyzed with Image J, the average particle sizes of the nanomaterials synthesized (MCM-B and MCM-B-D) were found to be  $72.36 \pm 9.06$  nm and  $81.97 \pm 9.01$  nm, respectively. The pores in the TEM images of MCM-B were more visible than that of MCM-B-D. This is attributed to the effects of dextran as a gating agent on the nanoparticle pores. Hence, the level of nanoparticle agglomeration in Figure 4.5e is more pronounced in MCM-B-D than in MCM-B.



**Figure 4.6.** High-resolution transmission electron micrographs of (a) MCM-B nanoparticles before capping with dextran and (b) MCM-B-D nanoparticles (after capping the MCM-B nanoparticles with dextran).

The zeta potential values at pH 5.0, 6.5 and 7.4 showed that the MCM-41 nanoparticles had a negative surface charge, as shown in Table 4.1. This could be due to the ionization of silanol groups in aqueous solution. The surface has an acidic character, due to the possibility of proton displacement ( $-\text{Si}-\text{O}- + \text{H}^+$ ) [61]. Upon silanizing the silica nanoparticles with amine group (MCM-N), the surface charge increased to positive values, which decreased with further functionalization with phenylboronic acid groups (MCM-B) and capping with dextran (MCM-B-D).

Table 4.1: A summary of the zeta potentials of the silica nanoparticles.

pH	MCM-41 (mV)	MCM-N (mV)	MCM-B (mV)	MCM-B-D (mV)
<b>5.00</b>	-14.73	+40.03	+34.5	+9.05
<b>6.50</b>	-30.77	+29.27	+11.4	+7.87
<b>7.40</b>	-34.33	+14.53	+12.57	+2.59

#### **4.7.2. Drug release from the nanoparticle formulations**

Prior to the drug release studies, the amount of drug effectively loaded into the nanoparticles and the encapsulation efficiencies were determined, and the results are summarized in Table 4.1. The amount of drugs loaded into the nanoparticles and the encapsulation efficiency was generally higher for the free doxorubicin than the AMACR-doxorubicin conjugates.

The drug release profile of doxorubicin (DOX) and doxorubicin conjugated with AMACR (DOX-A) was examined from the bare mesoporous silica nanoparticles (MCM-41), the functionalized nanoparticles with the phenylboronic acid groups (MCM-B), and the nanoparticles capped with dextran (MCM-B-D). The drug release studies were carried out using two different buffers of pH 6.5 and pH 7.4 at three different temperatures of 37°C (representing physiological temperature [62]), 41°C and 44°C (representing hyperthermia temperature region [62]). The following drug-loaded formulations were used: MCM-41-DOX, MCM-41-DOX-A, MCM-B-DOX, MCM-B-DOX-A, MCM-B-D-DOX and MCM-B-D-DOX-A. In general, the drug release profiles show that the highest DOX and DOX-A cumulative release were obtained at pH 6.5 for all the nanoparticle formulations, which is aimed at mimicking the tumor microenvironment [35], [36], as shown in Figures 4.7 (a-c) and (g-i).

Cumulative drug release was lower at pH 7.4, which represents the human physiological pH value [35]–[37]. This lower drug release was observed in both MCM-B and MCM-B-D but the release profile of the latter was lower than that of the former, as shown in Figure 4.7 (a-f) for the

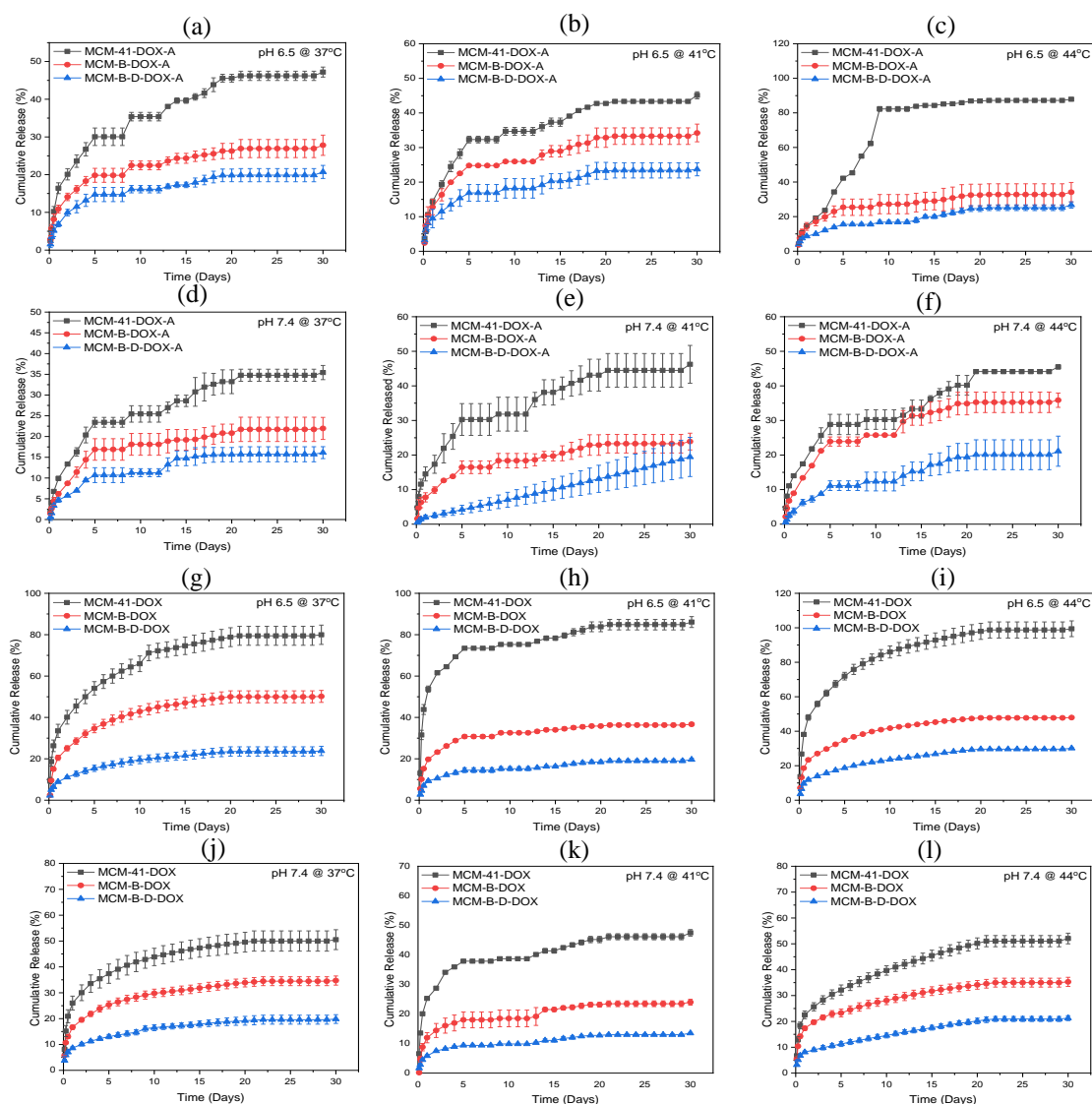


Figure 4.7: Cumulative AMACR-conjugated drug release from MCM-41-DOX-A, MCM-B-DOX-A and MCM-B-D-DOX-A of DOX-A nanoparticles in a buffer of pH 6.5 at (a) 37°C (b) 41°C (c) 44°C, and in a buffer of pH 7.4 at (d) 37°C (e) 41°C (f) 44°C. Furthermore, the cumulative drug release from MCM-41-DOX, MCM-B-DOX and MCM-B-D-DOX of DOX nanoparticles in a buffer of pH 6.5 at (g) 37°C (h) 41°C (i) 44°C, in a buffer at pH 7.4 at (j) 37°C (k) 41°C (l) 44°C.

conjugated drug (DOX-A) and Figure 4.7 (g-l) for the free drug (DOX), meaning that capping the nanoparticle with a polymer can slow down the release of DOX and DOX-A in silica-based nanoparticle drug formulations over a period of time. In this study, the release was sustained for a period of thirty days. Hence, the reduction in the cumulative release is attributed to the capping of the pores by dextran, as well as the increase in the acidity of the

buffer. The release profile also tends to increase beyond 50%, with MCM-41 having the highest cumulative release and MCM-B-D having the least cumulative release, as shown in Figure 4.7 for the conjugated drug and the free drug-loaded nanoparticles. The release studies also showed that the highest cumulative drug release was obtained at 44°C, while at 37°C the lowest drug release was obtained, as shown in Figure 4.7 (a, d, g and j).

Five kinetic models (Zeroth order model, First order model, Second order model, Higuchi model, and Korsmeyer–Peppas model) were used to characterize *in vitro* drug release kinetics from the silica-based nanoparticle drug formulations [63]. Table 4.2 shows the correlation coefficients  $R^2$  obtained for the release kinetics. The release kinetics for the various silica-based nanoparticle formulations with the highest  $R^2$  correlation coefficients value fits the Korsmeyer-Peppas model, as shown in Table 4.2. The release exponents for the free drug-loaded formulations MCM-41-DOX and MCM-B-DOX range from  $0.43 \leq n \leq 0.71$  which corresponds to anomalous transport [39], [64], while MCM-B-D-DOX exhibited anomalous transport at 37 °C, quasi-Fickian diffusion at 41 °C and a Fickian diffusion at 44 °C. The conjugated drug-loaded formulations, on the other hand, predominantly exhibited quasi-Fickian diffusion [64]. This conclusion was drawn based on the standard created from drug release from a spherical drug formulation by Peppas and Sahlin [64].

Table 4.2: The correlation coefficients ( $R^2$ ), the drug release exponents (n), and the diffusion coefficients (D) from the various drug-loaded silica nanoparticle formulations determined from the drug release kinetic models.

Formulations		Temperature (°C)	Zeroth Order	First Order	Second Order	Higuchi	Korsmeyer- Peppas	
			$R^2$	$R^2$	$R^2$	$R^2$	$R^2$	n
<b>Unconjugated Drug</b>	MCM-41-DOX	37	0.71	0.91	0.98	0.90	0.84	0.61
		41	0.58	0.86	0.93	0.76	0.93	0.55
		44	0.65	0.89	0.95	0.87	0.88	0.62
	MCM-B-DOX	37	0.65	0.92	0.92	0.88	0.96	0.71
		41	0.77	0.96	0.90	0.92	0.94	0.57
		44	0.65	0.94	0.88	0.86	0.93	0.64
	MCM-B-D-DOX	37	0.68	0.88	0.87	0.88	0.91	0.45
		41	0.61	0.84	0.64	0.8	0.94	0.35
		44	0.63	0.86	0.80	0.87	0.88	0.43
<b>Conjugated Drug</b>	MCM-41-DOX-A	37	0.61	0.66	0.60	0.75	0.86	0.26
		41	0.61	0.61	0.54	0.70	0.91	0.26
		44	0.79	0.71	0.59	0.74	0.85	0.49
	MCM-B-DOX-A	37	0.72	0.74	0.61	0.75	0.83	0.35
		41	0.72	0.77	0.72	0.62	0.87	0.34
		44	0.81	0.68	0.51	0.71	0.86	0.36
	MCM-B-D-DOX-A	37	0.80	0.51	0.45	0.75	0.69	0.30
		41	0.67	0.58	0.34	0.62	0.88	0.28
		44	0.23	0.26	0.26	0.72	0.81	0.21

The thermodynamic parameters computed from *in vitro* drug release data are presented in Table 4.3. The change in Gibbs free energy  $\Delta G$  value for MCM-41, MCM-B and MCM-B-D were all positive, indicating the nonspontaneous nature of the release of drugs from the nanoparticles. This nonspontaneous process could be ascribed to interactions of the loaded drugs with the nanoparticles MCM-41, MCM-B and MCM-B-D, which most likely aided the sustained drug release over a period of thirty days [15], [37]. The change in the enthalpy ( $\Delta E_a$ ) was found to have a positive value, indicating that drug release from the aforementioned nanoparticles was by an endothermic process [14], [65]. There was also a reduction in system disorder when the drug dispersed in the medium tried to attain

equilibrium, the very small negative readings of the entropy change ( $\Delta S$ ) for all the nanoparticle formulations clearly confirmed this. The activation energy ( $E_a$ ) indicates the amount of energy needed to transfer

the drug molecule from the silica-based drug formulation to the media (e.g. PBS or PC-3 cells). Hence, the positive value of the activation energy indicated that the *in vitro* drug release was mostly due to processes relating to anomalous transport mechanisms, super case II or quasi Fickian diffusion.

Table 4.3: Thermodynamic parameters of MCM-41, MCM-B, and MCM-B-D nanoparticles

Formulations	Temperature (°C/K)	$E_a$ (kJ mol <sup>-1</sup> )	$\Delta H$ (kJ mol <sup>-1</sup> )	$\Delta S$ (kJ mol <sup>-1</sup> K <sup>-1</sup> )	$\Delta G$ (kJ mol <sup>-1</sup> )
<b>MCM-41-DOX</b>	37/310.15	10.973	13.58	-0.3869	133.58
	41/314.15				135.13
	44/317.15				136.29
<b>MCM-B-DOX</b>	37/310.15	7.107	9.714	-0.3774	126.76
	41/314.15				128.27
	44/317.15				129.40

loaded with doxorubicin (DOX) and doxorubicin conjugated with AMACR (DOX-A).

<b>MCM-B-D-DOX</b>	37/310.15	37.534	14.548	-0.4063	140.55
	41/314.15				142.18
	44/317.15				143.40
<b>MCM-41-DOX-A</b>	37/310.15	6.488	3.882	-0.352	113.13
	41/314.15				114.53
	44/317.15				115.59
<b>MCM-B-DOX-A</b>	37/310.15	21.403	18.79	-0.307	114.10
	41/314.15				115.33
	44/317.15				116.25
<b>MCM-B-D-DOX-A</b>	37/310.15	20.086	17.479	-0.311	114.08
	41/314.15				115.32
	44/317.15				116.26

#### 4.7.3. Simulation of drug release

In this work, drug elution was simulated from five porous geometries (Figure 4.8). The following assumptions were made in the simulations:

- (i) First, it was assumed that the porous structure was 2D and formed from the agglomeration of millions of nanoparticles with the mesopore interconnected to form the bulk material.
- (ii) Secondly, the fluid was assumed to be flowing from one boundary of the 2D rectangular geometry to the other end while keeping the third and fourth boundaries as insulating boundaries. After designing the 2D geometry, the fluid in each case was assumed to be flowing from the concentration boundary to the flux boundary, which are always perpendicular to each other. The two other boundaries were assumed to be insulating.
- (iii) The five geometries in Figure 4.8 were used in time-dependent studies that were used to simulate drug elution over periods between 10 days and 30 days. The five geometries were designed with different orientations to control the directions of flow.

For each of the geometries in Figure 4.8, the simulation was run for a period of 720 h (30 days). Steady state conditions were reached at different times, for the different geometries in Figure 4.8. In the case of Figure 4.8a, steady state was reached between  $t = 0$  h to  $t = 240$  h.

The average flux from the 2D model can be obtained by solving the average flux equation below

$$N_{\text{average}} = \frac{1}{L_0} \int_0^{L_0} k_m (c - c_1) dS \quad 4.21$$

where  $L_0$  corresponds to the length over the flux boundary. At steady state, the average flux can be obtained from equation 4.21. The effective diffusion was also obtained from.

$$D^{\text{eff}} \frac{(c_0 - c_{\text{out}})}{L_1} = N_{\text{average}} \quad 4.22$$

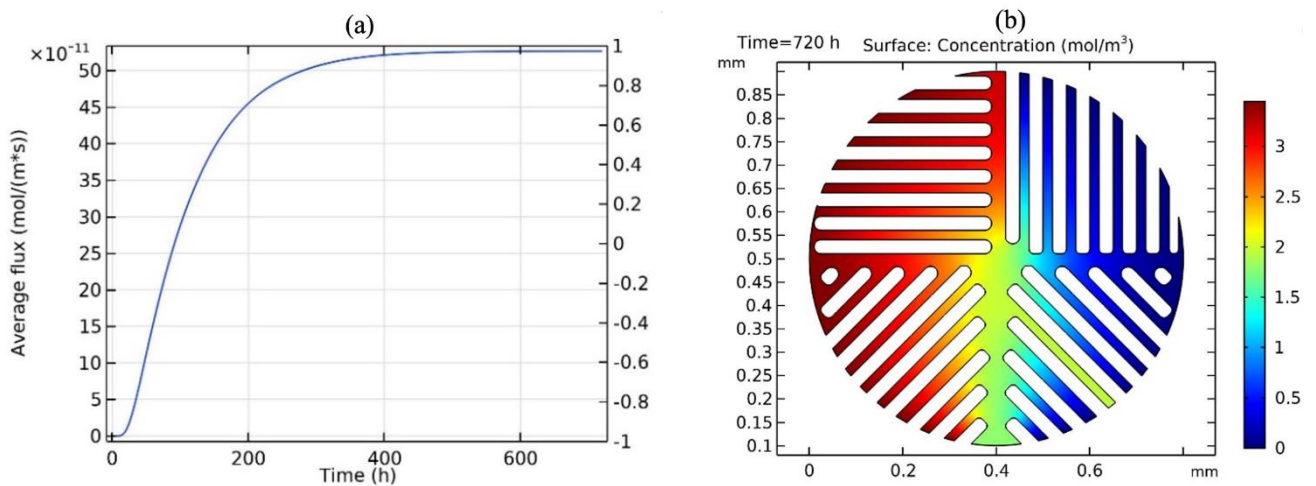
where  $L_1$  is the length of the 2D geometries that were created along the x-axis, and it is the average concentration at the flux border. Integrating according to the expression below yields the average concentration:

$$c_{\text{out}} = \frac{1}{L_0} \int_0^{L_0} c dy \quad 4.23$$

The relationship between the free diffusion coefficient and the effective diffusion coefficient is given by:

$$D^{\text{eff}} = D \frac{\varepsilon}{\tau} \quad 4.24$$

where  $\tau$  represents the tortuosity in length per unit length of diffusion through a porous medium, and the porosity of the particle is represented as  $\varepsilon$ . At the end of the simulation, a relationship was established between the 1D homogenized model and the drug release profile



as shown in figure 4.8.

Figure 4.8: (a) Average flux of the drugs through the multiple pores of the nanomaterial over a 30-day period and (b) Time-dependent transport of diluted species from the concentration boundary to the left down to the flux boundary to the right.

#### 4.8. Viability of prostate cancer cells

In order to use the AMACR-conjugated drug-loaded nanoparticles to specifically target the prostate cancer cells, it was necessary to demonstrate the expression of AMACR receptors on these cells. The confocal fluorescence images in Figure 4.9 show that AMACR receptors (green color) are expressed on the surfaces of the PC-3 prostate cancer cell line. Upon binding anti-AMACR primary antibody to the AMACR receptors on fixed PC-3 cells and labelling them with Alexa Fluor 488-conjugated secondary antibody, the green fluorescence of the Alexa Fluor 488 dye was seen at areas with AMACR receptors under a confocal fluorescence microscope.

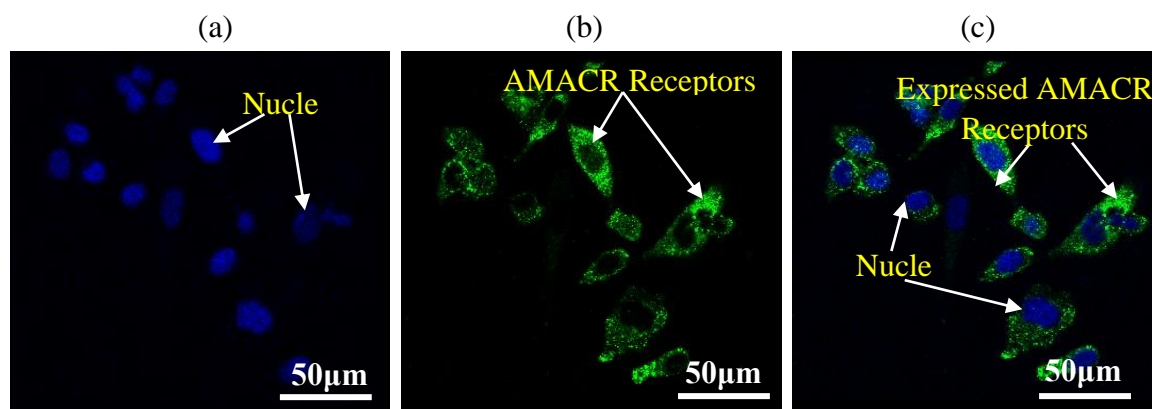


Figure 4.9: Confocal fluorescence images showing the expression AMACR receptors (green stains) from human prostate cancer cells (PC-3), showing (a) the blue staining of the nuclei of PC-3 cells (b) the green staining of the expressed AMACR receptors on the surfaces of the PC-3 cells and (c) the composite image.

Cell metabolic activity, as measured by the percentage alamar blue reduction, was used as an indirect measure of cell viability. Thus, a higher percentage alamar blue reduction value

corresponded to greater cell viability. The percentage alamar blue reduction by the PC-3 prostate cancer cells treated with the unloaded drugs (DOX and DOX-A) and the different bare and drug (DOX and DOX-A) loaded nanoparticles was quantified at times 0, 6, 24, 48, 72, and 96h after treatment, and the results are shown in Figure 4.10. Treating the PC-3 cells with the various formulations significantly reduced ( $p < 0.05$ ) the PC-3 cell viability after 96 h. Also, cells exposed to the bare nanoparticles generally exhibited higher cell viabilities than those treated with the drug-loaded nanoparticles, suggesting that the drugs released from the latter exerted anti-proliferative effects on the PC-3 cancer cells.

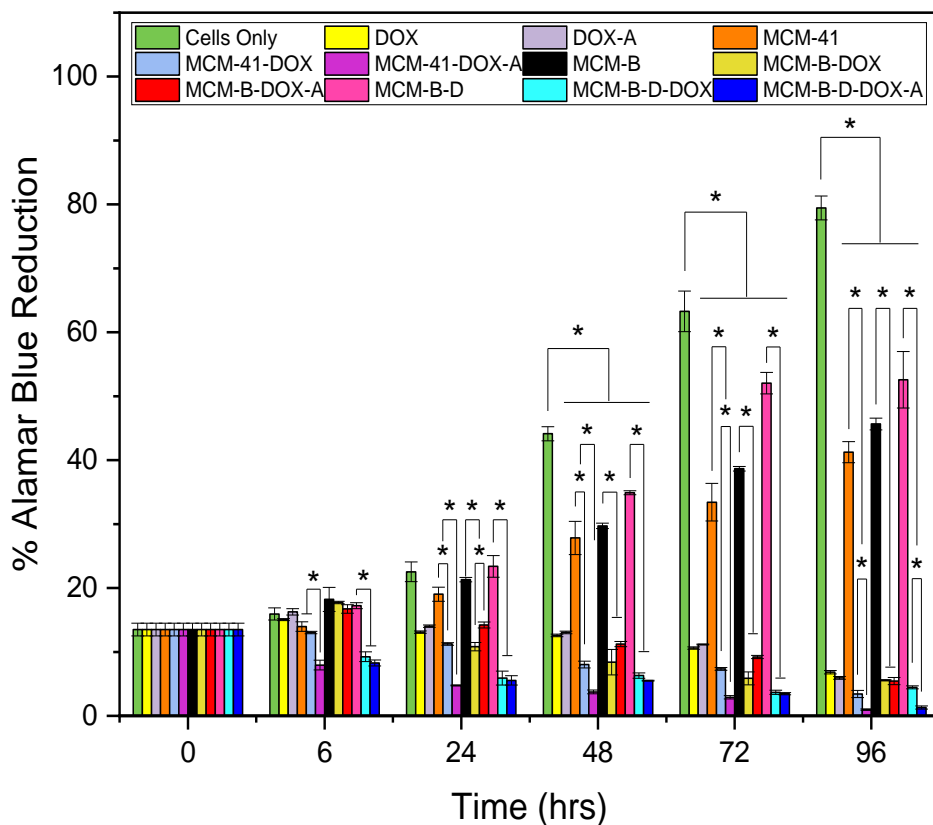


Figure 4.10: The effects of the different drug-loaded nanoparticle formulations on the viability of prostate cancer cells treated with them, as measured by the percentage alamar

blue reduction. The error bars represent the standard deviations for  $n = 3$  independent trials. \*  $p < 0.05$ .

After 96 h of treatment, the DOX-loaded nanoparticles (MCM-41-DOX) reduced ( $p < 0.05$ ) the PC-3 cell viability than the bare nanoparticles (MCM-41). When exposed to the DOX-A-loaded nanoparticles (MCM-41-DOX-A) the PC-3 cell viability further declined ( $p < 0.05$ ). The PC-3 viability under treatment with MCM-B-D nanoparticles displayed a similar trend as the MCM-41 nanoparticles above (i.e.  $\text{MCM-B-D-DOX-A} < \text{MCM-B-D-DOX} < \text{MCM-B-D}$ ). Both the DOX-A-loaded MCM-41 (MCM-41-DOX-A) and MCM-B-D (MCM-B-D-DOX-A) nanoparticles gave rise to the lowest PC-3 cell viability after 96 h, and there was no significant difference in cell viability between these two groups at 96 h ( $p > 0.05$ ). On the other hand, there was no significant difference between the cell viabilities associated with the DOX and DOX-A-loaded MCM-B nanoparticles (MCM-B-DOX vs. MCM-B-DOX-A) ( $p > 0.05$ ), although these were significantly lower than ( $p < 0.05$ ) the bare MCM-B nanoparticles. Finally, after 96 h of treatment, no significant differences ( $p > 0.05$ ) were observed between the viabilities of PC-3 cells exposed to the unloaded drugs directly added (DOX and DOX-A), on one hand, and the MCM-41-DOX, MCM-B-DOX, MCM-B-DOX-A, and MCM-B-D-DOX drug-loaded nanoparticles, on the other. However, the viability of the cells treated with MCM-DOX-A and MCM-B-D-DOX-A drug-loaded nanoparticles were lower than ( $p < 0.05$ ) those treated with DOX and DOX-A alone.

#### **4.9. Discussion**

The main goal of this study was to design a silica nanoparticle-based drug delivery system for the sustained release of model targeted and free cancer drugs (AMACR-conjugated and free doxorubicin, respectively) to inhibit the growth of prostate cancer cells. We hypothesized that functionalizing mesoporous silica nanoparticles with phenylboronic acid groups to reduce

their pore sizes would slow down the release of targeted or free doxorubicin drugs loaded into their pores. We also hypothesized that capping the drug-loaded phenylboronic acid - functionalized silica nanoparticles with a polymer (dextran) would slow down the targeted or free doxorubicin drug release even further.

To test these hypotheses, MCM-41 silica nanoparticles were synthesized. These were then functionalized with phenylboronic acid groups (MCM-B) that were tethered to amino groups previously grafted onto the MCM-41 nanoparticles. FTIR analysis (Figure 4.2) confirmed the formation of silica through the peaks for Si-O-Si symmetric stretching, Si-OH stretching, and Si-O-Si asymmetric vibrations observed at 798, 960, and 1079  $\text{cm}^{-1}$ , respectively. After grafting amino groups onto the MCM-41 silica nanoparticles to form MCM-N, distinct FTIR bands for amino groups were observed, which disappeared when the amino groups were tethered to phenylboronic acid groups to form MCM-B. An amide bond was expected to be formed between the amino groups of MCM-N and the display of peaks for C=O and C-N stretching at  $\sim 1654 \text{ cm}^{-1}$  and  $\sim 1627 \text{ cm}^{-1}$  confirmed the formation of MCM-B nanoparticles [37][38].

The FE-SEM micrographs (Figure 4.5) showed that the silica nanoparticles were spherical in shape. However, the MCM-B-D nanoparticles were agglomerated due to the gelling effects of the dextran used to cap the nanoparticles. The spherical shapes were more evident when the nanoparticles were visualized at higher magnifications under high resolution TEM (Figure 4.6). The TEM micrograph also revealed the pores on the silica nanoparticles. Using Image J to analyze the TEM images, the average diameter of the MCM-B nanoparticles was measured to be  $72.36 \pm 9.06 \text{ nm}$ , which increased to  $81.97 \pm 9.01 \text{ nm}$  upon capping with dextran.

Nitrogen sorption analysis indicated that the MCM-41 silica nanoparticles were mesoporous, but the pore volume and the pore diameter decreased, as expected, upon functionalizing the MCM-41 nanoparticles with phenylboronic acid groups to form MCM-B nanoparticles.

Therefore, doxorubicin was loaded into the pores of the MCM-41 and MCM-B nanoparticles as a model prostate cancer drug.

AMACR receptors have been reported to be overexpressed on the surfaces of prostate cancer cells [66]. To this end, we stained for AMACR receptors on the PC-3 prostate cancer cell lines using immunofluorescence, and the confocal fluorescence images captured (Figure 4.9) indicated that AMACR receptors were expressed on the prostate cancer cells. Therefore, we conjugated AMACR ligands to doxorubicin (DOX-A) that could bind to these expressed AMACR receptors to specifically target the prostate cancer cells for killing by the attached DOX drug. On this basis, the DOX-A drug was also loaded into the pores of the silica-based nanoparticles (MCM-41 and MCM-B).

There is a need to slow down the release of doxorubicin-based drugs in smaller doses due to their high toxicity so as to reduce their side effects on healthy tissues. Thus, we capped the drug-loaded MCM-B nanoparticles with dextran to form MCM-B-D drug-loaded nanoparticles. FTIR analysis (Figure 4.2a) confirmed the existence of dextran characteristic peaks at  $\sim 3453\text{ cm}^{-1}$ ,  $\sim 942\text{ cm}^{-1}$ , and  $\sim 800\text{ cm}^{-1}$  [47], [48], in addition to the silica and phenylboronic acid peaks observed earlier, suggesting that dextran was successfully capped around the MCM-B nanoparticles.

TGA analysis (Figure 4.2b) showed that there were successive weight losses after functionalizing the MCM-41 nanoparticles with phenylboronic acid groups and capping them with dextran. These excess weight losses were attributed to the decomposition of the additional groups (amino and phenylboronic acid groups and dextran), thus, indicating the successful grafting of phenylboronic acid groups and dextran to the silica nanoparticles. These observations were corroborated by the XRD patterns in Figure 4.4, which display characteristic peaks for MCM-41 silica nanoparticles that gradually disappeared with functionalization (MCM-B) and dextran capping (MCM-B-D).

We also determined the surface charges of the nanoparticles through zeta potential measurements at pH values corresponding to physiological conditions (pH 7.4) and the tumor microenvironment (pH 5.0 and 6.5). The negative surface charges of the MCM-41 nanoparticles were attributed to their negatively charged silanol groups [55]. silanized to introduce amino groups to its structure,, the MCM-N nanoparticles exhibited positive surface charges consistent with the protonation of the  $-NH_2$  (amino) group, which confirmed the grafting of the amino groups to the MCM-41 nanoparticles. Tethering the phenylboronic acid groups to the amino groups decreased the positive surface charges of the MCM-B nanoparticles due to the negatively charged carboxyl groups of the phenylboronic acid, providing evidence for the successful grafting of phenylboronic acid groups to the MCM-41 nanoparticles. Further evidence was obtained from the EDS elemental analysis of the MCM-B nanoparticles (Figure 4.5c), which revealed the presence of silica and oxygen (from the MCM-41 nanoparticles), nitrogen (from the grafted amino groups), and boron (from the phenylboronic acid groups tethered to the MCM-41 nanoparticles).

After successfully synthesizing and characterizing the silica-based nanoparticles and loading them with the model drugs (DOX and DOX-A), the next part of this study was to test the hypothesis that reducing the pore sizes of the mesoporous silica nanoparticles (MCM-41) through functionalization with phenylboronic acid groups (MCM-B) and capping the pores with dextran (MCM-B-D) would slow down and prolong the release of the model drugs (DOX and DOX-A) from the nanoparticles. The drug release studies were carried out in phosphate-buffered saline (PBS) at pH 7.4 and pH 6.5, corresponding to the physiological and slightly acidic tumor microenvironments, respectively, and at physiological (37 °C) and hyperthermic temperatures (41°C and 44 °C).

It is evident from the drug release profiles (Figure 4.7) that there was a higher cumulative release of drugs (DOX and DOX-A) from the nanoparticles at pH 6.5 than at pH 7.4. This

was probably the result of the protonation of DOX and DOX-A in the acidic environment (pH 6.5) that weakened the electrostatic interactions between the drugs (DOX and DOX-A) and the silica nanoparticles [19], thus, releasing more drugs into the buffer. It is, therefore, expected that these drug-loaded silica nanoparticles would elute the drugs (DOX and DOX-A) to the prostate tumor region when they are administered since the tumor microenvironment is acidic [59]–[61].

As shown in Figure 4.7, the cumulative drug release was generally higher for the drug-loaded MCM-41 nanoparticles. However, functionalizing the MCM-41 with the phenylboronic acid groups (MCM-B) reduced the BJH pore volume and pore diameter by ~ 49% and ~ 24%, respectively. The lower cumulative release from the MCM-B nanoparticles is, therefore, attributed to the significant reduction in the pore sizes that slowed down the release of the loaded drugs (DOX and DOX-A). Drug release was further slowed down when the drug-loaded MCM-B nanoparticles were capped with dextran (MCM-B-D). This was consistent with the reduction in the BJH pore size distribution observed in Figure 4.3b for the MCM-B-D nanoparticles. The slow down in drug release was also attributed to the nonspontaneous nature of the release as determined from the thermodynamic parameters.

It must be pointed out that the weight of the DOX-A molecules was expected to increase by ~54 kDa (the molecular weight of the AMACR peptide), which will also increase the molecule size. As a result, the amount of DOX-A that can be loaded into the nanoparticle pores will decrease compared to the free DOX that has a smaller molecular weight and size. In addition, the larger molecular weight and size will slow down the release of DOX-A drugs from the pores. This contributed to the lower amounts of DOX-A loaded into the nanoparticles (Table S1) and the lower cumulative drug release profiles observed for the DOX-A formulations (Figure 4.7) than the free DOX formulations.

In this study, it was observed that the percentage cumulative drug released (Figures 4.7a-l) occurred in two phases for the DOX-loaded nanoparticles (Figures 4.7a-f), with the first phase being moderate all through to day 20, while the remaining 10 days showed that the drug release profile was linear. In the case of DOX-A-loaded nanoparticles (Figure 4.7g-l), it exhibited three phases. The first phase exhibited a very fast cumulative drug release within the first five days study, for the next fifteen days the release was considerably reduced. Hence the moderate slope of the curve. The last 10 days looks considerably consistent up till day 30 with the slope being almost linear. Hence the first phase drug release is as a result of drug burst release [67], while the second and the last phases of DOX-A release could be as a result of steady state drug release [68].

As a result of the initial exposure of the nanoparticles to the phosphate-buffered saline, burst release occurs. This is followed by the next phase in which a power-law relationship is observed between the cumulative amount of drug released and time [69]. The presence of dextran as a gating agent could also be the cause of the sustained DOX and DOX-A release. Thus, the presence of dextran appears to provide physical barriers to drug transport across the nanoparticles, while limiting diffusion and erosion processes [70], [71].

Next, we fitted the drug release data to the kinetic models to understand the kinetics of *in vitro* drug (DOX and DOX-A) release from the silica-based nanoparticle drug delivery systems developed. The kinetic model that fitted the release data with the highest  $R^2$  value was selected as the best model. Based on this criterion, the release of DOX and DOX-A drugs from the silica-based nanoparticles followed the Korsmeyer-Peppas kinetic model [69]–[71] (Table 4.2). The initial 60% of drug release is usually best fit by this power law model [72], [43]. This model yields  $n$  values in the range  $0.21 < n < 0.71$ . The release exponent,  $n$ , of the Korsmeyer-Peppas model was then used to assign the mechanism of drug release from the different silica-based drug formulations. Anomalous transport (non-Fickian diffusion) was

the mechanism driving the release of DOX from MCM-41 and MCM-B nanoparticles, while the release of DOX from MCM-B-D nanoparticles was driven by anomalous transport (non-Fickian diffusion) at 37°C, quasi-Fickian diffusion at 41°C, and Fickian diffusion at 44 °C. The release mechanism of the DOX-A drug from all the silica-based nanoparticles (MCM-41, MCM-B, and MCM-B-D) were predominantly driven by quasi-Fickian diffusion.

It is important to note that the release profile of MCM-B-D-DOX-A in Figure 4.7e appears different from its counterparts in Figures 4.7 d and f. As noted above, the MCM-B-D-DOX-A release profile in Figure 4.7e fitted a Korsmeyer-Peppas kinetic model with a quasi-Fickian drug release mechanism (release exponent,  $n = 0.28$  (Table 4.2)). This means that DOX-A was partially diffusing into the surrounding medium through the swollen dextran capping the nanoparticles, thereby slowing down the amount of drug released. Although the release profile appears linear throughout, it is nonlinear for the first 2 days of release. This was likely the result of the initial release of the DOX-A drugs trapped in the dextran as it swelled. By the second day and over time, the fully swollen dextran continuously trapped the drugs diffusing out of the pores of the underlying nanoparticles and subsequently released them into the surrounding medium via quasi-diffusion at a relatively constant rate until day 30, accounting for the relatively linear profile observed between days 2 and 30. In addition, although not within the scope of this work, it is most likely that if the drug release duration is extended beyond 30 days, the release profile will eventually plateau when the dextran is degrading or has degraded and the drugs can directly diffuse out from the nanoparticle pores into the surrounding medium.

The diffusion coefficients obtained for the conjugated drug (DOX-A) formulations were higher than those obtained for the unconjugated drug (DOX) formulations. The diffusion coefficient ( $D$ ) was in the range of  $1.84 \times 10^{-23} \leq D \leq 4.17 \times 10^{-23} m^2 s^{-1}$  for the unconjugated drug (DOX) and  $1.21 \times 10^{-22} \leq D \leq 4.26 \times 10^{-22} m^2 s^{-1}$  for the conjugated

drug (DOX-A). This shows that the conjugated drug diffuses faster into the medium than the unconjugated drug.

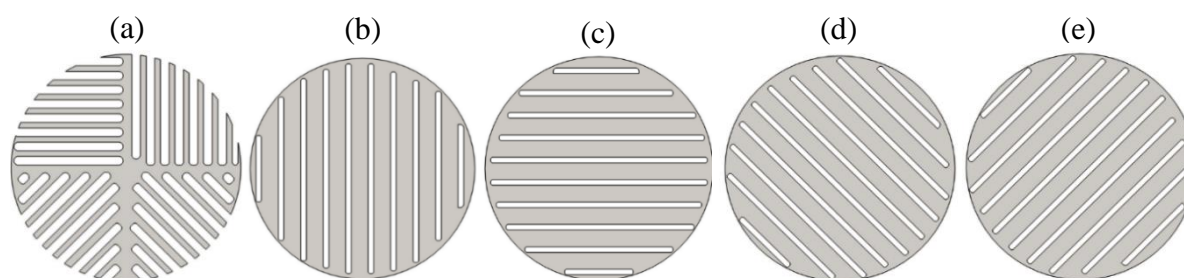


Figure 4.11: Porous geometries used for the simulation: (a) multi-porous (b) horizontal pore alignment (c) vertical pore alignment (d) and (e) are both inclined at 45° to the horizontal.

The COMSOL simulation shows the average flux of the drug through the multiple pores as in figure 4.11 of the nanomaterial over a month and the time-dependent transport of diluted species from the concentration boundary showing that a line plot can be expressed as a 1D homogenized model which is synonymous to the cumulative drug release profile. This shows that the assumption that the bare and the functionalized silica nanoparticle are having pores in different direction is a good assertion as the cumulative flux after 30 days converges to a plot shown in Figure 4.8 that is synonymous with the cumulative drug release in Figure 4.7.

The release of drugs (DOX and DOX-A) from the drug-loaded nanoparticle formulations were correlated with reductions in the viability of PC-3 prostate cancer cells, hence the cell growth inhibition, to investigate whether the sustained release of DOX and DOX-A was beneficial for killing and inhibiting prostate cancer cell growth. A decrease in cell growth is expected to cause a reduction in cell viability. Therefore, lower percentage alamar blue reduction values corresponded to greater cell growth inhibition. On that basis, it was evident from Figure 4.10 that the drugs (DOX and DOX-A) released from the drug-loaded nanoparticles exerted significant antiproliferative effects on the PC-3 cells to cause the observed lower cell viabilities than the drug-free nanoparticles. Whereas the drug-free nanoparticles lowered cell viability by a factor of about 1.5, the drug-loaded nanoparticles

reduced cell viability approx. 10-fold compared to the drug-free nanoparticles and approx. 16-fold versus the untreated cells, suggesting that the drugs released from the nanoparticles were more responsible for killing the cancer cells than the nanoparticles themselves.

The slow release of DOX and DOX-A drugs observed from the MCM-B and the dextran-capped MCM-B nanoparticles (Figure 4.7) did not correspond to lower cell viabilities of the MCM-41 nanoparticles. This suggests that the slowdown in drug release from the MCM-B nanoparticles owing to their smaller pore sizes did not translate into greater cell growth inhibition *in vitro*. Therefore, longer *in vitro* cell viability studies beyond 96 h as well as *in vivo* studies are needed to explore the effects of the prolonged drug release.

However, the slow release of AMACR-conjugated drugs (DOX-A) from the nanoparticles was generally the most potent in inhibiting PC-3 cell growth. We showed in this study through immunofluorescence staining (Figure 4.9) that AMACR receptors were expressed on the surfaces of the PC-3 prostate cancer cells. Therefore, the greater cell growth inhibition associated with the sustained release of the AMACR-conjugated drugs (DOX-A) from the nanoparticles was attributed to the binding of the AMACR attached to the DOX drug to the AMACR receptors on the PC-3 cancer cells. This had the tendency of increasing the uptake of the drugs (DOX) by the cells through receptor-mediated endocytosis, leading to increased cell death.

It is worth noting that, although lower doses of drugs (DOX and DOX-A) were released from the drug-loaded nanoparticle formulations, the released drugs inhibited the growth of the PC-3 prostate cancer cells at similar levels as the directly added/unloaded drugs (DOX and DOX-A). Furthermore, the sustained release of low doses of AMACR-conjugated DOX (DOX-A) from the silica-based drug delivery systems inhibited the PC-3 cancer cell growth more than the higher dose unloaded drugs (DOX and DOX-A). This suggests that by loading DOX and DOX-A into silica-based nanoparticles, the slowed release of the drugs can inhibit the growth

of prostate cancer cells *in vitro* at the same level or even better than adding the drugs (DOX and DOX-A) directly to the cells.

Before closing, it is interesting to note that the three bare nanoparticles; MCM-41, MCM-B and MCM-B-D supported the growth of the PC-3 cells to some extent, as shown in Figure 4.10. This work demonstrates that DOX and AMACR-conjugated DOX can be loaded into silica-based nanoparticles with varying pore sizes to slow down and prolong drug release over a 30-day period. It also shows that AMACR-conjugated drug-loaded formulations were more effective in inhibiting the growth of the PC-3 prostate cancer cells because of the specificity that was enabled by the conjugation of the DOX drug with AMACR. The drugs are released in lower doses from the nanoparticles than the drugs that are directly treated to cells but inhibit the growth of prostate cancer cells at similar levels or even better. This is beneficial for reducing the amount of highly toxic cancer drugs, such as doxorubicin, in the patient and could potentially shrink/eliminate prostate tumors *in vivo* while reducing side effects. Further work is needed to demonstrate these effects under *in vivo* conditions.

#### **4.10. Conclusions**

This paper presents the results of a combined experimental and theoretical/computational study of the targeted delivery of untargeted (DOX) and targeted (DOX-A) cancer drugs from silica nanoparticles to prostate cancer cells. Salient conclusions arising from the study are summarized below.

1. Silica nanoparticle structures can be engineered to have controlled pore sizes, volumes and surface areas. The cumulative drug release from these structures also increases with increasing temperature, for temperatures between 37°C and 44°C.

2. Drug release from the conjugated drug (DOX-A)-loaded nanoparticle formulations occurs predominantly by quasi-Fickian diffusion, while that of the unconjugated drug (DOX) formulation occurs predominantly by anomalous transport diffusion.
3. The specific targeting of the prostate cancer cells is enhanced by the conjugation of doxorubicin to AMACR and loading them into the silica nanoparticles. The sustained release of AMACR-conjugated doxorubicin enhances the specific targeting of prostate cancer cells for killing by the attached doxorubicin, through the binding of the AMACR moiety to the overexpressed AMACR receptors on the cells, thereby lowering prostate cancer cell viability.
4. Estimated drug release profiles similar to the experimental results through a silica nanoparticle drug formulation can be obtained through simulations following set diffusion principles and valid assumptions based on the TEM particle size. This has been validated by the convergence of the 30-day simulation plot and the 1D homogenized plot.

#### 4.11 Bibliography

- [1] H. Sung *et al.*, “Global Cancer Statistics 2020: GLOBOCAN Estimates of Incidence and Mortality Worldwide for 36 Cancers in 185 Countries,” *CA. Cancer J. Clin.*, vol. 71, no. 3, pp. 209–249, 2021, doi: 10.3322/caac.21660.
- [2] M. Nguyen-Nielsen and M. Borre, “Diagnostic and Therapeutic Strategies for Prostate Cancer,” *Semin. Nucl. Med.*, vol. 46, no. 6, pp. 484–490, Nov. 2016, doi: 10.1053/J.SEMNUCLMED.2016.07.002.
- [3] N. Bock *et al.*, “In vitro engineering of a bone metastases model allows for study of the effects of antiandrogen therapies in advanced prostate cancer,” *Sci. Adv.*, vol. 7, no. 27, pp. 1–4, 2021, doi: 10.1126/sciadv.abg2564.
- [4] J. Pinto, A. Athanassiou, and D. Fragouli, “Surface modification of polymeric foams for oil spills remediation,” *J. Environ. Manage.*, vol. 206, pp. 872–889, 2018, doi: 10.1016/j.jenvman.2017.11.060.
- [5] U. Lindner *et al.*, “Focal Laser Ablation for Prostate Cancer Followed by Radical Prostatectomy: Validation of Focal Therapy and Imaging Accuracy,” *Eur. Urol.*, vol. 57, no. 6, pp. 1111–1114, Jun. 2010, doi: 10.1016/J.EURURO.2010.03.008.
- [6] M. Vallet-Regi, A. Rámila, R. P. Del Real, and J. Pérez-Pariente, “A new property of MCM-41: Drug delivery system,” *Chem. Mater.*, vol. 13, no. 2, pp. 308–311, 2001, doi: 10.1021/cm0011559.
- [7] M. Perera, N. Krishnananthan, U. Lindner, and N. Lawrentschuk, “An update on focal therapy for prostate cancer,” *Nat. Rev. Urol.*, vol. 13, no. 11, pp. 641–653, 2016, doi: 10.1038/nrurol.2016.177.

- [8] A. J. Evans, "Treatment effects in prostate cancer," *Mod. Pathol.* 2018 311, vol. 31, no. 1, pp. 110–121, Jan. 2018, doi: 10.1038/modpathol.2017.158.
- [9] C. R. Cardwell, J. M. O'Sullivan, S. Jain, B. M. Hicks, P. A. Devine, and Ú. C. McMenamin, "Hormone therapy use and the risk of acute kidney injury in patients with prostate cancer: a population-based cohort study," *Prostate Cancer Prostatic Dis.*, 2021, doi: 10.1038/s41391-021-00348-x.
- [10] A. B. Barqawi *et al.*, "Boosting immune response with GM-CSF optimizes primary cryotherapy outcomes in the treatment of prostate cancer: a prospective randomized clinical trial," *Prostate Cancer Prostatic Dis.*, 2021, doi: 10.1038/s41391-021-00321-8.
- [11] G. Gravis *et al.*, "Chemotherapy in hormone-sensitive metastatic prostate cancer: Evidences and uncertainties from the literature," *Cancer Treat. Rev.*, vol. 55, pp. 211–217, 2017, doi: 10.1016/j.ctrv.2016.09.008.
- [12] J. W. Nichols and Y. H. Bae, "Odyssey of a cancer nanoparticle: From injection site to site of action," *Nano Today*, vol. 7, no. 6, pp. 606–618, 2012, doi: 10.1016/j.nantod.2012.10.010.
- [13] J. D. Obayemi *et al.*, "Degradable porous drug-loaded polymer scaffolds for localized cancer drug delivery and breast cell/tissue growth," *Mater. Sci. Eng. C*, vol. 112, no. March, p. 110794, 2020, doi: 10.1016/j.msec.2020.110794.
- [14] S. M. Jusu *et al.*, "Drug-encapsulated blend of PLGA-PEG microspheres: in vitro and in vivo study of the effects of localized/targeted drug delivery on the treatment of triple-negative breast cancer," *Scientific Reports*, vol. 10, no. 1. 2020, doi: 10.1038/s41598-020-71129-0.
- [15] J. D. Obayemi *et al.*, "LHRH-Conjugated Drugs as Targeted Therapeutic Agent for the Specific Targeting and Localized Treatment of Triple Negative Breast Cancer." Nature Research (Scientific Report), Worcester, p. 18, 2020, doi: /doi.org/10.1038/s41598-020-64979-1www.nature.com/scientificreportsLHRH-conjugated Drugs as targeted therapeutic Agents for the Specific Targeting and Localized Treatment of Triple Negative Breast cancerJ. D. obayemi1,2, A. A. Salifu1, S. C. Eluu3, V. O. Uzonwanne1, S. M. Jusu4, C. C. Nwazojie4, c. e. onyekanne4, O. Ojelabi5, L. payne6, C. M. Moore6, J. A. King6,7 & W. o. Soboyejo1,2 ✉Bulk chemotherapy and drug release strategies for cancer treatment have been associated with lack of specificity.
- [16] T. K. Upadhyay *et al.*, "Nanoparticles mediated target-specific drug delivery in prostate cancer: In-depth review," *Curr. Med. Chem.*, vol. 29, Dec. 2021, doi: 10.2174/0929867329666211221112312.
- [17] M. Mladenović *et al.*, "Ph-responsive release of ruthenium metalloterapeutics from mesoporous silica-based nanocarriers," *Pharmaceutics*, vol. 13, no. 4. 2021, doi: 10.3390/pharmaceutics13040460.
- [18] C. M. Day, M. J. Sweetman, Y. Song, S. E. Plush, and S. Garg, "Functionalized mesoporous silica nanoparticles as delivery systems for doxorubicin: Drug loading and release," *Applied Sciences (Switzerland)*, vol. 11, no. 13. 2021, doi: 10.3390/app11136121.
- [19] Y. Zhang *et al.*, "Tumor microenvironment responsive mesoporous silica nanoparticles for dual delivery of doxorubicin and chemodynamic therapy (CDT) agent," *New J. Chem.*, vol. 44, no. 6, pp. 2578–2586, 2020, doi: 10.1039/c9nj05427h.
- [20] C. P. Silveira, L. M. Apolinário, W. J. Fávaro, A. J. Paula, and N. Durán, "Doxorubicin-Functionalized Silica Nanoparticles Incorporated into a Thermoreversible Hydrogel and Intraperitoneally Administered Result in High Prostate Antitumor Activity and Reduced Cardiotoxicity of Doxorubicin," *ACS Biomater. Sci. Eng.*, vol. 2, no. 7, pp. 1190–1199, Jul. 2016, doi:

- 10.1021/ACSBBIOMATERIALS.6B00241/SUPPL\_FILE/AB6B00241\_SI\_001.PDF.
- [21] T. A. N. Dau *et al.*, “Surface Functionalization of Doxorubicin loaded MCM-41 Mesoporous Silica Nanoparticles by 3-Aminopropyltriethoxysilane for Selective Anticancer 9 Effect on A549 and A549/DOX Cells,” *J. Electron. Mater.*, vol. 50, no. 5, pp. 2932–2939, 2021, doi: 10.1007/s11664-021-08813-y.
- [22] N. Jiang, S. Zhu, J. Chen, Y. Niu, and L. Zhou, “A-Methylacyl-CoA Racemase (AMACR) and Prostate-Cancer Risk: A Meta-Analysis of 4,385 Participants,” *PLoS One*, vol. 8, no. 10, p. e74386, Oct. 2013, doi: 10.1371/JOURNAL.PONE.0074386.
- [23] F. Ping, B. Chunyin, C. Bin, L. Na, and W. Jifeng, “Screening of differentially expressed genes and identification of AMACR as a prognostic marker in prostate cancer,” *Andrologia*, p. 15, 2021, doi: 10.1111/and.14067.
- [24] I. H. Erdogdu, B. Tuna, K. Yorukoglu, and R. Montironi, “Biomarkers in Urinary Tract and Male Genital System Carcinomas,” in *Biomarkers in Carcinoma of Unknown Primary*, Springer Nature, 2022, p. 37.
- [25] H. Yamada *et al.*, “Alpha methylacyl-CoA racemase (AMACR) in prostate adenocarcinomas from Japanese patients: Is AMACR a ‘race’-dependent marker?,” *Prostate*, vol. 73, no. 1, pp. 54–59, Jan. 2013, doi: 10.1002/PROS.22539.
- [26] A. Sayari, “Catalysis by crystalline mesoporous molecular sieves,” *Chem. Mater.*, vol. 8, no. 8, pp. 1840–1852, 1996, doi: 10.1021/cm950585+.
- [27] B. V. V. S. Pavan Kumar, K. Salikolimi, and M. Eswaramoorthy, “Glucose-and pH-Responsive Charge-Reversal Surfaces,” 2014, doi: 10.1021/la500407r.
- [28] S.-W. Sun, Y.-C. Lin, Y.-M. Weng, and M.-J. Chen, “Efficiency improvements on ninhydrin method for amino acid quantification,” *J. Food Compos. Anal.*, vol. 19, pp. 112–117, 2006, doi: 10.1016/j.jfca.2005.04.006.
- [29] J. E. Ippolito *et al.*, “Extracellular pH Modulates Neuroendocrine Prostate Cancer Cell Metabolism and Susceptibility to the Mitochondrial Inhibitor Niclosamide,” *POS ONE*, vol. 11, no. 7, p. 26, 2016, doi: <https://doi.org/10.1371/journal.pone.0159675>.
- [30] T. Aina *et al.*, “Release kinetics of fungicidal antimicrobials into packaged foods,” *J. Food Saf.*, no. February, p. 12, 2021, doi: 10.1111/jfs.12904.
- [31] S. M. Jusu *et al.*, “Plga-cs-peg microparticles for controlled drug delivery in the treatment of triple negative breast cancer cells,” *Applied Sciences (Switzerland)*, vol. 11, no. 15, 2021, doi: 10.3390/app11157112.
- [32] “Mathematical models of drug release,” in *Strategies to Modify the Drug Release from Pharmaceutical Systems*, 2015, pp. 63–86.
- [33] A. D. Nurhan, “Dash, Murthy,” *Polish Pharm. Soc.*, vol. 67, no. 3, pp. 217–223, 2010.
- [34] R. Gouda, H. Baishya, and Z. Qing, “Application of Mathematical Models in Drug Release Kinetics of Carbidopa and Levodopa ER Tablets,” *J. Dev. Drugs*, vol. 06, no. 02, pp. 1–8, 2017, doi: 10.4172/2329-6631.1000171.
- [35] E. S. Akinboye, M. D. Rosen, S. R. Denmeade, B. Kwabi-Addo, and O. Bakare, “Design, Synthesis, and Evaluation of pH-Dependent hydrolyzable Emetine Analogues as Treatment for Prostate Cancer,” *J. Med. Chem.*, vol. 55, p. 10, 2012, doi: [doi.org/10.1021/jm300426q](https://doi.org/10.1021/jm300426q).
- [36] E. A. S., M. D. Rosen, S. R. Denmeade, B. Kwabi-Addo, and O. Bakare, “Design, Synthesis, and Evaluation of pH-Dependent Hydrolyzable Emetine Analogues as Treatment for Prostate Cancer.” American Chemical Society, p. 10, 2021, doi: [dx.doi.org/10.1021/jm300426q](https://dx.doi.org/10.1021/jm300426q).
- [37] S. M. Jusu *et al.*, “Plga-cs-peg microparticles for controlled drug delivery in the treatment of triple negative breast cancer cells,” *Applied Sciences (Switzerland)*, vol. 11, no. 15, 2021, doi: 10.3390/app11157112.
- [38] D. Wójcik-Pastuszka, J. Krzak, B. Macikowski, R. Berkowski, B. Osiński, and W.

- Musiał, "Evaluation of the release kinetics of a pharmacologically active substance from model intra-articular implants replacing the cruciate ligaments of the knee," *Materials (Basel)*, vol. 12, no. 8, 2019, doi: 10.3390/ma12081202.
- [39] R. W. Korsmeyer, R. Gurny, E. Doelker, P. Buri, and N. A. Peppas, "Mechanisms of solute release from porous hydrophilic polymers," *Int. J. Pharm.*, vol. 15, no. 1, pp. 25–35, 1983, doi: 10.1016/0378-5173(83)90064-9.
- [40] A. Lamprecht, H. Yamamoto, H. Takeuchi, and Y. Kawashima, "Microsphere design for the colonic delivery of 5-fluorouracil," *J. Control. Release*, vol. 90, no. 3, pp. 313–322, 2003, doi: 10.1016/S0168-3659(03)00195-0.
- [41] K. Onwudiwe *et al.*, "Investigation of creep properties and the cytoskeletal structures of non-tumorigenic breast cells and triple-negative breast cancer cells," *J. Biomed. Mater. Res. Part A*, Dec. 2021, doi: 10.1002/JBM.A.37348.
- [42] P. J. Marsac, H. Konno, and L. S. Taylor, "A comparison of the physical stability of amorphous felodipine and nifedipine systems," *Pharm. Res.*, vol. 23, no. 10, pp. 2306–2316, 2006, doi: 10.1007/s11095-006-9047-9.
- [43] J. M. Smith, "Introduction to chemical engineering thermodynamics," *Journal of Chemical Education*, vol. 27, no. 10, p. 584, 1950, doi: 10.1021/ed027p584.3.
- [44] X. Du *et al.*, "CO<sub>2</sub> and CH<sub>4</sub> adsorption on different rank coals: A thermodynamics study of surface potential, Gibbs free energy change and entropy loss," *Fuel*, vol. 283, no. January 2020, p. 118886, 2021, doi: 10.1016/j.fuel.2020.118886.
- [45] R. A. De Souza and R. J. Chater, "Oxygen exchange and diffusion measurements: The importance of extracting the correct initial and boundary conditions," *Solid State Ionics*, vol. 176, no. 23–24, pp. 1915–1920, 2005, doi: 10.1016/j.ssi.2005.05.010.
- [46] A. Xu, T. S. Zhao, L. Shi, and J. B. Xu, "Lattice Boltzmann Simulation of Mass Transfer Coefficients for Chemically Reactive Flows in Porous Media," *J. Heat Transfer*, vol. 140, no. 5, pp. 1–8, 2018, doi: 10.1115/1.4038555.
- [47] T. Sugimoto, S. Hamamoto, and T. Nishimura, "Inhibited nanobubble transport in a saturated porous medium: Effects of deposited colloidal particles," *J. Contam. Hydrol.*, p. 103854, 2021, doi: 10.1016/j.jconhyd.2021.103854.
- [48] S. S. Shafqat *et al.*, "Development of amino-functionalized silica nanoparticles for efficient and rapid removal of COD from pre-treated palm oil effluent," *J. Mater. Res. Technol.*, vol. 8, no. 1, pp. 385–395, 2019, doi: 10.1016/j.jmrt.2018.03.002.
- [49] V. Hernández-Morales, R. Nava, Y. J. Acosta-Silva, S. A. Macías-Sánchez, J. J. Pérez-Bueno, and B. Pawelec, "Adsorption of lead (II) on SBA-15 mesoporous molecular sieve functionalized with -NH<sub>2</sub> groups," *Microporous Mesoporous Mater.*, vol. 160, pp. 133–142, 2012, doi: 10.1016/j.micromeso.2012.05.004.
- [50] A. L. Brody, E. R. Strupinsky, and L. R. Kline, *Active packaging for food application*. New York,: Tehnomic Publishing, 2001.
- [51] X. Xue, H. Gong, H. Zheng, and L. Ye, "Boronic Acid Functionalized Nanosilica for Binding Guest Molecules," *ACS Appl. Nano Mater.*, vol. 4, no. 3, pp. 2866–2875, Mar. 2021, doi: 10.1021/ACSANM.1C00005/SUPPL\_FILE/AN1C00005\_SI\_001.PDF.
- [52] L. Quiles-Carrillo, S. Montava-Jordà, T. Boronat, C. Sammon, R. Balart, and S. Torres-Giner, "On the use of gallic acid as a potential natural antioxidant and ultraviolet light stabilizer in cast-extruded bio-based high-density polyethylene films," *Polymers*, vol. 12, no. 1, 2020, doi: 10.3390/polym12010031.
- [53] K. Panwar, M. Jassal, and A. K. Agrawal, "In situ synthesis of Ag-SiO<sub>2</sub> Janus particles with epoxy functionality for textile applications," *Particuology*, vol. 19, pp. 107–112, Apr. 2015, doi: 10.1016/J.PARTIC.2014.06.007.
- [54] G. Yang *et al.*, "Synthesis and characterization of dextran-capped silver nanoparticles with enhanced antibacterial activity," *J. Nanosci. Nanotechnol.*, vol. 12, no. 5, pp.

- 3766–3774, 2012, doi: 10.1166/jnn.2012.5865.
- [55] G. Predoi *et al.*, “Preparation and Characterization of Dextran Coated Iron Oxide Nanoparticles Thin Layers,” *Polymers (Basel)*, vol. 13, no. 14, p. 2351, Jul. 2021, doi: 10.3390/POLYM13142351.
- [56] I. Denry, J. M. Nédélec, and J. A. Holloway, “Tranexamic acid-loaded hemostatic nanoclay microsphere frameworks,” *Journal of Biomedical Materials Research - Part B Applied Biomaterials*. Wiley, p. 9, 2021, doi: 10.1002/jbm.b.34918.
- [57] I. Union, O. F. Pure, and A. Chemistry, “Recommendations for the characterization of porous solids (Technical Report),” *Pure Appl. Chem.*, vol. 66, no. 8, pp. 1739–1758, 1994, doi: 10.1351/pac199466081739.
- [58] S. Lim *et al.*, “Synthesis and Characterization of Highly Ordered Co–MCM-41 for Production of Aligned Single Walled Carbon Nanotubes (SWNT),” *J. Phys. Chem. B*, vol. 107, no. 40, pp. 11048–11056, Oct. 2003, doi: 10.1021/JP0304778.
- [59] T. M. Albayati, I. K. Salih, and H. F. Alazzawi, “Synthesis and characterization of a modified surface of SBA-15 mesoporous silica for a chloramphenicol drug delivery system,” *Heliyon*, vol. 5, no. 10, p. e02539, 2019, doi: 10.1016/j.heliyon.2019.e02539.
- [60] N. Loy and L. Preziosi, *Mathematical Biology Kinetic models with non-local sensing determining cell polarization and speed according to independent cues*. Italy: Springer Berlin Heidelberg, 2019.
- [61] K. Czarnobaj, M. Prokopowicz, and K. Greber, “Use of materials based on polymeric silica as bone-targeted drug delivery systems for metronidazole,” *International Journal of Molecular Sciences*, vol. 20, no. 6. 2019, doi: 10.3390/ijms20061311.
- [62] G. B. Dell’isola, E. Cosentini, L. Canale, G. Ficco, and M. Dell’isola, “Noncontact body temperature measurement: Uncertainty evaluation and screening decision rule to prevent the spread of covid-19,” *Sensors (Switzerland)*, vol. 21, no. 2. pp. 1–20, 2021, doi: 10.3390/s21020346.
- [63] S. Dash, P. N. Murthy, L. Nath, and P. Chowdhury, “Kinetic modeling on drug release from controlled drug delivery systems,” *Acta Pol. Pharm. - Drug Res.*, vol. 67, no. 3, pp. 217–223, 2010.
- [64] N. A. Peppas and J. J. Sahlin, “A simple equation for the description of solute release. III. Coupling of diffusion and relaxation,” *Int. J. Pharm.*, vol. 57, no. 2, pp. 169–172, Dec. 1989, doi: 10.1016/0378-5173(89)90306-2.
- [65] Y. Danyuo *et al.*, “Swelling of poly(N-isopropylacrylamide) P(NIPA)-based hydrogels with bacterial-synthesized prodigiosin for localized cancer drug delivery,” *Mater. Sci. Eng. C*, vol. 59, pp. 19–29, 2016, doi: 10.1016/j.msec.2015.09.090.
- [66] H. Lee *et al.*, “Alpha-Methylacyl-CoA Racemase (AMACR), a Potential New Biomarker for Glioblastoma,” *Frontiers in Oncology*, vol. 10. 2020, doi: 10.3389/fonc.2020.550673.
- [67] S. Bhattacharyya, H. Wang, and P. Ducheyne, “Polymer-coated mesoporous silica nanoparticles for the controlled release of macromolecules,” *Acta Biomater.*, vol. 8, no. 9, pp. 3429–3435, Sep. 2012, doi: 10.1016/J.ACTBIO.2012.06.003.
- [68] M. Kumar Jha, M. Habibur Rahman, and M. Mofizur Rahman, “BIPHASIC ORAL SOLID DRUG DELIVERY SYSTEM: A REVIEW,” *IJPSR*, vol. 2, no. 5, 2011.
- [69] M. Bouchoucha, M. F. Côté, R. C-Gaudreault, M. A. Fortin, and F. Kleitz, “Size-Controlled Functionalized Mesoporous Silica Nanoparticles for Tunable Drug Release and Enhanced Anti-Tumoral Activity,” *Chem. Mater.*, vol. 28, no. 12, pp. 4243–4258, Jun. 2016, doi: 10.1021/ACS.CHEMMATER.6B00877/SUPPL\_FILE/CM6B00877\_SI\_001.PDF.
- [70] M. G. Devi, S. Dutta, A. T. Al Hinai, and S. Feroz, “Studies on encapsulation of Rifampicin and its release from chitosan-dextran sulfate capsules,” *Korean J. Chem.*

- Eng. 2014 321*, vol. 32, no. 1, pp. 118–124, Aug. 2014, doi: 10.1007/S11814-014-0161-9.
- [71] A. Angelopoulou, E. K. Efthimiadou, and G. Kordas, “Dextran modified pH sensitive silica hydro-xerogels as promising drug delivery scaffolds,” *Mater. Lett.*, vol. 74, pp. 50–53, May 2012, doi: 10.1016/J.MATLET.2012.01.054.
- [72] J. D. Obayemi *et al.*, *PLGA-based microparticles loaded with bacterial-synthesized prodigiosin for anticancer drug release: Effects of particle size on drug release kinetics and cell viability*, vol. 66. 2016.

## CHAPTER FIVE

### 5.0 AMACR-Conjugated Drug as Targeted Therapeutic Agents for the Specific Targeting and Localized Treatment of Prostate Cancer Cells (PC-3)

#### 5.1 Introduction

Prostate cancer (PC) is the most commonly diagnosed cancer among men in 112 nations [1] and the second leading cause of deaths in men in 48 countries [1]. Cancers that form in the gland cells that line the prostate gland are known as adenocarcinomas [2][3]. Prostatic adenocarcinomas which accounts for 93 percent of prostate cancer cases [4], is the most frequent such as PC3, LNCap [5] and DU145 a prostate xenograft model cell line [2].

Furthermore, PC-3 cells have hallmarks of a weakly differentiated adenocarcinoma, according to electron microscopy [2], PC3 cells also have a strong proclivity for spreading.

Studies has shown that prostate adenocarcinoma is the most common kind of prostate cancer PC stem cells with high phenotypic and functional variability, and the progeny can exhibit a wide range of plasticity [6][7]. From literatures, some of the immunohistochemical markers that are expressed on the prostatic adenocarcinoma are prostate specific antigen (PSA), prostatic acid phosphatase (PAP) [8], alpha-methyl acyl-CoA racemase (AMACR) [9], androgen receptor (AR) [10], and cytokeratin 7 [11], which can be targeted to aid PC treatment [4]. Hence to aid better treatment of prostate cancer (PC), combining the existing treatment options by targeting PC surface biomarkers while ensuring a balance in treatment efficacy with toxicity can result in better treatment [12]. Bulk chemotherapy and radiation treatment, for example, are some of the PC treatment methods that has been adopted but these options lack specificity and are linked with significant adverse effects [13].

According to recent research, prostate cancer cells can develop or acquire inherent resistance to chemotherapy treatments [14]. This drug resistance is frequently linked to a complex tumor microenvironment [15]. Also when bulk chemotherapy is used, only a small proportion of the drug eventually reach the tumor locations of interest [16], [17]. As a result, there are negative consequences. This causes pharmacological interactions with non-tumor-bearing healthy tissue and organs, resulting in adverse effects. Most targeted cancer drug delivery systems may connect selectively to antibodies, peptides, and hormone receptors created to treat cancers that overexpress these receptors [13]. Some examples of biomarkers that are overexpressed on the surface of PC are androgen receptors [18], estrogen receptors (ER $\alpha$  and ER $\beta$ ) [19], nuclear receptors [20], alpha-methylacyl-CoA racemase (AMACR) and transmembrane serine protease 2 (TMPRSS2) [21]. Prostate cancer treatment poses difficulties since it is not adequately targeted by standard cancer treatments. As a result, chemotherapeutic drugs for the effective targeting and treatment of prostate cancer are needed.

In a work carried out on about 40 PC specimen it was discovered that over 30 out of the specimens have AMACR overexpressed on them [22].

Tumor-specific markers were used in a given research by *Dykman L. A.*, using laboratory and morphological differential diagnosis of prostate cancer [23]. Alpha-methylacyl-CoA racemase (AMACR) is one of the most promising tumor markers, with studies showing a link between AMACR expression, tumor differentiation, and tumor progression [23]. The most frequent method for detecting AMACR is immunohistochemistry [23]. Furthermore, colloidal gold nanoparticles' adjuvant characteristics was used to make rabbit polyclonal anti-AMACR antibodies and compared them to commercially available monoclonal anti-AMACR antibodies [23]. ELISA revealed that the sensitivity of both antibody types was similar and close to  $1 \mu\text{g mL}^{-1}$ , however a gold nanoshell-aided immunodot assay revealed that polyclonal gold-derived anti-AMACR antibodies had an eight-fold greater sensitivity [23]. We solely target Prostate adenocarcinoma cells that have been found to overexpress AMACR receptors in this research. AMACR regulates the metabolism of lipids and medicines in all metabolic pathways. AMACR induces chiral reversal of 2-methyl acids by regulating  $\beta$ -oxidation of branched chain lipids in peroxisomes and mitochondria [24]. In another work, *Brice A. P. et al.* Used stably produced short-hairpin RNA constructs, to establish that suppressing AMACR expression can inhibits the development of prostate cancer cell lines. This finding clearly implies that the AMACR enzyme might be a therapeutic target in prostate cancer [25]. Despite the fact that much research has been done into the overexpression of AMACR receptors in a variety of cancers such as prostate cancer, liver cancer, papillary renal cell carcinoma (pRCC), [24]. Only prostate cancer cells that have been demonstrated to overexpress AMACR receptors are studied in this study [24], [26].

AMACR has been found as a novel diagnostic marker for PC, and to better understand the dysregulation of AMACR that occurs during prostate carcinogenesis and to start evaluating a

putative functional role for this protein in this process investigation of the enzymatic activity of AMACR in both clinical PC samples and tissue culture cells were studied to know if AMACR is required for PC cell line growth [27]. Hence lowering AMACR protein levels in PC cells causes the cancerous cell to proliferate less, and this impact appears to be independent of androgen action. The therapeutic potential of down-regulating AMACR in conjunction with androgen ablation was subsequently tested *in vitro*, and it was discovered that it had an additional antiproliferative impact which suggest that additional research into AMACR as a potential new therapeutic target in PC is necessary [27].

In this paper, AMACR-conjugated doxorubicin was studied as a model cancer drug. The synthesis was done by conjugating cysteine AMACR to doxorubicin hydrochloride. The conjugated structure was characterised using Fourier Transform Infra-Red spectroscopy (FTIR) and UV-Vis. The effect of the AMACR-conjugated drug was elucidated on cancer cells and tissues *in-vitro* using PC-3 PC cell line under *in vivo* condition athymic nude mouse model was induced with PC xenograft tumors. The ability of the conjugated drug to target and shrink PC xenograft tumors for about two weeks in the prostate cancer tumour progression was studied. Hence, the results' shows the implications for selective targeting and localized therapy of PC are then highlighted.

## **5.2 Materials and Methods**

### **5.2.1 Materials**

Alpha methyl Acyl-CoA racemase (AMACR) was procured from Bio SB, Santa Barbara, CA, USA. doxorubicin hydrochloride salt was supplied by LC Laboratories, Woburn, MA, USA. (N-hydroxysuccinimide (NHS), 1-ethyl-3-(3-dimethylaminopropyl) carbodiimide hydrochloride (EDC HCl), Alamar Blue Assay (ABA) kits, Dubecco Phosphate Buffer (DPBS), 24-well plate, and opaque 96-well plates were purchased from Thermo Fisher Scientific (Waltham, MA, USA). N.N-Dimethylformamide (DMF) and Dimethyl sulfoxide

(DMSO) were purchased from Sigma-Aldrich Co. LLC, (St. Louis, MO USA). 3 kDa Amicon Ultra-4 Centrifugal Filters Units and Amicon Pro Purification System were purchased from Millipore Sigma (Burlington, MA, USA). The growth media F-12K, Fetal bovine serum (FBS), Human prostate cancer cells (PC-3 cell line, ATCC-CRL-1435) was obtained from American Type Culture Collection (ATCC), Manassas, VA, USA.

## **5.2.2 Methods**

### **5.2.2.1 Conjugation of doxorubicin with AMACR peptide**

The conjugation was carried out by weighing 1.0 mg of DOX and mixing it with 0.5 ml of dimethyl sulfoxide (DMSO) and 88.2  $\mu$ l of EDC for 40 minutes in the dark with vigorous stirring. Following that, 105.9  $\mu$ l of NHS was added to the reaction mixture and stirred for 20 minutes. 15  $\mu$ l AMACR was mixed with 1.2 ml of a 0.1 M NaP04/0.15 M NaCl solution at a pH of 7.4 to make an AMACR solution. In the dark, the AMACR solution was mixed into the reaction mix. Then, for the final 5 hours of the conjugation process, 0.4ml of DMSO:Water (7.5:2.5) was gradually added to the reaction in ice with gentle stirring. A combination of 3 kDa Amicon Ultra-4 Centrifugal Filters Units and the Amicon Pro Purification System was used to remove excess AMACR from the conjugated DOX solution. The conjugation of AMACR to DOX was then confirmed with FTIR and NMR as reported by (Aina T. *et al.* 2022).

### **5.2.2.2 FTIR Investigation**

Attenuated Total Reflectance Fourier Transform Infrared Spectroscopy (ATR-FTIR) (IRSpirit, Shimadzu, Kyoto, Japan) was used to investigate the bare drug DOX and the conjugated drug DOX-A. To explore the functional groups, bonding types, and chemical features of the new

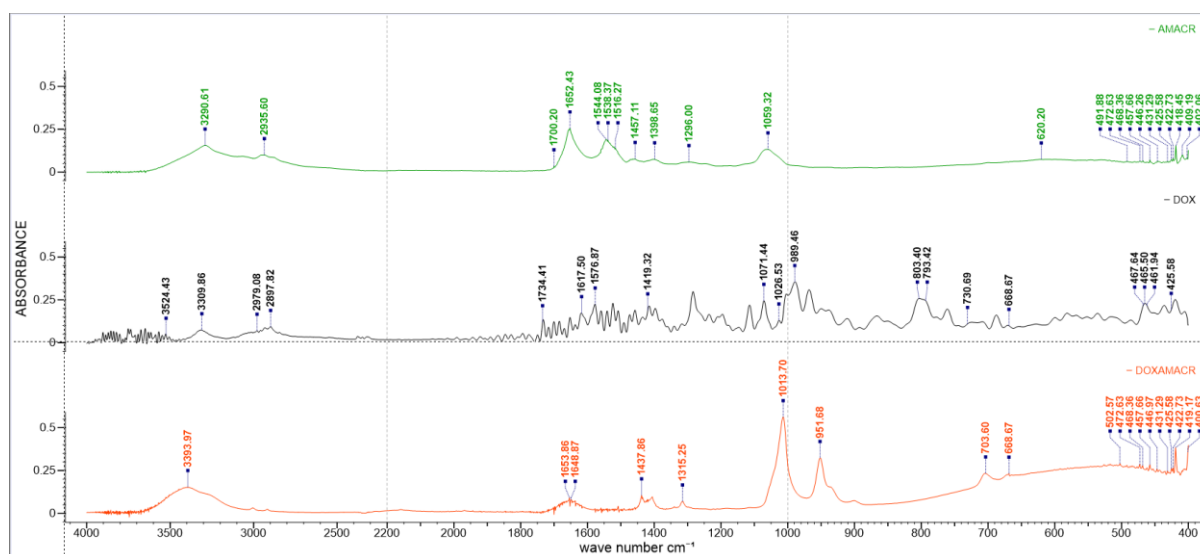


Figure 5.1: FTIR spectra of AMACR, DOX and DOX-A drug

compounds, the FTIR was set to absorbance mode with the spectra as shown above figure 5.1.

### 5.2.2.3 UV-Vis

Samples of DOX, DOX-A and AMACR dissolved in DPBS to form a solution. 700µl of each of the formulations were poured in the cuvette for UV-Vis measurement to determine the wavelength at which all the drug formulations (DOX, DOX-A and AMACR) would produce a conspicuous peak. DOX, DOX-A and AMACR peaks occur at 481.5nm, 490nm and 276.5nm respectively. After, conjugation the peaks for DOX-A shifts to the right that is from 481.5nm to a broad peak of 490nm and the initial peak of 276.5nm becomes evident at 253.5nm indicating the likelihood of conjugation between AMACR and DOX as in figure 5.2.

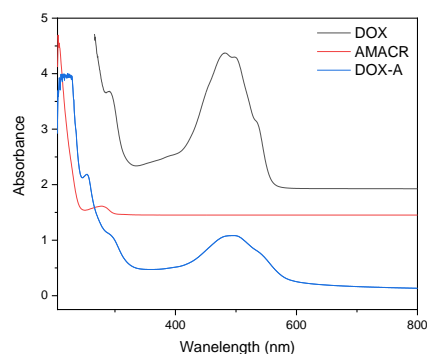


Figure 5.2: UV-VIS spectra of DOX, DOX-A and AMACR dissolved in PBS pH7.4

#### 5.2.2.4 Cell culture

American Type Culture Collection (ATCC), Manassas, VA, USA, provided us with the PC-3 and PNT-2 cell line ATCC-CRL-1435 and the PNT-2 cell line. The PC-3 cells were grown in F-12K media supplemented with 10% fetal bovine serum whereas the PNT-2 cells (from normal prostate tissue) were grown in RPMI base medium (consisting of 10% FBS, 2mM glutamine with or without pen strip). Cultures were maintained at 37°C in a CO<sub>2</sub> incubator with a humidified environment of 95% air and 5% CO<sub>2</sub>.

#### 5.2.2.5 *In vitro* cell viability

The *in vitro* survivability of prostate cancer cells with and without treatment with DOX and DOX-A drugs was assessed using the alamar blue test to quantify cell metabolic activities, represented as the percentage alamar blue decrease [28], [29]. The decrease in a greater proportion of the alamar blue suggests that the cells are developing more quickly and are thus more viable (figure 5.3). Human prostate cancer cells (PC-3 cell line, ATCC-CRL-1435) were obtained from the American Type Culture Collection (ATCC), Manassas, VA, USA, and cultured in a complete culture medium made up of Kaighn's modification of Ham's medium (F-12K) supplemented with 10% fetal bovine serum (FBS) and 1% penicillin/streptomycin. At 37° and 5% CO<sub>2</sub>, the cells were kept in a humidified incubator.

Using a 0.25 percent trypsin-EDTA solution, cells were collected at 70-80% confluence and sub-cultured in new T75 flasks. Approximately  $10^4$  cells/well were seeded in 24-well plates ( $n = 3$ ) at passages 5-7 and incubated overnight at 37 °C and 5% CO<sub>2</sub>. Following that, each well's culture media was treated with 15 μM and 30 μM of free DOX and DOX-A. After treating the cells, the culture media was changed with culture medium #containing 10% alamar blue reagent at predefined time intervals (0, 6, 24, 48, 72, and 96 hours). 100 ml aliquots were put into black opaque 96-well plates for fluorescence intensity measurements after 3 hours of incubation at 37 °C and 5% CO<sub>2</sub>. Using a 1420 Victor3 multilabel plate reader (excitation/emission: 544/590 nm) (Perkin Elmer, Waltham, MA, USA). The equations below were used to compute the percentage alamar blue reduction and the percentage cell growth inhibition.

$$\% \text{ Alamar Blue Reduction} = \frac{FI_{\text{sample}} - FI_{10\%AB}}{FI_{100\%R} - FI_{10\%AB}} \times 100, \quad 5.1$$

$$\% \text{ Cell Growth Inhibition} = 1 - \frac{FI_{\text{samples}}}{FI_{\text{cells}}} \times 100 \quad 5.2$$

Where  $FI_{\text{sample}}$  is the sample's fluorescence intensity,  $FI_{10\%AB}$  is 10% Alamar blue reagent fluorescence intensity,  $FI_{100\%R}$  is 100% reduced Alamar blue fluorescence intensity, and  $FI_{\text{cells}}$  is the fluorescence intensity of untreated cells [28].

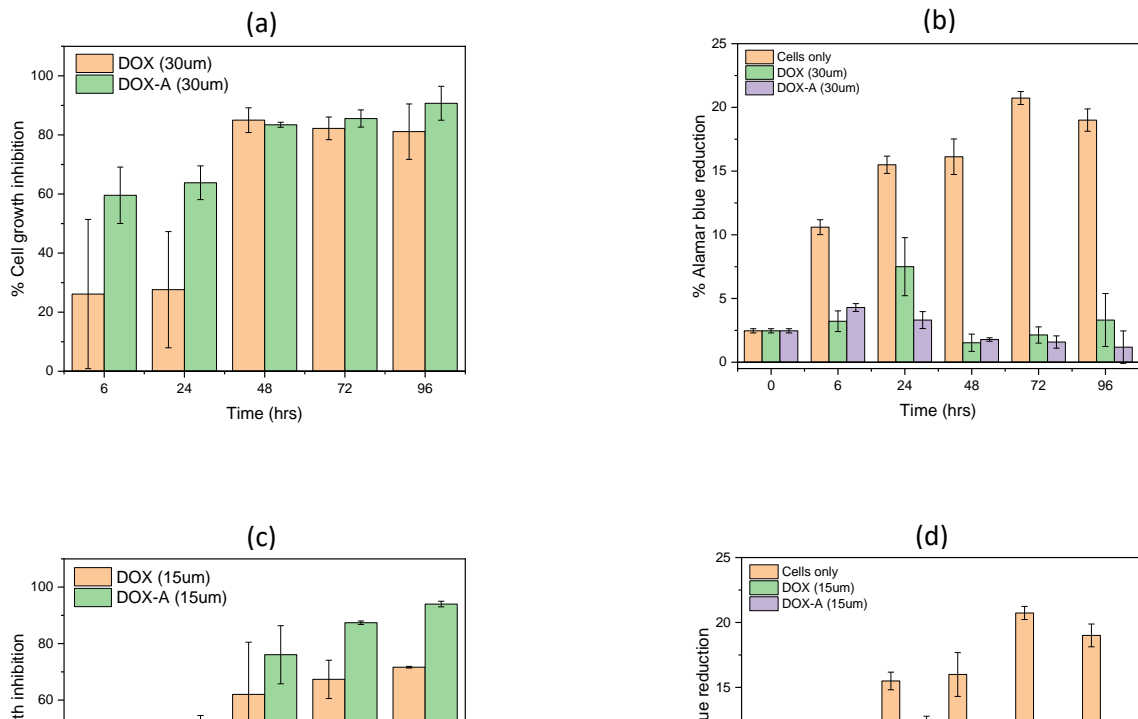
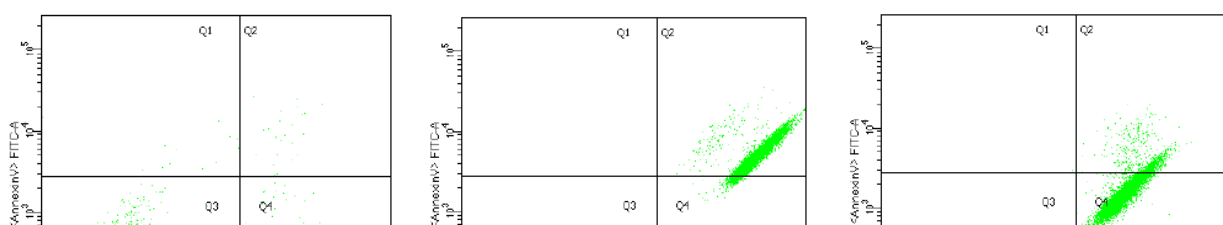


Figure 5.3: Percentage (a) \*CGI for 30 $\mu$ M (b) \*\*ABR for 30 $\mu$ M (c) \*CGI for 15 $\mu$ M (d) \*\*ABR for 15 $\mu$ M drug (DOX and DOX-A). \*Cell Growth Inhibition; \*\*Alamar Blue Reduction

### 5.2.2.6 Flow cytometry

To determine the method of cell death flow cytometry was carried out on DOX, DOX-A and the control sample using a flow cytometer BD Accuri™ C6 Plus (San Jose, CA, USA). Here results are analyzed based on certain physical and chemical characteristics of PC-3 cells as the fluid passes through a fluid stream with the help of a beam of laser light as they flow across a series of detectors. By utilizing mechanical or electrical devices to separate and collect cells with one or more measurable properties falling within a range or ranges of values selected by the user, flow sorting improves flow cytometry [30]. Cells were cultured at 20 000 cells in a T-75 flask at 37°C for 48 hours using appropriate medium to allow them adhere and develop their characteristic protein expression. The cells were de-trypsinised using trypsin EDTA (2ml) and cells were collected into a sterile micro centrifuge tube. The cells were rinsed with dPBS and also added to the already collected cells and centrifuged at 800rpm in order to collect both live and dead cells. 500ml of the cell apoptosis flow cytometry kit solution were added into the centrifuged cells and carefully agitated to ensure even distribution. The tubes were then wrapped with aluminum foil to avoid light effect. Hence measurements were taken using the flow cytometer and the result is as shown below figure 5.4.



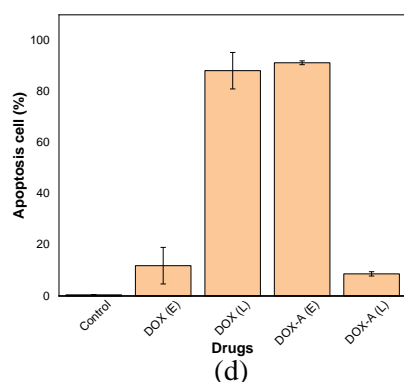


Figure 5.4: Flow cytometry result showing the cell viability of PC-3 cell death in (a) control without drug (b) DOX treated PC-3 (c) DOX-A treated PC-3 (d) The apoptotic rates of PC-3 cells treated with DOX and DOX-A. Data are presented as means  $\pm$  SD (n =3).  $P < 0.05$

### 5.2.3 *In vivo* Tumor Development and Targeted Drug Delivery

Cell culture, tumor induction, and drug injection studies were carried out in this section. T75 tissue culture flasks were used to cultivate 20 ml of  $1 \times 10^6$  PC-3 human prostate cancer cells (CELLTREAT, Pepperell, MA, USA). At 37°C, the cell culture was done until 70 % confluence was achieved. The cells were cultured in an F-12K medium with 10% FBS medium (ATCC, Manassas, VA, USA) supplemented with 100 I.U./ml penicillin/100Ig/ml streptomycin at normal atmospheric pressure. Envigo provided twenty-five (4-week-old) female Athymic Nude-Foxn1nu strain mice weighing approximately 28 g each (South Easton, MA, USA). The Worcester Polytechnic Institute Institutional Animal Care and Use Committee cleared these mice for use in this study (WPI IACUC). All of the mice were cared for in compliance with WPI IACUC standards and procedures. Each of the mice had

subcutaneous tumor xenografts introduced by injecting  $5.0 \times 10^6$  of PC-3 human prostate cancer cells (suspended in sterile saline) into the right femur/tibia-fibula area to promote angiogenesis. Palpation and digital calipers were used to assess the tumor formation and development respectively once in two days. The volume of the tumor was determined using the modified ellipsoidal formula below, where  $a$  and  $b$  representing the width (shorter axis,  $a$ , of the tumor measured perpendicular to the longer axis,  $b$ , of the tumor which is the length) and the length respectively.

$$\mathbf{Tumor\ Volume} = \frac{a^2 \times b}{2} \qquad 5.1$$

Due to animal welfare concerns, the mice were randomly allocated four treatment groups with each group consisting of three mice such that we had each of the groups being injected with saline only, DOX, DOX-A and then the control. A 12-day tumor development study was conducted on these mice. The weight of the mice and the tumor sizes were assessed every two days using digital calipers

#### **5.2.4 Studies on toxicity, histopathology, and electron microscopy**

After the administration of two doses of 10 mg/kg of DOX, DOX-A drugs to the athymic male nude mice which was induced subcutaneously for tumor shrinkage/treatment on a weekly basis for two weeks, qualitative toxicity was characterized by examining differences in mortality, changes in body weight, signs of poor health, general observations and the histopathology of the tumor, lungs, kidneys, liver and spleen. To screen for probable pharmacological side effects, daily observations and weight measurements were employed. For the various treatment groups, physiological changes, weight loss/gain, and the tumor volume and general well-being of the mice were measured. Tissue samples from the mice's kidneys, lungs, liver, spleen and tumor regions were taken at the end of each research and promptly fixed in 4 percent paraformaldehyde, dried in a graded series of alcohol, and

embedded in paraffin. Following the administration of the drug, hematoxylin and eosin (H and E) staining was used to detect tumor necrosis and analyze histologic alterations on important organs. 5 µm formalin-fixed, paraffin-embedded tissue/organ samples (tumor, kidneys, liver, spleen and lungs) for mice injected with DOX and AMACR-conjugated DOX and DMSO. These were hydrated by immersing them in increasing concentrations of alcohol baths and water (70, 90, and 100%). After that, the hydrated tissue sections were stained for 5 minutes in hematoxylin solution afterwards, 3 minutes of rinsing in a tap water and 5 minute of differentiation in 1% acid alcohol. After that, the parts were rinsed three times with tap water before being dipped in ammonia water for two minutes. then 10 minutes of eosin staining was done and the treated samples that has been sliced were subjected to dehydration using a solution of varying concentration of alcohol and xylene. In conclusion the samples were mounted using a few drops of Permount Mounting Medium. Using a TS100F Nikon microscope (Nikon Instruments Inc., Melville, NY, USA) and a DS-Fi3 C mount Nikon camera, the stained slides were ultimately photographed with a 20X objective lens.

Finally, the following; penicillin/streptomycin, a cell medium supplement and antibiotic were purchased from Thermo Fisher Scientific, Inc. (Waltham, MA, USA). Athymic Nude-Foxn1nu strain mice with individual weights of approximately 17 g was purchased from Envigo (South Easton, MA, USA). The Institutional Animal Care and Use Committee (IACUC) at the Worcester Polytechnic Institute, MA (IACUC docket # A2630 -17) approved all of the animal protocols, which were carried out in accordance with the National Institute of Health Guide for the Care and Use of Laboratory Animals.

### 5.2.5 AMACR Receptor Staining and *In vitro* cell viability

AMACR receptor staining was done using immunofluorescence staining of PNT-2 cells, which is a non-tumorigenic epithelial prostate cell line and PC-3 cells, an androgen-independent human advanced adenocarcinoma cell lines with AR expression negative with the aim of examining the expression of AMACR receptors on PNT-2 and PC-3 cell lines as shown in figure 5.5.

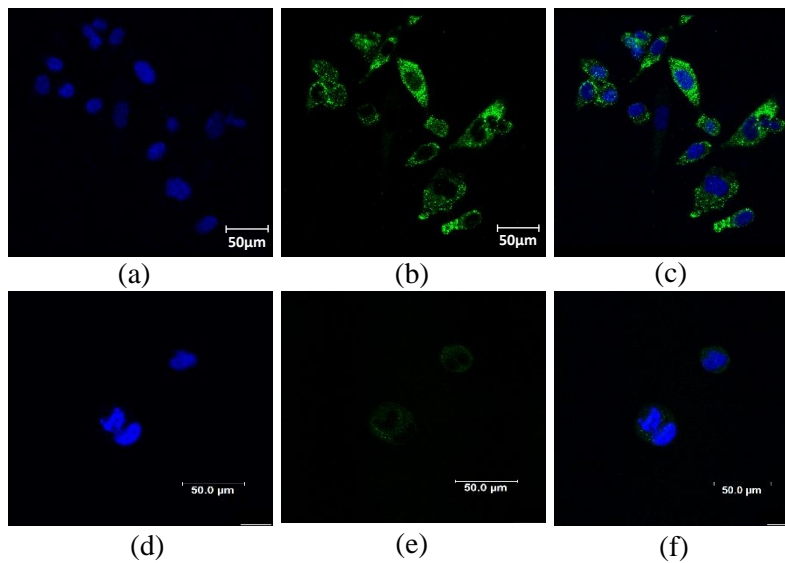


Figure 5.5: (a) PC3 cells (b) Overexpression of AMACR receptors (green) (c) Combined cells & AMACR stains (d) PNT-2 cells (e) Very low expression of AMACR receptors (green) (f) Combined cells & AMACR stains

Additionally, we performed immunohistochemistry (IHC) staining of prostate cancer and enlarged prostate gland tissue as shown in figure 5.6.

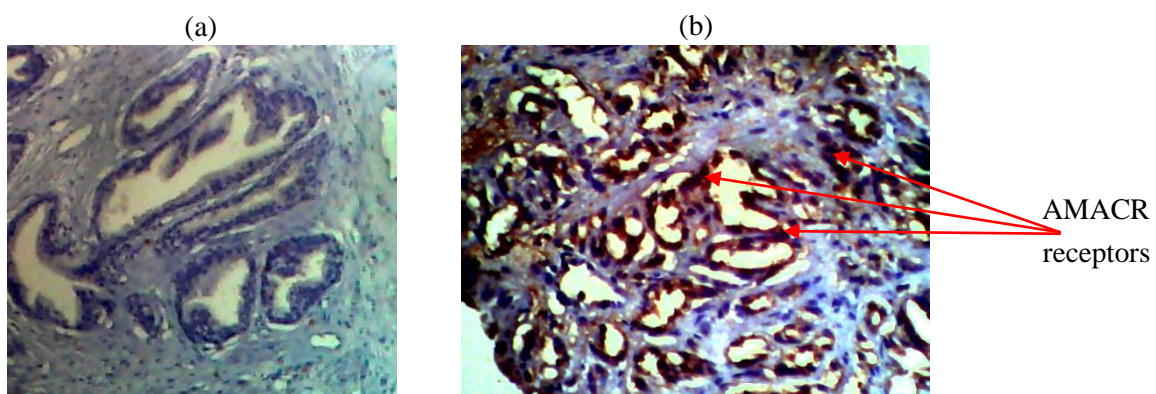


Figure 5.6: Optical micrograph of Immunohistochemistry staining of tissues at magnification of X40 (a) No expression of AMACR receptors on a benign prostatic hyperplasia (BPH) (b) Prostate tissue with overexpression of AMACR receptors (brown stains).

### 5.2.6 Immunofluorescence Staining

Using a technique reported in previous work, immunofluorescence (IF) labeling was performed to characterize the overexpressed receptors on the triple negative breast cancer tumor[13], [31]. The overexpression of AMACR receptors on prostate cancers was studied using IF staining. The frozen tumor tissue was progressively embedded in an optimal cutting temperature (OCT) compound. The tissues were frozen in a cryostat (Leica CM3050 S Research Cryostat, Leica Biosystems Inc., Buffalo Grove, IL, USA) to prevent them from thawing. Using a Leica cryomicrotome, 10  $\mu\text{m}$  thick slices of spleen, lungs, kidney, liver from frozen prostate cancer tumors (obtained from nude mice) these organs were sectioned on charged glass slides (Leica Biosystems Inc., Buffalo Grove, IL, USA). The sectioned organs were dried at room temperature (23  $^{\circ}\text{C}$ ) overnight. This was done to make adherence to the glass slides easier for immunofluorescence staining later on. The sliced tumor samples were incubated with 0.5 ml of 3% bovine serum albumin (Sigma-Aldrich, St. Louis, MO, USA) (blocking agent) made with PBS mixed with 30  $\mu\text{l}$  of triton X-100 after being adhered on glass slides (Life technologies Corporation, Carlsbad CA). This was done for 60 minutes at ambient temperature (23  $^{\circ}\text{C}$ ). To detect the levels of AMACR, the blocking agents were removed from the samples and treated with drops of 100  $\mu\text{l}$  of anti-AMACR Antibody (Millipore Sigma, Burlington, MA, USA), a primary antibody. This was done in a desirable dilution with a concentration of 1  $\mu\text{g}/\text{ml}$ . The samples were then incubated at 4  $^{\circ}\text{C}$  overnight before being dipped three times in 1X PBS (1 minute each time). The treated tumors were then incubated for another 2 hours with 50  $\mu\text{l}$  of anti-mouse IgG coupled with Alexa fluoro 488 secondary antibody at 1  $\mu\text{g}/\text{mL}$ . In a 1 % BSA solution, this secondary antibody was

produced at a concentration of 1 µg/ml. Thermo Fisher Scientific, Inc. (Waltham, MA, USA) was used to get both the primary and secondary antibody kits. Afterwards, the stained samples were washed three times for one minute each in 10 ml 1X PBS. In conclusion, drops of 5 µg/mL ProLong Gold antifade reagent with DAPI (Thermo Fisher Scientific Inc., Waltham, MA, USA) were used to stain the cell nuclei of the tumor samples. The samples obtained after the above process in a glass slides were fixed in a coverslip using some drops of Permout Mounting Medium. Using a Leica SP5 Point Scanning Confocal Microscope, the stained samples were imaged at a magnification of 60x (Leica TCS SP5 Spectral Confocal couple with Inverted Leica DMI 6000 CS fluorescence microscope, Leica, Buffalo Grove, IL, USA).

### **5.2.7 Studies on toxicity, histopathology, and electron microscopy**

The athymic male nude mice that was used in this research was induced with PC-3 subcutaneously after administering two doses of 10 mg/kg of DOX and DOX-A once in a week for two weeks. Several factors were observed in the course of the research on the mice ranging from differences in mortality, changes in body weight, poor health observation and the histology of the lungs, kidneys, spleen and liver (figure 5.7) at different phases of tumor development were used to characterize qualitative toxicity for tumor shrinkage/treatment. The mice were observed to ensure that there are no likely adverse effect arising from the bare and the conjugated drugs been injected to the mice intravenously, physiological changes, body weight gain/loss were measured once in three days on all the mice with the different drug formation and the control. At the end of each study, the aforementioned tissue samples were surgically removed from each mouse and then fixed in 4% paraformaldehyde, dried in alcohol of various grades and then embedded in paraffin. After injecting the mice with the bare and conjugated drug and upon completion of the study the haematoxylin and eosin staining was the method adopted to determine method of tumour necrosis and the organs

were analysed to see if there is any toxic effect of the drug on the organs (lungs, spleen, kidney and liver).

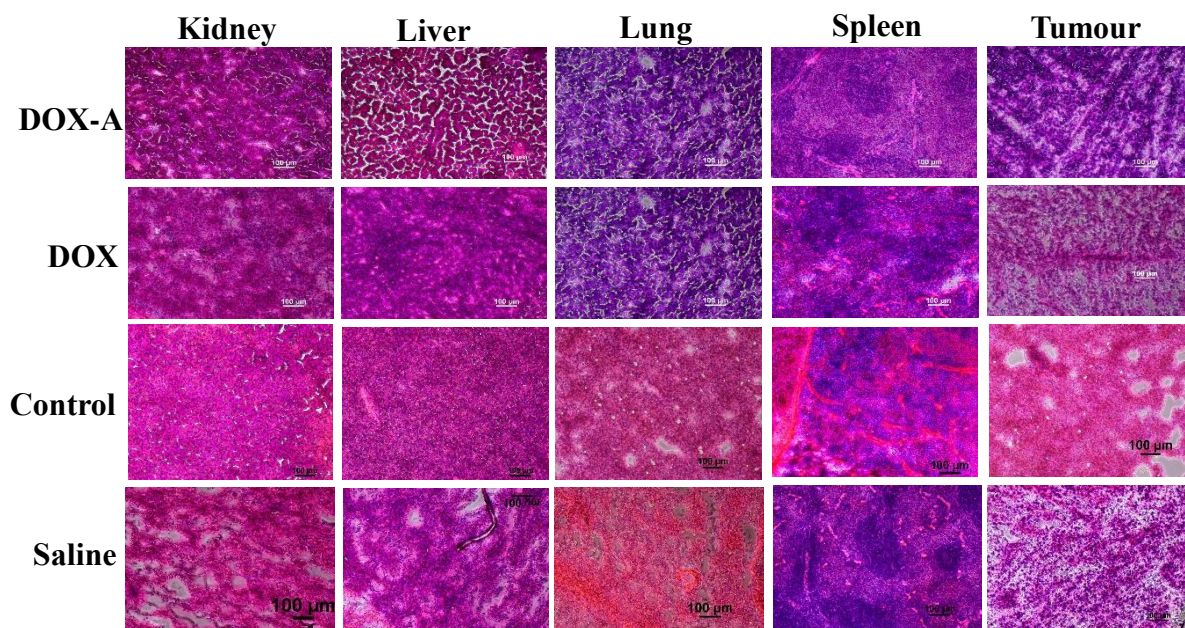


Figure 5.7: Histopathological examination of tumour tissues and organs in PC-3 induced xenograft prostate tumour model mice after treatment (from 12-day treatment group) with unconjugated DOX and DOX-A drugs.

### 5.3 Results

#### 5.3.1 Results of IHC, IF, drug conjugation and characterization

Immunohistochemistry (IHC) was used to examine samples of prostate cancer tissues and enlarged prostate gland tissue taking in a national hospital in Abuja, Nigeria in Africa with the aim of examining the overexpressed receptor(s) on the PC and the enlarged prostate gland tissues to facilitate the localized drug delivery. The optical image result of the staining revealed that AMACR (brown stains) were overexpressed on the PC tissue and non was observed on the enlarged prostate gland figure 5.6.

Furthermore, immunofluorescence (IF) staining was done on PC-3 cells to revealed the expression of AMACR receptors (figure 5.5), it was observed that AMACR receptors were overexpressed on PC-3 cells (green stains) [32] stained with unblocked AMACR antibody

receptors, the receptor expression obtained using fluorescent confocal microscope is as shown in figure 5.5. Whereas the AMACR expression on the PNT-2 was very low.

Hence, Doxorubicin (DOX) was conjugated with AMACR to form DOX-A in the presence of NHS as the hydrophilic linker that creates sites for the lysine group in the doxorubicin and the presence of EDC facilitates DOX cleavage to the N-H group thereby making the conjugation with AMACR easier. The conjugated protocol followed the principle highlighted in the work by T. Aina *et al.* 2022. To determine whether the conjugation was properly done, the UV-Vis of DOX, DOX-A and AMACR, was compared as shown in figure 5.2. At a wavelength of 481.5nm a peak was observed for the DOX whereas that of DOX-A and AMACR existent at 490nm and 276.5nm respectively. This results shows that the bare drug and the conjugated drug exhibit distinct wavelengths as shown in figure 5.2 at which they are absorbed. The first peak of 276.5 nm becomes apparent at 253.5 nm, suggesting the possibility of conjugation between AMACR and DOX, and the peaks for DOX-A moved to the right, from 481.5 nm to a wider peak of 490 nm, as seen in figure 5.2.

The FTIR result showed the following: N-H stretching vibrations at  $3309.86\text{ cm}^{-1}$  [33],  $\text{CH}_2$  asymmetric and symmetric stretching vibrations at  $2979.03$  and  $2897.82\text{ cm}^{-1}$ [34]. The peak situated at  $1734.41\text{ cm}^{-1}$  assigned to C=O stretching vibration [35] from the ester groups. The amide bond was located around  $1617.50\text{ cm}^{-1}$ . Ester bond stretching vibrations and C-N stretching vibrations are situated at  $1296\text{ cm}^{-1}$ , respectively. Absorption at 1026, 1071,  $951.68$  and  $703.6\text{ cm}^{-1}$  represents the presence of the aromatic bonds. Conjugated drug is seen from the new peaks formed at  $3393.73\text{ cm}^{-1}$ .

### **5.3.2 In vitro cell viability**

After 96 hours, both the bare (DOX) and conjugated (DOX-A) drug significantly decreased the viability of PC-3 cells, hence, DOX-A has the higher cell growth inhibition as shown in

figure 5.3. Additionally, cells treated with the conjugated drug had lower cell viability than cells exposed to the bare nanoparticles, indicating that the conjugated drug formulation had stronger anti-proliferative effects on PC-3 cancer cells which is consistent with the aim of the paper. The conjugated drug, DOX-A reduced PC-3 cell viability more than the bare (DOX) drug after 96 hours of treatment and there was no significant difference between DOX and DOX-A groups at that time ( $p < 0.05$ ). The percentage alamar blue reduction after 96 hours' treatment shows that in both concentrations, DOX-A resulted in lower ABR when compared with the bare drug, DOX as shown in figure 5.3(b and d).

This result shows that AMACR-conjugated drug (DOX-A) were more effective in inhibiting the growth of the PC-3 prostate cancer cells because of the specificity that was enabled by the conjugation of the DOX drug with AMACR *in vivo*, and this was further aided by the force of adhesion between the overexpressed AMACR receptors on the prostate cancer cells and the AMACR peptide on the drug (DOX-A). Although both 15 $\mu$ M and 30 $\mu$ M were effective concentrations in preventing the cell growth, the smaller concentration, 15 $\mu$ M was more effective in preventing the growth of PC-3 cells *in vitro* compared to the 30 $\mu$ M.

Further analysis was carried out to determine the method of cell death using a flow cytometer. Here results are analyzed based on certain physical and chemical characteristics of PC-3 cells as the fluid passes through a fluid stream with the help of a beam of laser light as they flow across a series of detectors. By utilizing mechanical or electrical devices to separate and collect cells with one or more measurable properties falling within a range or ranges of values selected by the user, flow sorting improves flow cytometry [30].

The result shows cells treated with DOX, 88.15% of the cell death occurs in the second quadrant and the remaining 11.85% cell death occur in the fourth quadrant which shows that cell death here was by early stage apoptosis. On the other hand, the cells that were treated

with the conjugated drug DOX-A, 91.25% of the cell death occurred in the fourth quadrant whereas the remaining cell death, 8.75% occurred in the second quadrant showing that the method of cell death is by late state apoptosis. The control shows that a greater number of the cell occurred in the third quadrant as shown in figure 5.4a above, which is a case of cells still alive because the cells were not treated with any drug formulation

### 5.3.3 Result of tumor growth and shrinking *in vivo*

On day 5, the mean tumor volume in the nude mice treated with DOX, DOX-A, saline and control without drugs are 50.3 mm<sup>3</sup>, 99.8 mm<sup>3</sup>, 75.9 mm<sup>3</sup>, and 64.1 mm<sup>3</sup> respectively and at day 12, the mean tumor volume in the animals treated with DOX, DOX-A, saline and control without drugs are 49.4 mm<sup>3</sup>, 55.5 mm<sup>3</sup>, 241.6 mm<sup>3</sup> and 151.9 mm<sup>3</sup> respectively. The tumors reduced significantly after treating the mice with the respective bare and conjugated drug after 12 days following injection of 10 mg/kg DOX-A and DOX into each animal (one dosage per week) in the day-12 treatment group as shown in figures 5.8 a and b, the tumor sizes shows that both DOX and DOX-A are capable of causing tumor shrinkage with DOX-A causing a higher tumor shrinkage.

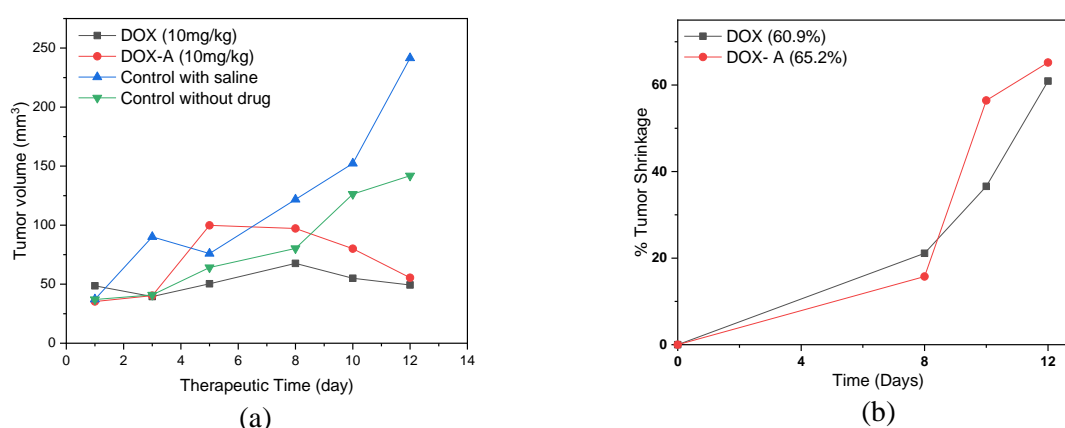


Figure 5.8: (a) Anti-tumour efficacy and tumour reduction in male athymic nude mice treated with two injections of DOX, DOX-A, and Saline over a 12-day trial period (b) percentage tumour shrinkage (n = 3, P<0.05)

After two weeks (one per week) of administration of 10 mg/kg of DOX-A and DOX, substantial xenograft tumour reduction was observed in the 14-day treatment with a percentage tumour shrinkage been ~82% and ~75% for DOX-A and DOX treated xenograft tumours. The result shows that conjugating DOX with AMACR is a potential targeted drug delivery cargo capable of causing xenograft tumour shrinkage provided substantial amount (at least two doses) of drugs is been administered to the xenograft prostate cancer tumour.

After receiving therapy (12-day treatment group) with unconjugated and AMACR-conjugated DOX, tumor tissues and organs in PC-3-induced xenograft prostate tumor model mice were examined histopathologically. This tumor shrinkage was accomplished with no signs of toxicity (Figure. 4.7). The late-stage tumors that developed after 12 days significantly shrank under the same drug dose, with no discernible toxicity (Figure 4.7). This implies that additional therapies (beyond the two-week injection time investigated in this study) could be able to completely eliminate mid- and late-stage malignancies.

#### **5.4 Implications of the results**

The results of this research have important significance for the development of drugs targeted and localized for the treatment of prostate cancer. We have demonstrated that conjugating AMACR peptides to cancer drugs DOX to form DOX-A greatly improves the transport of those drugs to PC tumor locations. First the DOX was conjugated with AMACR antibodies. The targeted delivery of PC drug helps to lessens the adverse effects that usually arises as a result of bulk chemotherapy. To properly understand the cause of the conjugated drug adhering faster the unconjugated drug, the work done by J. Hu 2020 [13], [36] in the group provided an insight. Increased hydrogen bonds and Van der Waal interactions between AMACR attached to the drug and the overexpressed AMACR receptors on the surfaces of prostate cancer cells/tissue are possible factors responsible for the equivalent increase in adhesion forces between AMACR-conjugated drugs and the prostate cancers. Hence, the

immunofluorescence (IF) and immunohistochemistry (IHC) staining of the expressed AMACR receptors makes AMACR a potential target in PC drug delivery and may quantitatively confirm the assertions made by the adhesion forces been responsible for AMACR ligands binding to the receptors expressed on the cells/tissue. However, the findings from experiments on alamar blue cell viability (figure 5.3) demonstrate that the receptors work to increase the specificity of the conjugated drug to the AMACR receptors of the PC-3 cell lines. Additionally, it is necessary to obtain additional understanding and decipher direct evidence of interactions or binding between AMACR ligand and their receptors expressed on cells and tissues utilizing a combination of tagged fluorescent receptors and CRISPR analysis. The intravenous injection of DOX-A administered via the tail vein also caused the xenograft tumors that were produced subcutaneously at the interscapular locations to decrease at the late stage of tumor growth. Furthermore, athymic nude mouse model was employed in the present work, the AMACR conjugation of the doxorubicin also considerably improved the precise targeting of PC. The drug's precise method of delivery had few adverse effects as well. It is significant to note that the tumors developed within the late stage of tumor growth shrunk in response to the second injection of 10 mg/kg of AMACR-conjugated doxorubicin (within 12 days) without any signs of toxicity, this tumor reduction was accomplished. This implies that if explored, additional treatments beyond the 12-day trial and beyond the two drug dosages might completely eradicate the PC cancers.

As a result, the findings from the ex vivo histopathology/microscopy, immunofluorescence staining, drug-tumor adhesion prediction, and in vitro cell viability study demonstrated that the improved therapeutic effects are linked to the increased adhesion forces/interactions of the AMACR-conjugated cancer drugs DOX-A with the AMACR receptors overexpressed on the PC cells/tissue. These lead to advancements in the precise targeting of PC cells and tissue as well as the eradication or contraction of PCs, all of which were seen in this study. To

further confirm this work more research will be required in the future to show the observable effects of the conjugated and unconjugated medications on animals. Additional research is required to examine the effects of various medication doses in animal models in order to target various cancer types such as kidney, liver, colon, and cells that express AMACR receptors.

### **5.5 Statistical analysis**

The statistical data was examined with the help of OriginPro 2019 program. To compare the differences between the control and study groups, independent Student t tests and one-way analyses of variance (ANOVA) were performed. The difference in their population means were used to assess the statistical significance of the percentage survival of drug-treated mice with the control mice. The effects of bare drug (DOX) and conjugated cancer drugs (DOX-A) were statistically analyzed. A p-value was obtained for  $p < 0.05$  and it was deemed significant.

### **5.6 Conclusion**

Targeting PC cells/tissue's overexpressed AMACR receptors in both in vitro and in vivo settings, we have effectively produced a unique AMACR-conjugated DOX drug (DOX-A). Our findings imply that the higher adherence of the AMACR-conjugated drug to PC cells/tissues during in vitro and in vivo experiments enhances the selective targeting. Additionally, the AMACR-conjugated drug (DOX-A) increases PC-3 PC inhibition more than the unconjugated drug (DOX). Our findings for the in vivo investigations indicate that early stage prostate tumors shrank after receiving two injections of 10 mg/kg of AMACR-conjugated doxorubicin (DOX-A) during a two-week period (12-days tumor-treatment group) in the athymic nude male mice. Therefore, the enhanced adherence of the AMACR to the AMACR receptors that are overexpressed on the surfaces of the PC cells/tissue during PC

development is responsible for the improved specificity of the AMACR-conjugated drug (in the targeting of PC).

Furthermore, the results of the *ex vivo* histopathology studies did not provide any indication that the administration of an AMACR-conjugated drug caused any physiological alterations. After receiving the conjugated drug, DOX-A, there were no unfavorable variations in mortality or body weight compared to control mice. This indicates that DOX-A effectively and specifically suppressed the growth of the generated xenograft PC tumors in the athymic nude mice. Therefore, the current findings demonstrate that AMACR-conjugated DOX considerably improves the targeted and localized therapy of PCs without producing unfavorable toxicological consequences.

## 5.8 Bibliography

- [1] H. Sung *et al.*, “Global Cancer Statistics 2020: GLOBOCAN Estimates of Incidence and Mortality Worldwide for 36 Cancers in 185 Countries,” *CA. Cancer J. Clin.*, vol. 71, no. 3, pp. 209–249, 2021, doi: 10.3322/caac.21660.
- [2] S. Tai *et al.*, “PC3 Is a Cell Line Characteristic of Prostatic Small Cell Carcinoma,” *Prostate*, vol. 71, pp. 1668–1679, 2011, doi: 10.1002/pros.21383.
- [3] “A Probasin-Large T Antigen Transgenic Mouse Line Develops Prostate Adenocarcinoma and Neuroendocrine Carcinoma with Metastatic Potential1 | Cancer Research | American Association for Cancer Research.” [Online]. Available: <https://aacrjournals.org/cancerres/article/61/5/2239/508674/A-Probasin-Large-T-Antigen-Transgenic-Mouse-Line>. [Accessed: 10-Mar-2022].
- [4] F. A. Baig, A. Hamid, T. Mirza, and S. Syed, “Ductal and Acinar Adenocarcinoma of Prostate: Morphological and Immunohistochemical Characterization,” *Oman Med. J.*, vol. 30, no. 3, pp. 162–166, 2015, doi: 10.5001/omj.2015.36.
- [5] M. A. Castanares *et al.*, “Characterization of a novel metastatic prostate cancer cell line of LNCaP origin.,” *Prostate*, p. 11, 2016, doi: <https://doi.org/10.1002/pros.23115>.
- [6] Q. Li *et al.*, “Linking prostate cancer cell AR heterogeneity to distinct castration and enzalutamide responses,” doi: 10.1038/s41467-018-06067-7.
- [7] D. G. Tang, “Understanding cancer stem cell heterogeneity and plasticity,” *Nat. Publ. Gr.*, vol. 22, pp. 457–472, 2012, doi: 10.1038/cr.2012.13.
- [8] R. Wen, H. Zhao, D. Zhang, C. L. Chiu, and J. D. Brooks, “Sialylated glycoproteins as biomarkers and drivers of progression in prostate cancer,” *Carbohydr. Res.*, vol. 519, p. 108598, Sep. 2022, doi: 10.1016/J.CARRES.2022.108598.
- [9] Q. Fu *et al.*, “Proteomics reveals MRPL4 as a high-risk factor and a potential diagnostic biomarker for prostate cancer,” *Proteomics*, p. 2200081, Sep. 2022, doi: 10.1002/PMIC.202200081.
- [10] N. Eke and M. Sapira, “Prostate cancer in Port Harcourt, Nigeria: features and outcome,” *Nigerian Journal of Surgical Research*, vol. 4, no. 1. pp. 34–44, 2002, doi: 10.4314/njsr.v4i1.12167.
- [11] A. Shehzad, *Cancer Biomarkers in Diagnosis and Therapeutics*. 20222.
- [12] K. L. Stratton and A. K. Morgans, *Urologic Oncology*. Gewerbestrasse: Springer Nature, 2005.

- [13] J. D. Obayemi *et al.*, “LHRH-Conjugated Drugs as Targeted Therapeutic Agents for the Specific Targeting and Localized Treatment of Triple Negative Breast Cancer,” *Sci. Rep.*, vol. 10, no. 1, Dec. 2020, doi: 10.1038/S41598-020-64979-1.
- [14] S. Dhar, F. X. Gu, R. Langer, O. C. Farokhzad, and S. J. Lippard, “Targeted delivery of cisplatin to prostate cancer cells by aptamer functionalized Pt(IV) prolonged-PLGA-PEG nanoparticles,” vol. 105, no. 45, p. 6, 2008, doi: org/10.1073/pnas.0809154105.
- [15] I. F. Tannock, B. Seruga, A. Ocana, and I. F. Tannock, “Drug resistance in metastatic castration-resistant prostate cancer,” *Nat. Rev. Clin. Oncol.*, vol. 12, no. 8, pp. 12–23, 2011, doi: 10.1038/nrclinonc.2010.136.
- [16] “A New Class of Cancer Drugs May Be Less Toxic - The New York Times.” [Online]. Available: <https://www.nytimes.com/2012/06/01/business/a-new-class-of-cancer-drugs-may-be-less-toxic.html>. [Accessed: 13-Mar-2022].
- [17] G. Passeri, J. Northcote-Smith, and K. Suntharalingam, “Delivery of an immunogenic cell death-inducing copper complex to cancer stem cells using polymeric nanoparticles,” *R. Soc. Chem.*, vol. 5290, no. 12, p. 10, 2022, doi: 10.1039/d1ra08788f.
- [18] A. Urbanucci *et al.*, “Overexpression of androgen receptor enhances the binding of the receptor to the chromatin in prostate cancer,” *Oncogene*, vol. 31, no. 17, pp. 2153–2163, Apr. 2012, doi: 10.1038/ONC.2011.401.
- [19] A. Lacouture, C. Lafront, C. Peillex, M. Pelletier, and É. Audet-Walsh, “Impacts of endocrine-disrupting chemicals on prostate function and cancer,” *Environ. Res.*, vol. 204, p. 112085, Mar. 2022, doi: 10.1016/J.ENVRES.2021.112085.
- [20] M. Shiota, N. Fujimoto, E. Kashiwagi, and M. Eto, “cells The Role of Nuclear Receptors in Prostate Cancer,” 2019, doi: 10.3390/cells8060602.
- [21] T. Osada *et al.*, “HSP90-Specific nIR Probe Identifies Aggressive Prostate Cancers: Translation from Preclinical Models to a Human Phase I Study,” *Mol. Cancer Ther.*, vol. 21, no. 1, pp. 217–226, 2022, doi: 10.1158/1535-7163.MCT-21-0334.
- [22] J. Wang, J. Weng, Y. Cai, R. Penland, M. Liu, and M. Ittmann, “The Prostate-Specific G-Protein Coupled Receptors PSGR and PSGR2 Are Prostate Cancer Biomarkers that Are Complementary to  $\alpha$ -Methylacyl-CoA Racemase,” *Prostate*, vol. 66, pp. 847–857, 2006, doi: 10.1002/pros.20389.
- [23] L. A. Dykman *et al.*, “Gold nanoparticle-aided preparation of antibodies to  $\alpha$ -methylacyl-CoA racemase and its immunochemical detection,” *Gold Bull. 2016 493*, vol. 49, no. 3, pp. 87–94, Nov. 2016, doi: 10.1007/S13404-016-0186-4.
- [24] Y. Teng *et al.*, “Current Knowledge on the Function of  $\alpha$ -Methyl Acyl-CoA Racemase in Human Diseases,” 2020, doi: 10.3389/fmolb.2020.00153.
- [25] B. A. P. Wilson *et al.*, “High-Throughput Screen Identifies Novel Inhibitors of Cancer Biomarker  $\alpha$ -Methylacyl Coenzyme A Racemase (AMACR/P504S),” doi: 10.1158/1535-7163.MCT-10-0902.
- [26] P. Bhaumik, W. Schmitz, A. Hassinen, J. Kalervo Hiltunen, E. Conzelmann, and R. K. Wierenga, “The Catalysis of the 1,1-Proton Transfer by  $\alpha$ -Methyl-acyl-CoA Racemase Is Coupled to a Movement of the Fatty Acyl Moiety Over a Hydrophobic, Methionine-rich Surface,” *J. Mol. Biol.*, vol. 367, pp. 1145–1161, 2007, doi: 10.1016/j.jmb.2007.01.062.

- [27] S. Zha *et al.*, “Methylacyl-CoA Racemase as an Androgen-Independent Growth Modifier in Prostate Cancer 1,” *Johns Hopkins Med. Institutions*, vol. 63, pp. 7365–7376, 2003.
- [28] J. D. Obayemi *et al.*, “Degradable porous drug-loaded polymer scaffolds for localized cancer drug delivery and breast cell/tissue growth,” *Mater. Sci. Eng. C*, vol. 112, no. March, p. 110794, 2020, doi: 10.1016/j.msec.2020.110794.
- [29] S. M. Jusu *et al.*, “Plga-cs-peg microparticles for controlled drug delivery in the treatment of triple negative breast cancer cells,” *Applied Sciences (Switzerland)*, vol. 11, no. 15, 2021, doi: 10.3390/app11157112.
- [30] H. M. Shapiro, *Practical Flow Cytometry*, 4th ed. John Wiley & Sons, 2005.
- [31] J. D. Obayemi *et al.*, “Adhesion of ligand-conjugated biosynthesized magnetite nanoparticles to triple negative breast cancer cells,” *J. Mech. Behav. Biomed. Mater.*, vol. 68, no. August 2016, pp. 276–286, 2017, doi: 10.1016/j.jmbbm.2017.02.004.
- [32] W. Chen *et al.*, “Molecular cloning and preliminary analysis of the human  $\alpha$ -methylacyl-CoA racemase promoter,” *Mol. Biol. Rep.*, vol. 36, no. 3, pp. 423–430, Mar. 2009, doi: 10.1007/S11033-007-9196-X/FIGURES/6.
- [33] G. F. Svatos, C. Curran, and J. V. Quagliano, “Infrared Absorption Spectra of Inorganic Coördination Complexes. V. The N-H Stretching Vibration in Coördination Compounds,” *J. Am. Chem. Soc.*, vol. 77, no. 23, pp. 6159–6163, 1955, doi: 10.1021/JA01628A019.
- [34] S. Manivel, B. S. Gangadharappa, N. Elangovan, R. Thomas, O. A. Abu Ali, and D. I. Saleh, “Schiff base (Z)-4-((furan-2-ylmethylene)amino) benzenesulfonamide: Synthesis, solvent interactions through hydrogen bond, structural and spectral properties, quantum chemical modeling and biological studies,” *J. Mol. Liq.*, vol. 350, p. 118531, 2022, doi: 10.1016/j.molliq.2022.118531.
- [35] C. k. Enenebeaku, N. J. Okorochoa, E. Nzediegwu, and U. E. Enenebeaku, “Removal of Methyl Violet Dyes from Aqueous Solution using Almond (*Prunus dulcis*) Seed Shell,” *IOSR J. Appl. Chem.*, vol. 09, no. 08, pp. 01–13, 2016, doi: 10.9790/5736-0908010113.
- [36] J. Hu *et al.*, “Investigation of adhesive interactions in the specific targeting of Triptorelin-conjugated PEG-coated magnetite nanoparticles to breast cancer cells,” *Acta Biomater.*, vol. 71, pp. 363–378, 2018, doi: 10.1016/j.actbio.2018.02.011.

## CHAPTER SIX

### 6.0 Release kinetics of fungicidal antimicrobials into packaged foods

#### 6.1 Introduction

The growth of pathogenic microorganisms on food leads to spoilage/degradation [1], [2]. To ensure that fresh and processed food reach desired consumers with little or no degradation, the food must be packaged in an environmental condition that limits the tendency of degradation by fungi attack during the period between packaging and consumption by the consumer [2], [3]. Antimicrobial food packaging includes any packaging system(s) adopted to control the growth of harmful microbes in food products [4]. Statistics by the United Nations Food and Agriculture Organization shows that, 32% of all food produced based on weight in the world is lost/wasted [5]–[8]. This amounts to ~24% in calories of food lost globally [9], [10]. It is also important to note that 56% of total food lost/wasted occurred in developed countries like China, Japan and the remaining 44% occurs in developing countries [10] hence, the need to remedy this situation. There are different stages of food lost; 24% of global food lost/wasted occurs at the production stage, 24% in the process of handling and storage and 35% at the consumption stages. These three amounted to 80% of global food lost/wasted in 2009 [10]. There is, therefore, a need for improved methods for food

preservation. One approach to food preservation is to use the controlled release of antimicrobial agents (from food packaging) as a way of preserving packaged foods. Controlled release packaging (CRP) is a form of packaging technology that is currently employed in the food packaging industry [11], [12]. It uses the controlled release of antimicrobials and fungicidal (active) agents [9], [13]–[15] to manage the quality and safety of food, while extending the shelf lives of packaged foods. In this way, the active agent creates an enabling environment for the preservation of the packaged foods [16]. Gemili et al. (2010) has studied the effect of incorporating lysozyme into cellulose acetate (CA). The study revealed that the maximum release of the antimicrobial agent (into a packaged food) was obtained with 5% CA and 1.5% lysozyme and asymmetric CA film [7]. Other studies have also shown that the release of antimicrobial agents can be accomplished either by direct contact of the food with the package or by diffusion from the packing layer to the surface of food [7], [17]–[19]. This has paved the way for the development of “smart packaging” that can release different types of active agents that enable improvements in food preservation [20], [21]. Furthermore, to immobilize antimicrobials using ionic or covalent linkages, the polymer to be used and the antimicrobial agent must have a functional group. Examples of polymers that have functional groups are ionomeric films [22], polystyrene [23], polyvinyl alcohol [24], nylon 6, 6 resins, peptides [13], enzymes [25], and polyamines [26]. Moreover, antimicrobial films formed with chitosan based polymers are useful as a medium to transporting acids and spices to targeted materials [27]. Prior work has been done in the areas of antimicrobial food packaging to prove the efficacy of antimicrobial agents in preserving several kinds of food as earlier mentioned [22], [27], however, there is need for further research to improve on the existing work that has been done. Further study could help in controlling the release of antimicrobial food packaging by testing its efficacy on selected food items over a prolonged period of time. Applying mathematical model in ways that will

help in the optimization of antimicrobial food package designs to back up the experimental result will be helpful. Achieving further shelf life extension through the design of model packaging to further control the release of AM agents to packaged food stuffs will be a welcome development.

Technological advancement also suggests the design of smart package that can notify the store keeper of the food expiry date. Finally, the formation of polymeric pellets that have antimicrobial agent incorporated into it is also an area with lots of potential for research.

Essentially, potassium sorbate has the capacity to inhibit the following microorganisms; Fungi (e.g., *Penicillium Commune*), Mold (e.g., *Alternaria*, *Cephalosporium*, *Helminthosporium*, *Penicillium*), Yeast (e.g., *Brettanomyces*, *Hansenula*, *Sporobolomyces*), Bacteria (e.g., *Acetobacter*, *Clostridium*, *Vibrio* [28], [29]). A good example of the areas of application of PS is seen in Cheese where 1000 µg/mL of PS was able to inhibit the growth of *Penicillium verrucosum* var. *cyclopium*, also ≤ 6% of PS was able to inhibit the growth of *Penicillium roqueforti*; *Mucor miehi*. Hence, the choice of PS incorporated into polymers to prolong food shelf life [30], but little is known about its antimicrobial properties in CA. Edible films has recently found some application as AM agents and the AMA being released is regulated to ensure that exact concentration is permitted into the food [31] and this study is not an exception as it explores the above areas. In this article, we explore the effects of the controlled release of fungicidal antimicrobials in the preservation of packaged foods (peanuts and bread). These are encapsulated in films (2 mm thick) to regulate the AM agent release into packaged foods. The article is divided into five sections. Following the introduction (section 1), the materials and methods are presented in Section 2. This is followed by Section 3 in which the theoretical framework for the modelling of antimicrobial release is presented. The results obtained from the current study are discussed in Section 4, before summarizing the conclusions arising from the current work in Section 5.

## 6.2 Materials and methods

### 6.2.1 Materials

PS ( $C_6H_7KO_2$ ), with relative molecular mass of  $150.22 \text{ gmol}^{-1}$  was obtained from Qualikems Laboratory Reagents (New Delhi, India). Chloramphenicol was procured from Merck (City, NJ). Acetone ( $CH_3COCH_3$ ) with molecular weight of  $58.08 \text{ g/mol}$  was procured from Sigma–Aldrich (Taufkirchen, Germany). Cellulose acetate with molecular weight of  $29,000 \text{ g/mol}$  was procured from Fluka (Milwaukee, Wisconsin). Sucrose ( $C_{12}H_{22}O_{11}$ ) with molecular weight of  $342.30 \text{ g/mol}$ , melting point of  $185\text{--}187^\circ\text{C}$ , and solubility of  $H_2O:0.5 \text{ g/mL}$ , was obtained from Sigma Aldrich (Taufkirchen, Germany), while Agar was obtained from Fisher Scientific (City, NJ), Celestron Pentaview LCD Digital microscope (Torrance, CA), The software used for the simulation was COMSOL Multiphysics® (COMSOL, Inc. Burlington, MA).

### 6.2.2 Methods

#### 6.2.3 Preparation of Cellulose Acetate (CA) Film

To make CA film, PS was dissolved in water, while cellulose acetate (CA) was dissolved in acetone [21]. Then PS/water solution was added to the CA/acetone solution using syringe in a drop wise fashion under stirring until there was fairly homogeneity in the mixture of CA solution in PS/water solution. The stirring of the mixture was done until there was complete dissolution of all the PS solution in the CA solution. After obtaining a homogenous mixture, the solution was kept in a vacuum oven for 30 min at  $25^\circ\text{C}$ . This was done to eliminate the bubbles formed on the antimicrobial films. The concentration of PS in the film was kept constant at 2% (w/w) during the experiments in which the concentration of CA was varied (10%, 13% and 15%, by weight). The films formed at  $24^\circ\text{C}$  are shown in Table 6.1. The films with the code  $M_{15}^+$ ,  $M_{13}^+$  and  $M_{10}^+$  represents the film with AMA whereas  $M_{15}^-$ ,  $M_{13}^-$  and

M<sub>10</sub><sup>+</sup>, stands for films acting as control without AMA incorporated into it. 15, 13 and 10 are the weight percent of CA in the film.

#### **6.2.4 Characterization of the films**

The surface morphologies of the films and the cross-sectional areas of the films were examined using a Scanning Electron Microscope (SEM) (Philips XL-30SFG, Leuven, Belgium). A UV–vis Spectrophotometer (UV-1900i, Shimadzu, Kyoto, Japan) to measure the absorbance of potassium sorbate in a solution containing antimicrobial film dissolved in distilled water over a period of 10 days and also to check the effect of porosity in the release of the AM agent.

#### **6.2.5 Release tests**

Antimicrobial release tests were carried out on three films formed on a mini-glass petri dish as the mold. The films, with different concentrations of cellulose acetate, were placed on a 10 cm glass petri dish containing 100 mL of distilled water (pH ~ 7.00) at a temperature of 25°C. The content of the petri dish was formed by stirring it in a beaker using a magnetic stirrer and a rod at a speed of 240 rpm, the mixture was poured into the dish. The release of the PS into distilled water was determined by collecting 100 µl samples at regular time intervals of 15 hr, while fresh volume of distilled water was replaced. After 1 mL dilution with distilled water, the absorbance of the PS was measured at 252 nm in UV–Vis spectrometer based on Beer–Lambert law, which gives a linear relationship between absorbance and concentration of an absorbing species:

$$A = \epsilon lc \quad 6.1$$

where A is absorbance (au),  $\epsilon$  is the molar absorptivity constant  $\text{dm}^3/\text{mol}\cdot\text{cm}$ , l is the path length (the distance of the solution that the light has to travel through, 1 cm) and C, is the concentration of the solution, expressed in  $\text{molL}^{-1}$  or  $\text{mol}\text{dm}^{-3}$ .

Table 6.1: Types of films and their codes prepared at 24°C

<b>Film code</b>	<b>Number of layers</b>	<b>Film thickness (mm)</b>	<b>Composition of CA (%w/w)</b>
M <sub>15</sub> <sup>+</sup>	Single	2	15
M <sub>13</sub> <sup>+</sup>	Single	2	13
M <sub>10</sub> <sup>+</sup>	Single	2	10
M <sub>15</sub> <sup>-</sup>	Single	2	15
M <sub>13</sub> <sup>-</sup>	Single	2	13
M <sub>10</sub> <sup>-</sup>	Single	2	10

### 6.2.6 Preparation of potato dextrose agar (PDA)

With the aid of an analytical weighing balance ABS Kern, ABS 80-4N + 963-101 (Sigma–Aldrich, Kern, UK), 300 g of chopped Irish potato were weighed, while 1 L of distilled water was added to the sliced potato infusion. The mixture was boiled for 1 hr at 100°C. Soil

samples (2 g) were collected from a land fill refuse bin in Galadimawa, Abuja, Nigeria. These were used to isolate fungi *A. niger*. Two different soil samples were used (labelled samples A and B). To form the diluent solution (normal saline solution), 0.9 g of sodium chloride was dissolved in 200 mL of distilled water in a beaker. The solution was subjected to shaking to ensure complete dissolution of the salt in water. 90 g of Irish potatoes required the addition of 300 mL of distilled water to make the broth. For soil samples A and B, 2 g of the soil was poured into the bottles with labels: sample A and sample B, respectively. Then 9 mL of normal saline solution was poured into each of the 12 bottles that were subsequently used for cell subculture. The source of nutrient for the microbes (fungi) are the potato broth and sucrose, 6 g of which was dispensed in 300 mL of distilled water using the standard of 20 g of sucrose in 1 L of distilled water 4.5 g of agar was dispensed in 300 mL distilled water using a standard of 15 g of agar in 1 L distilled water. The sucrose solution, agar solution and 0.6 g of chloramphenicol were dispensed in potato broth that has been made up to 300 mL and this combined solution is called potato dextrose agar (PDA). Saline solution and PDA (in a conical flask) were autoclaved at 121°C for 15 min. The content of the autoclaved was then cooled for 15 min. The biosafety environment was then sterilized with 70% w/w ethanol. The biosafety cabinet was then turned on for 5 min to allow UV light to disinfect the hood. The content of the autoclaved samples was transferred to the biosafety cabinet. A Bunsen burner was used to kill any microbes around the petri dishes and the bottles. A stock solution was prepared using 2 g of soil dispensed in 8 mL normal saline solution. The bottles were labeled A, B, C, and D to represent  $10^{-1}$ ,  $10^{-2}$ ,  $10^{-3}$  and  $10^{-4}$  dilutions, respectively. With a syringe of 1 mL, the stock solution was added to the bottle labelled A which contains 9 mL of the normal saline solution to make it up to 10 mL solution. Then, 1 mL of the content of the A bottle was taken and then transferred to the B bottle, and the process was repeated for sample B following serial dilutions [32], [33].

### 6.2.7 Morphology of *Aspergillus niger* (*A. niger*)

*Aspergillus niger* (*A. niger*) is a name coined out of the Latin name *Aspergillum*, which literally means holy water sprinkler due to its appearance under a microscope [34], [35]. It possesses a characteristic black color like a mold [36]. The microstructure reveals that the *A. niger* is filamentous with some hyphae, initially it was white but over time the color changed to black, after some days it produced a conidial spore. The conidiophores produced were emerging from the septate and hyphae and the conidial heads are spherical forming columns of biseriate. Metulea is a cellular subset of conidiophore and its duty is to provide support for the phialides. Hence, the image in Figure 6.1 observed using a Celestron microscope after staining with methyl blue. Hence, this image confirms the presence of *A. niger* as the test organism in the Petri dish.

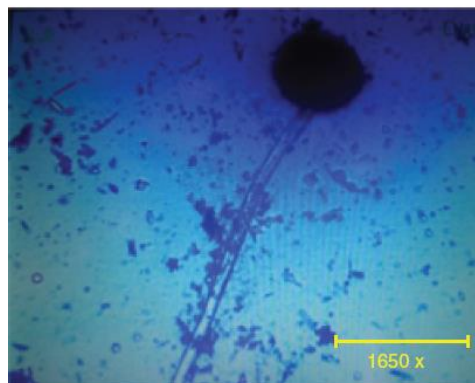


Figure 6.1: Optical micrograph of an *A. niger*

### 6.2.8 Preparation of test organism

The *A. niger* colony that were prepared were stored in bottles that were transferred from the PDA slant to the petri dish at 25°C for 30 min. An 80 µl section of the *A. niger* colonies were dispensed into six different glass petri dishes. After 3 days of growth, the grown *A. niger* spores were harvested using a sterile tween-20 solution (0.05% w/v). They were then added to the PDA in the slanting bottles. The slants were incubated at room temperature (25°C) for 7 days. The harvest was done again using sterile tween-20 solution [37].

### 6.2.8.1 Determination of number of *A. niger* spores

A spore suspension was prepared. Using pipet, ~ 9 µl of the cell suspension was put into the two counting chambers of a haemocytometer. Care was taken to avoid injecting bubbles into the chambers to overfill or under fill the chambers. The spores were counted in each of the four 0.1 mm<sup>3</sup> corner squares, while the spores touching the top or left and or bottom or right borders were not counted [38], [39]. To determine the spore count, the total spores counted in the four corner squares were calculated using the equation:

$$\text{Spores/ml} = (n) \times 10^6 \quad 6.2$$

where n stands for the number of cells per millilitre is the average cell count per square of the four corner squares counted.

### 6.2.8.2 Test of zone of inhibition

The antimicrobial activity exhibited by the antimicrobial agent was checked using the classical zone of inhibition test. 80 µl of the *A. niger* culture was transferred and spread using a sterile cotton bud on the PDA in the petri dish. Then 5 mm diameter antimicrobial films of the three different CA contents were placed in a glass petri dish. The petri dishes were kept at room temperature, 25°C, for 7 days. The growth of the *A. niger* was monitored and the diameter of the clear zone was measured with a calliper at regular intervals after three five and seven days [7], [40], [41].

## 6.3 Modelling antimicrobial release mechanism from films

The Korsmeyer-Peppas model (KPM) (1983) [42] was used to model the Antimicrobial Release from the films. This gives:

$$\frac{m_t}{m_i} = 4 \left( \frac{D}{\pi \delta^2} \right) t^n = kt^n \quad 6.3$$

$$m_t = m_o - m_f \quad 6.4$$

where  $\frac{m_t}{m_i}$  is the release fraction,  $k$  is the geometric constant of the release system,  $n$  is the release exponent which depicts the release mechanism,  $m_i$  is the absolute cumulative amount of PS released at time,  $t$ ,  $m_t$  is the amount of PS remaining in the film at time,  $t$  during drug elution,  $\delta$  is the thickness of the film. From Equation (6.2),  $m_o$  is the mass of the swollen film at equilibrium state prior to PS release,  $m_f$  is the final mass of the film after drug elution, and  $D$  is the diffusion coefficient, the constants  $k$  and  $n$  were obtained from the linear form of Equation (6.1):

$$\ln\left(\frac{m_t}{m_i}\right) = \ln k - n \ln t \quad 6.5$$

where  $\ln(k)$ , represents the intercept and,  $n$ , the slope of the plot,  $\ln(m_t/m_i)$  versus  $\ln(t)$ . The intercepts on the  $\ln(m_t/m_i)$  is equal to  $\ln(k)$ . The diffusion coefficients,  $D_s$ , were obtained from the equation below.

$$D_s = \frac{k\pi\delta^2}{4} \quad 6.6$$

where  $k$  is the geometric constant of the release system,  $\pi$  is the mathematical constant reflecting the ration of a circle circumference to its diameter and  $\delta$  is the thickness of the film [14].

### 6.3.1 Modelling the effect of diffusion from the porous film

Using some form of simple homogenous models possessing effective transport properties the mode of Transport (of fluid) through a porous material can be done. This has become necessary because the pores are usually smaller than the entire domain to be modelled. Assuming the CA film to be a homogenous domain with the structures well detailed, the simplified 3D geometry is as shown below from COMSOL multiphysics a finite analysis software [43], [44] (Figure 6.2). The modelled structure in the diagram above follows a time dependent equation

$$\frac{\partial c}{\partial t} + \nabla \cdot (-D\nabla C) = 0 \quad 6.7$$

In the above equation,  $c$  and  $D$  signifies the concentration (in mol/m<sup>3</sup>) and the diffusion coefficient (in m<sup>2</sup>/s) respectively of the solute CA. The left vertical boundary represents the concentration boundary condition region and it was set in accordance with Equation (6.8).

$$c = c_o \quad 6.8$$

with  $c_o$  denoting any given concentration. The right vertical boundary represents the flux boundary and it was set in accordance with the Equation (6.9)

$$(-D\nabla C) \cdot n = k_m(c - c_1) \quad 6.9$$

where  $k_m$  and  $c_1$  represents the mass transfer coefficient (in m/s) and the concentration in a bulk solution around the porous structure. Other boundaries are meant to be insulating in accordance with Equation (6.8).

$$(-D\nabla c) \cdot n = 0 \quad 6.10$$

At  $x = 0$ , the maximum value is obtained along the abscissa and along the ordinate it is given as  $c = c_o$ .

$$c(t_o) = c_o \exp(-ax^2) \quad 6.11$$

To generate a uniform 1D model geometry having efficient properties of transport and requisite average porosity, the equation boils down to this:

$$\varepsilon \frac{\partial c}{\partial t} + \nabla \cdot (-D^{eff} \nabla c) = 0 \quad 6.12$$

where  $\varepsilon$  and  $D_{eff}$  represents the average porosity and the effective diffusivity respectively. These results are obtained by calculation from the solutions to the detailed structure. The result shows a time dependent simulation that runs from 0 to 52 hr as shown below (Figure 6.3).

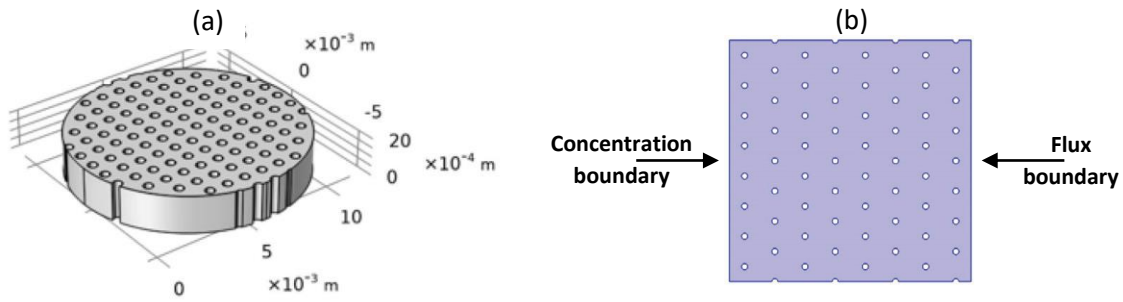


Figure 6.2: (a) 3D CA porous structure with the gray colored portion as the surface that is accessible for diffusion. (b) 2D porous structure representing a segment of the surface of (a)

### 6.3.2 Summary of the simulation

For the 2D simulation, the concentration has almost reached steady state after 72 min. To calculate the flux, we need to integrate over the flux boundary and then divide by its length,  $L_0$ , and this boils down to the equation below [43], [44].

$$N_{\text{average}} = \frac{1}{L_0} \int_0^{L_0} k_m (c - c_1) dS \quad 6.13$$

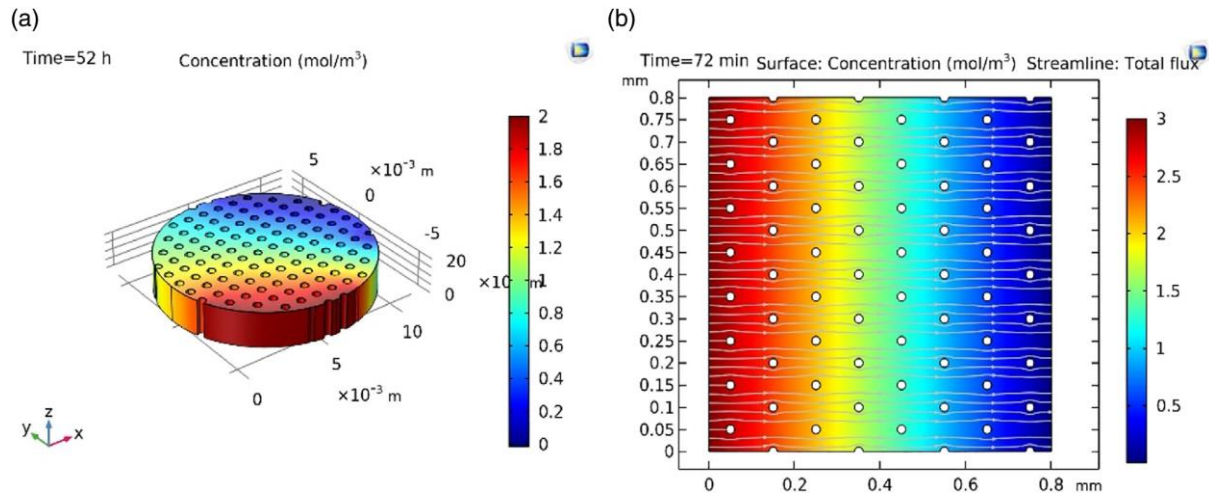


Figure 6.3: (a) Concentration flux in the 3D modelled CA porous film after 52 hr. (b) Surface concentration flux of a segment of the entire CA film in 2D after 72 min

If the simulation is allowed to reach a steady state, then the average flux can be computed. The profile of diffusion of the PS through the film follows a linear trend; hence, the porous 2D film can be replaced with a 1D film that is homogenous along the abscissa therefore calculating the effective diffusion becomes feasible using the formula shown below.

$$D_{\text{eff}} \frac{(c_0 - c_{\text{out}})}{L_1} = N_{\text{average}} \quad 6.14$$

The average concentration in (mol/m<sup>3</sup>) and the geometry length along the abscissa are represented by  $c_{\text{out}}$  and  $L_1$  respectively. To calculate the average concentration then the equation below was integrated

$$C_{\text{out}} = \frac{1}{L_0} \int_0^{L_0} c dy$$

6.15

From the result above the effective diffusivity was obtained using the equation

$$D^{\text{eff}} = \frac{N_{\text{average}} \times L_1}{C_0 - C_{\text{out}}} \quad 6.16$$

The above result is the effective diffusivity and this can be compared to the free diffusivity that has been given in COMSOL as D1. The relationship between the effective diffusivity and “free” diffusivity is based on this equation:

$$D^{\text{eff}} = D \frac{\varepsilon}{\tau} \quad 6.17$$

Hence, the porosity of the film and the tortuosity is represented as  $\varepsilon$  and  $\tau$  respectively. The tortuosity represents the actual length per unit effective length a molecule of PS has to diffuse in a porous structure. The porosity can be obtained by solving the integral below.

$$\varepsilon = \frac{1}{L_0 L_1} \int_0^{L_1} \int_0^{L_0} 1 dx dy \quad 6.18$$

The variables have their usual meanings. The resulting permittivity and the tortuosity were calculated. Furthermore, expressing tortuosity as a power of the porosity has led to the formula for effective diffusivity as shown below.

$$D^{\text{eff}} = D \varepsilon^\rho \quad 6.19$$

The calculated value for porosity is 1.60 which is very close to the experimental value for most porous material ranging from 1.5 to 2. Hence, we can leverage on the effective

diffusivity to model a homogenous 1D model with value that can be compared to the 2D model [43]. The diagram below shows the graph figure 6.4.

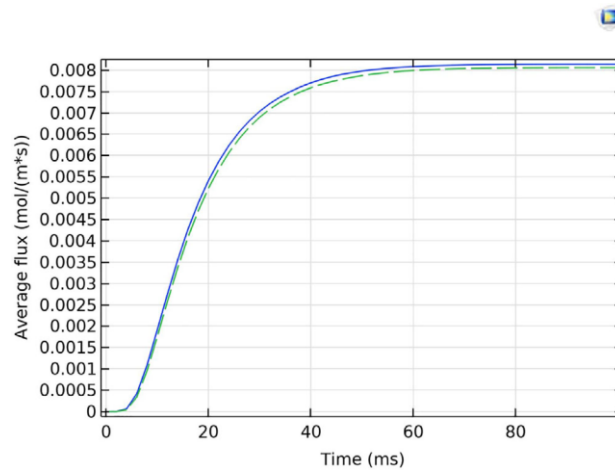


Figure 6.4: Generalized average flux at the flux boundary in the detailed 2D model (solid blue line) and the 1D homogenized approximation (dashed green line)

## 6.4 Result and Discussion

### 6.4.1 Film Microstructure and Morphology

The results of the scanning electron microscopy analyses are presented in figure 6.5. The SEM of the cross-section of single layer CA film with 2,300  $\mu\text{m}$  thickness were determined after complete drying at room temperature (25°C). Increasing the concentration of CA in the film (from 10 wt% to 13 wt% and 15 wt%) leads to the formation of dense films with decreasing porosity, as the amount of polymer in the films increases. Films without antimicrobial agent

had increasing pore sizes with increasing polymer content in the polymer film. As the antimicrobial film dries up, the crystalline nature of the PS was revealed, as shown in figure 6.5. Further drying of the antimicrobial film resulted in increasing PS concentration in the

porous structures Figure 6.5b–d. Drying the antimicrobial film at a higher temperature of 100°C resulted in even higher levels of porosity. Hence, the amount of crystals formed in a film depends on the porosity of the films. The pore sizes also increase with increasing cellulose: acetate ratio (Figure 6.5a–d).

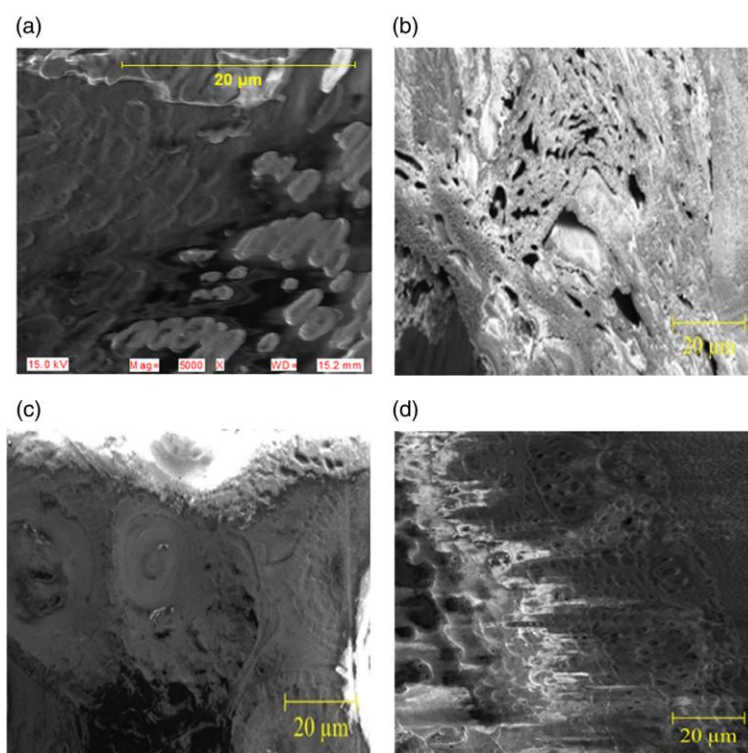


Figure 6.5: Effect of cellulose acetate ratio on the pore sizes: (a) crystals of antimicrobial film, (b) 10%w/w Composition of CA, (c) 13%w/w Composition of CA and (d) 15%w/w Composition of CA

#### 6.4.2 Potassium sorbate release

Upon the dissolution of 2 wt% of potassium sorbate in distilled water, the peak absorbance of 2.992 au was obtained via UV–vis at a wavelength of 252.0 nm. Similarly, the peak absorbance of the three other film samples were, 2.644 au, 1.271 au, and 2.084 au for films  $M_{15}^+$ ,  $M_{13}^+$  and  $M_{10}^+$ , respectively. Similar plots were obtained for the other days (Figure 6.6).

The standard curve for PS release (obtained on a daily basis) was obtained for the period corresponding to the incubation of antimicrobial film in distilled water. The presence of potassium sorbate was observed on the samples for the three film samples. The standard

curve revealed a constant absorptivity ( $214.85 \text{ au}\cdot\text{dm}^3/\text{mol}$ ) of PS, irrespective of the type of film. Furthermore, after 10 days, the percentage/cumulative release of PS from the films was  $\sim 64$  to  $66\%$ .

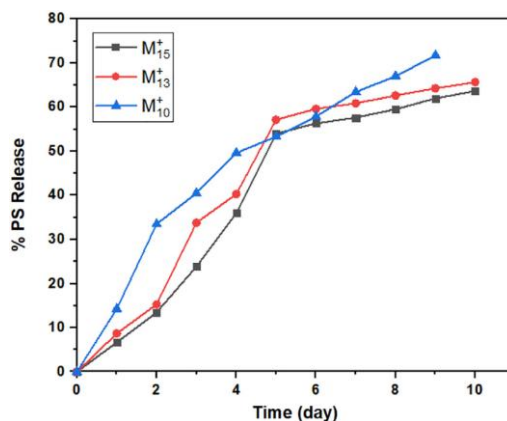


Figure 6.6: Percentage release of potassium sorbate (PS) from 15 w/w% CA, 13 w/w% CA, and 10 w/w% CA

This gives a concentration range of  $0.00787\text{--}0.00831 \text{ mol}\cdot\text{dm}^{-3}$  of PS over a period of 10 days of release [14], [40]. Plots of  $\ln\left(\frac{M_t}{M_i}\right)$  versus  $\ln(t)$  are presented in Figure 6.7a–d, for different film types having antimicrobial agent added to it at room temperature and at  $37^\circ\text{C}$ , the slope of each of these graphs is equivalent to the fluid release exponent,  $n$ , as in Equations (6.1) and (3.3) which in addition to the geometry determines the method of eluting the PS from the CA film to the microbial environment. The graph of the cumulative drug release has also been represented as the percentage PS release with both having the same trend for the different films in Figure 6.7. The release profile shows that the lower the concentration of CA in the film the higher the rate of diffusion of the PS from film hence, film code  $M_{15}^+$  has the lowest release whereas  $M_{10}^+$  has the highest release profile. KMP model validates the linear relationship between the natural logarithm of  $\frac{M_t}{M_i}$  and the natural logarithm of time. This implies that the rate of release of the antimicrobial film will either increase or decrease with time depending on the graph. The data obtained from the weight loss experiments were used to calculate the diffusion coefficients, the PS release exponents, and the geometric constants

of the films. The results are presented in Table 6.2. In most cases, the release exponents are consistent with an anomalous release, with  $n$  values that deviate from 0.5. However, in the case of the  $M_{15}^+$  film, the  $n$  value of 0.5 corresponds to a controlled diffusion mechanism at 37°C. In other cases, super-case II anomalous transport mechanisms were observed with  $n$  values greater than 0.50.

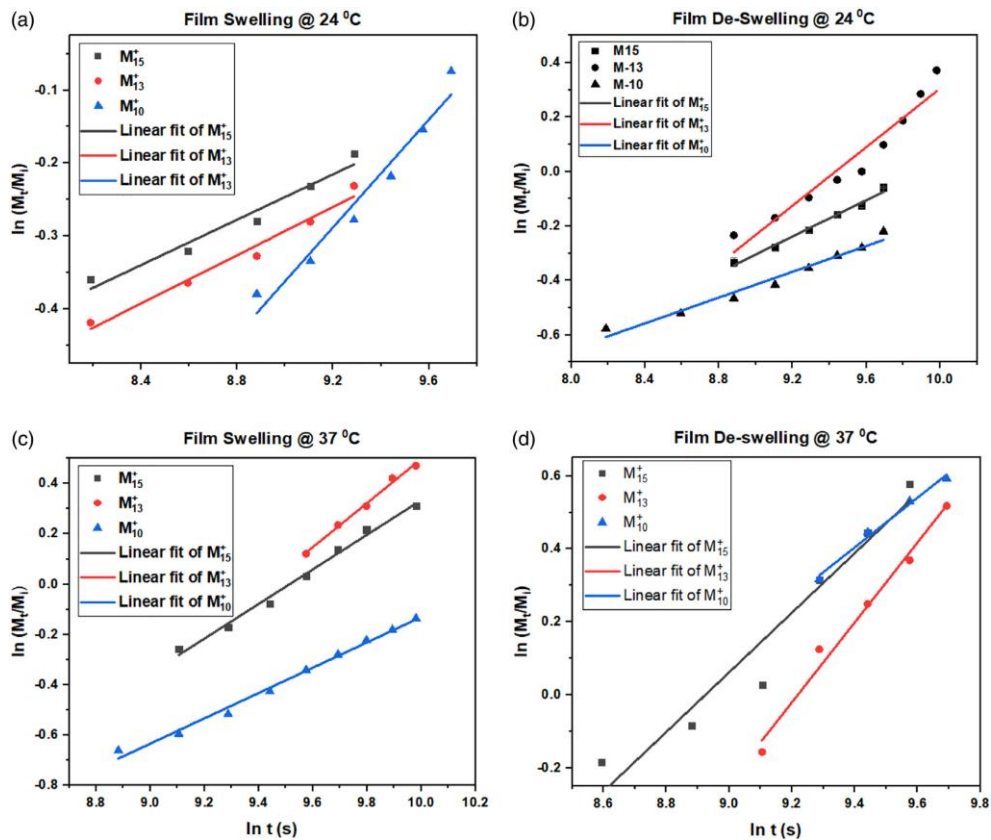


Figure 6.7: (a) and (b) Presents linear fit plot of  $\ln\left(\frac{M_t}{M_i}\right)$  versus  $\ln(t)$ , for swelling and de-swelling of antimicrobial film samples,  $M_{15}^+$ ,  $M_{13}^+$  and  $M_{10}^+$  respectively having antimicrobial agent added to it at room temperature 24°C, whereas, (c) and (d) was added at 37°C

Table 6.2: (a) The values of the swelling and de-swelling ratios and the  $k$ ,  $n$ , and  $D$  values of the antimicrobial films at room temperature 24°C. (b) The values of the swelling and de-swelling ratios and the  $k$ ,  $n$ , and  $D$  values of the antimicrobial films at room temperature 37°C

(a)					
Film samples	Film ~ thickness ( $\delta$ ) in mm	Geometric constant ( $k$ )	Fluid release exponent ( $n$ )	Diffusion coefficient ( $D$ ) ( $m^2s^{-1}$ )	Equilibrium swelling ratio ( $SR_{eq}$ )
$M_{15}^+$	2	0.19	0.16	$7.33 \times 10^{-7}$	1.42
$M_{13}^+$	2	0.17	0.17	$5.29 \times 10^{-7}$	1.41
$M_{10}^+$	2	0.025	0.37	$7.87 \times 10^{-8}$	1.12
$M_{15}^-$	2	0.037	0.33	$1.16 \times 10^{-7}$	1.52
$M_{13}^-$	2	0.0063	0.54	$1.97 \times 10^{-8}$	1.47
$M_{10}^-$	2	0.078	0.24	$2.46 \times 10^{-7}$	1.07
(b)					
Film samples	Film ~ thickness ( $\delta$ ) in mm	Geometric constant ( $k$ )	Fluid release exponent ( $n$ )	Diffusion coefficient ( $D$ ) ( $m^2s^{-1}$ )	Equilibrium swelling ratio ( $SR_{eq}$ )
$M_{15}^+$	2	0.0014	0.69	$4.52 \times 10^{-10}$	1.19
$M_{13}^+$	2	0.00026	0.88	$8.12 \times 10^{-10}$	1.40
$M_{10}^+$	2	0.0057	0.50	$1.80 \times 10^{-8}$	0.71
$M_{15}^-$	2	0.00068	0.82	$2.15 \times 10^{-9}$	1.68
$M_{13}^-$	2	0.0025	0.68	$7.85 \times 10^{-9}$	1.28
$M_{10}^-$	2	0.000041	1.10	$1.30 \times 10^{-10}$	0.96

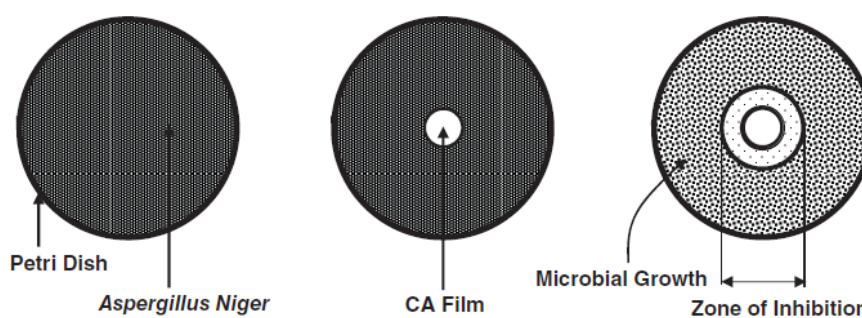


Figure 6.8: Zone of inhibition of CA film by the agar diffusion method [45]–[47]

between the natural logarithm of  $\frac{M_t}{M_i}$  and the natural logarithm of time. This implies that the rate of release of the antimicrobial film will either increase or decrease with time depending on the graph. The data obtained from the weight loss experiments were used to calculate the diffusion coefficients, the PS release exponents, and the geometric constants of the films. The results are presented in Table 6.2. In most cases, the release exponents are consistent with an anomalous release, with  $n$  values that deviate from 0.5. However, in the case of the  $M_{10}^+$ , the  $n$  value of 0.5 corresponds to a controlled diffusion mechanism at 24°C. In other cases, super-case II anomalous transport mechanisms were observed with  $n$  values greater than 0.50.

### 6.4.3 Antimicrobial effects

The restraining effects of the antimicrobial agent on the growth of *A. niger* was experimentally determined for antimicrobial agents containing 15 wt%, 13 wt%, and 10 wt% CA using the agar diffusion method which is synonymous with the endpoint method [28], [45]–[48]. After 7 days, there was no visible zone of inhibition with antimicrobial film that contained 2 wt% of CA. Further increase in the concentration of PS to 20 wt% resulted in a visible clear zone around the antimicrobial film. The rate of diffusion of PS through the PDA, results in a concentration gradient that is inversely proportional to the distance from the wall of the petri dish [28], [49]. The extent of inhibition is evident by the radius around the CA/PS film without the growth of *A. niger* and this is a function of the rate of diffusion of PS into the *A. niger*. The measured diameters of the visible clear zones of inhibition obtained from Vernier calipers measurements were: ~60 mm, ~65 mm and ~50 mm for films  $M_{15}^+$ ,  $M_{13}^+$  and  $M_{10}^+$ , respectively. After 4 days the zones were observed to be ~30 mm, ~35mm and ~45 mm, for samples  $M_{15}^+$ ,  $M_{13}^+$  and  $M_{10}^+$ , respectively. This suggests that the diffusion of PS to the agar medium (in the petri dishes) decreased with time and it also shows that the rate of diffusion of PS from the film is inversely proportional to film thickness. Hence, the lesser the concentration of CA in the film the higher the rate of diffusion of PS from the film to the *A. niger* in the petri dish. The antimicrobial films containing 2 wt% potassium sorbate (PS) was able to restrain the growth of the target microorganism, *A. niger*, in peanut and bread, with gradual increment in the amount of PS to 20 wt%, furthermore, the growth of *A. niger* was prevented (visible zone of inhibition) for about 8 days in the presence of PS as in Figure 6.8. Incorporating PS in linear low density polyethylene film (0.4 mm thick) lowered the growth rate of yeast and prolonged the lag period before mold growth became evident [50]–[53].

### 6.5 Implication

The above results suggest that the controlled release of PS from antimicrobial packaging has the potential to reduce the growth of *A. niger* in packaged foods such as bread and peanuts. Such inhibition also has the potential to improve the lifespans of packaged foods in ways that could be engineered through the control of the release kinetics. Thus, the improved understanding of the release kinetics can be used to guide the design of packaging materials in which the polymer films can be used to encapsulate PS and other active materials that can be released to prevent microbial growth and prolong the lifespans of packaged foods. Such understanding of controlled release can be used to guide the development of smart packaging that contains multiple active components that can be released in stages to prolong the lifetimes of packaged foods. Furthermore, in the case of packaged foods such as bread and peanuts, smart packaging can be used to prolong the lifetimes of agricultural products that are produced largely in rural areas, where almost half of the foods (fruits and vegetables) that are produced are lost between the farm and the market [15], [54], [55]. Further work is needed to develop the manufacturing processes for the application of the polymer films to plastic packages. There is also a need for further studies to determine the lifetimes of packaging materials in which different concentrations of antimicrobials are used to inhibit the growth of microbes in different types of packaged foods [56]. It is anticipated that such packaging may also contain embedded sensors [56], [57] that could detect biochemical signals that may provide the opportunity to develop the next generation of smart packaging materials for food preservation. These are clearly the challenges and opportunities for future work.

## 6.6 Bibliography

- [1] L. H. Villalobos-Delgado, G. V. Nevárez-Moorillon, I. Caro, E. J. Quinto, and J. Mateo, *Natural antimicrobial agents to improve foods shelf life*. Elsevier Inc., 2019.
- [2] E. J. Quinto, I. Caro, L. H. Villalobos-Delgado, J. Mateo, B. De-Mateo-silleras, and M. P. Redondo-Del-río, “Food safety through natural antimicrobials,” *Antibiotics*, vol. 8, no. 4, pp. 1–30, 2019, doi: 10.3390/antibiotics8040208.
- [3] U. De Corato, “Improving the shelf-life and quality of fresh and minimally-processed fruits and vegetables for a modern food industry: A comprehensive critical review from the traditional technologies into the most promising advancements,” *Crit. Rev. Food Sci. Nutr.*, vol. 60, no. 6, pp. 940–975, 2020, doi: 10.1080/10408398.2018.1553025.
- [4] I. Kim, K. Viswanathan, G. Kasi, S. Thanakkasaranee, K. Sadeghi, and J. Seo, “ZnO Nanostructures in Active Antibacterial Food Packaging: Preparation Methods, Antimicrobial Mechanisms, Safety Issues, Future Prospects, and Challenges,” *Food Rev. Int.*, vol. 00, no. 00, pp. 1–29, 2020, doi: 10.1080/87559129.2020.1737709.
- [5] A. L. Brody, E. R. Strupinsky, and L. R. Kline, *Active packaging for food application*. New York,: Tehnomic Publishing, 2001.
- [6] M. Felix de Andrade *et al.*, “A study of poly (butylene adipate-co-terephthalate)/orange essential oil films for application in active antimicrobial packaging,” *Lwt*, vol. 125, p. 109148, 2020, doi: 10.1016/j.lwt.2020.109148.
- [7] S. Gemili, A. Yemenicioğlu, and S. A. Altinkaya, “Development of antioxidant food packaging materials with controlled release properties,” *J. Food Eng.*, vol. 96, no. 3, pp. 325–332, 2010, doi: 10.1016/j.jfoodeng.2009.08.020.
- [8] J. Gustavsson, C. Cederberg, U. Sonesson, and A. Emanuelsson, *The methodology of the FAO study: “ Global Food Losses and Food Waste - extent , causes and prevention ” - FAO , 2011*, vol. SIK report, no. 857. 2013.
- [9] S. Corrado *et al.*, “Food waste accounting methodologies: Challenges, opportunities, and further advancements,” *Glob. Food Sec.*, vol. 20, pp. 93–100, 2019, doi:

- 10.1016/j.gfs.2019.01.002.
- [10] B. Lipinski, C. Hanson, J. Lomax, L. Kitinoja, R. Waite, and T. Searchinger, "Reducing food loss and waste," *Science (80-. )*, vol. 352, no. 6284, pp. 424–426, 2016, doi: 10.1126/science.352.6284.424-p.
- [11] A. K. Biswal and S. Saha, "Colloids and Surfaces B : Biointerfaces Prolonging food shelf-life by dual actives release from multi-layered polymer particles," *Colloids Surfaces B Biointerfaces*, vol. 175, no. November 2018, pp. 281–290, 2019, doi: 10.1016/j.colsurfb.2018.12.004.
- [12] A. M. Khaneghah, S. Mohammad, B. Hashemi, and S. Limbo, "Antimicrobial agents and packaging systems in antimicrobial active food packaging: an overview of approaches and interactions," *Food Bioprod. Process.*, vol. 111, pp. 1–19, 2018, doi: 10.1016/j.fbp.2018.05.001.
- [13] Y. R. Corrales-Ureña *et al.*, "Functionalization of hydrophobic surfaces with antimicrobial peptides immobilized on a bio-interfactant layer," *RSC Adv.*, vol. 10, no. 1, pp. 376–386, 2019, doi: 10.1039/c9ra07380a.
- [14] Y. Danyuo *et al.*, "Swelling of poly(N-isopropylacrylamide) P(NIPA)-based hydrogels with bacterial-synthesized prodigiosin for localized cancer drug delivery," *Mater. Sci. Eng. C*, vol. 59, pp. 19–29, 2016, doi: 10.1016/j.msec.2015.09.090.
- [15] Dana Gunders and N. R. D. Council, "Wasted: How America is losing up to 40 percent of its food from farm to fork to landfill," *NRDC Issue Pap.*, no. August, pp. 1–26, 2015.
- [16] A. Conte, G. G. Buonocore, A. Bevilacqua, M. Sinigaglia, and M. A. Del Nobile, "Immobilization of lysozyme on polyvinylalcohol films for active packaging applications," *J. Food Prot.*, vol. 69, no. 4, pp. 866–870, 2006, doi: 10.4315/0362-028X-69.4.866.
- [17] J. C. Oliveira, F. A. R. Oliveira, and L. G. M. Gorris, "Process Optimisation and Minimal Processing of Foods European Commission COPERNICUS PROGRAMME Concerted action CIPA-CT94-0195 Volume 5: Minimal and Combined Processes," in *Minimal and Combined Processes*, 1998, p. 180.
- [18] B. Ouattara, R. E. Simard, G. Piette, A. Bégin, and R. A. Holley, "Diffusion of acetic and propionic acids from chitosan-based antimicrobial packaging films," *J. Food Sci.*, vol. 65, no. 5, pp. 768–773, 2000, doi: 10.1111/j.1365-2621.2000.tb13584.x.
- [19] Y. M. Weng, M. J. Chen, and W. Chen, "Benzoyl chloride modified ionomer films as antimicrobial food packaging materials," *Int. J. Food Sci. Technol.*, vol. 32, no. 3, pp. 229–234, 1997, doi: 10.1046/j.1365-2621.1997.00397.x.
- [20] N. Halonen *et al.*, "Bio-Based Smart Materials for Food Packaging and Sensors – A Review," *Front. Mater.*, vol. 7, no. April, pp. 1–14, 2020, doi: 10.3389/fmats.2020.00082.
- [21] B. Kuswandi and Jumina, "Active and intelligent packaging, safety, and quality controls," *Fresh-Cut Fruits Veg.*, pp. 243–294, 2020, doi: 10.1016/b978-0-12-816184-5.00012-4.
- [22] C. Vilela, C. Moreirinha, E. M. Domingues, F. M. L. Figueiredo, A. Almeida, and C. S. R. Freire, "Antimicrobial and conductive nanocellulose-based films for active and intelligent food packaging," *Nanomaterials*, vol. 9, no. 7, pp. 1–16, 2019, doi: 10.3390/nano9070980.
- [23] A. M. El Nahrawy, A. B. A. Hammad, A. M. Youssef, A. M. Mansour, and A. M. Othman, "Thermal, dielectric and antimicrobial properties of polystyrene-assisted/ITO:Cu nanocomposites," *Appl. Phys. A Mater. Sci. Process.*, vol. 125, no. 1, p. 0, 2019, doi: 10.1007/s00339-018-2351-5.
- [24] Y. Xia *et al.*, "Materials Science & Engineering C Doxorubicin-loaded functionalized

- selenium nanoparticles for enhanced antitumor efficacy in cervical carcinoma therapy,” *Mater. Sci. Eng. C*, vol. 106, no. 318, p. 110100, 2020, doi: 10.1016/j.msec.2019.110100.
- [25] T. Sawa, K. Kooguchi, and K. Moriyama, “Molecular diversity of extended-spectrum  $\beta$ -lactamases and carbapenemases, and antimicrobial resistance,” *J. Intensive Care*, vol. 8, no. 1, pp. 1–13, 2020, doi: 10.1186/s40560-020-0429-6.
- [26] M. Xu *et al.*, “Single-step fabrication of catechol- $\epsilon$ -poly-L-lysine antimicrobial paint that prevents superbug infection and promotes osteoconductivity of titanium implants,” *Chem. Eng. J.*, vol. 396, p. 125240, 2020, doi: 10.1016/j.cej.2020.125240.
- [27] P. K. Dutta, S. Tripathi, G. K. Mehrotra, and J. Dutta, “Perspectives for chitosan based antimicrobial films in food applications,” *Food Chem.*, vol. 114, no. 4, pp. 1173–1182, 2009, doi: 10.1016/j.foodchem.2008.11.047.
- [28] J. Micheal Davidson, J. S. Sofos, and A. L. Branen, *Antimicrobials in Food*, 3rd Editio. Boca Raton: CRC Press, 2005.
- [29] J. N. Sofos, “Challenges to meat safety in the 21st century,” *Meat Sci.*, vol. 78, no. 1–2, pp. 3–13, 2008, doi: 10.1016/j.meatsci.2007.07.027.
- [30] B. Malhotra, A. Keshwani, and H. Kharkwal, “Antimicrobial food packaging: Potential and pitfalls,” *Front. Microbiol.*, vol. 6, no. JUN, pp. 1–9, 2015, doi: 10.3389/fmicb.2015.00611.
- [31] M. S. Arshad and S. A. Batool, “Natural Antimicrobials, their Sources and Food Safety,” *Food Addit.*, 2017, doi: 10.5772/intechopen.70197.
- [32] V. L. de de Farias, K. X. Monteiro, S. Rodrigues, F. A. N. Fernandes, and G. A. S. Pinto, “Comparison of aspergillus niger spore production on potato dextrose agar (PDA) and crushed corncob medium,” *J. Gen. Appl. Microbiol.*, vol. 56, no. 5, pp. 399–402, 2010, doi: 10.2323/jgam.56.399.
- [33] G. Weststeijn and N. Okafor, “Comparison of cassava, yam and potato dextrose agars as fungal culture media,” *Netherlands J. Plant Pathol.*, vol. 77, no. 4, pp. 134–139, 1971, doi: 10.1007/BF02000553.
- [34] S. E. Baker, “Aspergillus niger genomics: Past, present and into the future,” *Med. Mycol.*, vol. 44, no. SUPPL. 1, pp. 17–21, 2006, doi: 10.1080/13693780600921037.
- [35] E. Schuster, N. Dunn-Coleman, J. Frisvad, and P. Van Dijck, “On the safety of Aspergillus niger - A review,” *Appl. Microbiol. Biotechnol.*, vol. 59, no. 4–5, pp. 426–435, 2002, doi: 10.1007/s00253-002-1032-6.
- [36] G. S. Mishra, N. Mehta, and M. Pal, “Chronic bilateral otomycosis caused by Aspergillus niger,” *Mycoses*, vol. 47, no. 1–2, pp. 82–84, 2004, doi: 10.1046/j.0933-7407.2003.00935.x.
- [37] D. C. Martens, G. Chesters, and J. T. Murdock, “Available Zinc Status of Wisconsin Soils as Determined by Aspergillus niger 1,” *Agron. J.*, vol. 56, no. 3, pp. 262–265, 1964, doi: 10.2134/agronj1964.00021962005600030004x.
- [38] M. Plascencia-Jatomea, G. Viniegra, R. Olayo, M. M. Castillo-Ortega, and K. Shirai, “Effect of Chitosan and Temperature on Spore Germination of Aspergillus niger,” *Macromol. Biosci.*, vol. 3, no. 10, pp. 582–586, 2003, doi: 10.1002/mabi.200350024.
- [39] A. Wargenau and A. Kwade, “Determination of adhesion between single Aspergillus niger spores in aqueous solutions using an atomic force microscope,” *Langmuir*, vol. 26, no. 13, pp. 11071–11076, 2010, doi: 10.1021/la100653c.
- [40] P. Appendini and J. H. Hotchkiss, “Review of antimicrobial food packaging,” *Elsevier, Innov. food Sci. Eng. Technol.*, vol. 40, no. 3, pp. 113–126, 2009, doi: [https://doi.org/10.1016/S1466-8564\(02\)00012-7](https://doi.org/10.1016/S1466-8564(02)00012-7).
- [41] B. H. Ericsson, G. Tunevall, and K. Wickman, “The paper disc method for determination of bacterial sensitivity to antibiotics: Relationship between the diameter

- of the zone of inhibition and the minimum inhibitory concentration,” *Scand. J. Clin. Lab. Invest.*, vol. 12, no. 4, pp. 414–422, 1960, doi: 10.3109/00365516009065406.
- [42] S. Dash, P. N. Murthy, L. Nath, and P. Chowdhury, “Kinetic modeling on drug release from controlled drug delivery systems,” *Acta Pol. Pharm. - Drug Res.*, vol. 67, no. 3, pp. 217–223, 2010.
- [43] S. Aderyani, S. A. Shah, A. Masoudi, M. J. Green, J. L. Lutkenhaus, and H. Ardebili, “Comparison of Nanoarchitecture to Porous Media Diffusion Models in Reduced Graphene Oxide/Aramid Nanofiber Electrodes for Supercapacitors,” *ACS Nano*, vol. 14, no. 5, pp. 5314–5323, 2020, doi: 10.1021/acsnano.9b07116.
- [44] C. Kumar, G. J. Millar, and M. A. Karim, “Effective Diffusivity and Evaporative Cooling in Convective Drying of Food Material,” *Dry. Technol.*, vol. 33, no. 2, pp. 227–237, 2015, doi: 10.1080/07373937.2014.947512.
- [45] F. W. Goldstein, J. C. Chumpitaz, J. M. Guevara, B. Papadopoulou, J. F. Acar, and J. F. Vieu, “Plasmid-mediated resistance to multiple antibiotics in salmonella typhi,” *J. Infect. Dis.*, vol. 153, no. 2, pp. 261–265, 1986, doi: 10.1093/infdis/153.2.261.
- [46] L. J. V. Piddock, “Techniques used for the determination of antimicrobial resistance and sensitivity in bacteria,” *J. Appl. Bacteriol.*, vol. 68, no. 4, pp. 307–318, 1990, doi: 10.1111/j.1365-2672.1990.tb02880.x.
- [47] E. W. Tiemersma *et al.*, “Methicillin-resistant staphylococcus aureus in Europe, 1999–2002,” *Emerg. Infect. Dis.*, vol. 10, no. 9, pp. 1627–1634, 2004, doi: 10.3201/eid1009.040069.
- [48] A. J. Evans, “Treatment effects in prostate cancer,” *Mod. Pathol.*, vol. 31, pp. 110–121, 2018, doi: 10.1038/modpathol.2017.158.
- [49] R. Woodford and B. W. Barry, “Penetration enhancers and the percutaneous absorption of drugs: An update,” *Cutan. Ocul. Toxicol.*, vol. 5, no. 3, pp. 167–177, 1986, doi: 10.3109/15569528609030991.
- [50] P. Cazón, G. Velazquez, and M. Vázquez, “Novel composite films from regenerated cellulose-glycerol-polyvinyl alcohol: Mechanical and barrier properties,” *Food Hydrocoll.*, vol. 89, pp. 481–491, 2019, doi: 10.1016/j.foodhyd.2018.11.012.
- [51] J. H. Han and J. D. Floros, “Casting antimicrobial packaging films and measuring their physical properties and antimicrobial activity,” *J. Plast. Film Sheeting*, vol. 13, no. 4, pp. 287–298, 1997, doi: 10.1177/875608799701300405.
- [52] N. Kuplennik, R. Tchoudakov, Z. Ben-Barak Zelas, A. Sadovski, A. Fishman, and M. Narkis, “Antimicrobial packaging based on linear low-density polyethylene compounded with potassium sorbate,” *LWT - Food Sci. Technol.*, vol. 62, no. 1, pp. 278–286, 2015, doi: 10.1016/j.lwt.2015.01.002.
- [53] N. Samsalee and R. Sothornvit, “Development and characterization of porcine plasma protein-chitosan blended films,” *Food Packag. Shelf Life*, vol. 22, no. April 2018, p. 100406, 2019, doi: 10.1016/j.fpsl.2019.100406.
- [54] J. Johnston, A. Biro, and N. MacKendrick, “Lost in the supermarket: The corporate-organic foodscape and the struggle for food democracy,” *Antipode*, vol. 41, no. 3, pp. 509–532, 2009, doi: 10.1111/j.1467-8330.2009.00685.x.
- [55] M. Kumm, H. de Moel, M. Porkka, S. Siebert, O. Varis, and P. J. Ward, “Lost food, wasted resources: Global food supply chain losses and their impacts on freshwater, cropland, and fertiliser use,” *Sci. Total Environ.*, vol. 438, pp. 477–489, 2012, doi: 10.1016/j.scitotenv.2012.08.092.
- [56] H. Yousefi, H. M. Su, S. M. Imani, K. Alkhalidi, C. D. Filipe, and T. F. Didar, “Intelligent Food Packaging: A Review of Smart Sensing Technologies for Monitoring Food Quality,” *ACS Sensors*, vol. 4, no. 4, pp. 808–821, 2019, doi: 10.1021/acssensors.9b00440.

- [57] D. Schaefer and W. M. Cheung, “Smart Packaging: Opportunities and Challenges,” *Procedia CIRP*, vol. 72, pp. 1022–1027, 2018, doi: 10.1016/j.procir.2018.03.240.

## CHAPTER SEVEN

### 7.0 Perspectives and conclusions

The development of methods for targeted prostate cancer drug delivery, in particular, was the main emphasis of this dissertation's study coupled with the development of antimicrobial cellulose acetate polymer for food preservation. The first and the second project results mostly illustrated the importance of nanoparticle drug delivery formulations to achieve regulated drug release for prostate cancer treatment and on the other, the third project looks at the materials science approach to the effect of antimicrobial drug delivery on the foodstuff to prolong the shelf life of packaged food. The first, second and the third projects were conducted based on the following steps, and the materials difficulties related to localized drug release and food shelf life longevity have been clarified.

We presented the results for the synthesis of mesoporous silica nanoparticles, loading the pores of the nanoparticle with a prostate cancer drug (doxorubicin) that has been conjugated with the overexpressed molecular recognition unit (AMACR) on the surface of prostate cancer cells/tissues to ensure targeted drug delivery. Furthermore, the nanoparticle pores were reduced by loading it with a polymer (dextran) thereby sustaining the release of the bare and the conjugated drug *in vitro* on PC-3 cells over a prolonged period of time (Chapters 2 and 3). The drug release kinetics and the thermodynamic parameters were also determined. In addition, the mechanism of diffusion was also elucidated. The effect of the conjugated drug on the tumor injected on some athymic nude male mice were potent enough to shrink the PC-3 tumors *in vivo* and it was discovered that the conjugated drug was more effective in shrinking the tumor *in vivo* than the unconjugated ones. *In vitro* the conjugated drug also reduced the cell viability of the prostate cancer cells more than the unconjugated drug.

In the third project, antimicrobial agent (potassium sorbate) was added to a polymer (cellulose acetate) and a disc was made out of the antimicrobial polymer formed. The swelling and deswelling ratios of the antimicrobial polymer was determined. The drug release kinetics was gotten from the antimicrobial disc. *Aspergillus Niger*, a fungus that was isolated from a soil sample, served as the test microorganism in this experiment. The effect of loading cellulose acetate with the antimicrobial agent was elucidated and over a prolonged period of time (two years) it was still effective.

## **7.1 Recommendations for future work**

### **7.1.1 Application of AMACR conjugated doxorubicin to treat colon cancer**

The peroxisomal oxidation of branched-chain fatty acids from red meat and dairy products is significantly aided by an enzyme called -methylacyl CoA racemase (AMACR), also known as P504S [1]. Immunohistochemical analysis was used in an investigation to examine the

expression of AMACR in 242 instances of colonic malignancies, including 176 colorectal carcinomas, 38 colon adenomas, and 28 hyperplastic (non-neoplastic) polyps [1]. Real-time PCR was used to measure the messenger ribonucleic acid (mRNA) levels of AMACR expression in normal and colon cancer tissues. Real-time PCR was used to measure the mRNA levels of AMACR expression in healthy and colon cancer-related tissues. When compared to normal tissue, colon cancers were shown to have a significant up-regulation of AMACR mRNA. The expression of the AMACR protein was very low or absent in the normal colon, while it was substantially expressed in 76 and 75%, respectively, of well and moderately differentiated colon carcinomas as well as in 79% of adenomas. Only 4% of hyperplastic polyps, in contrast, exhibited AMACR [1]. So, for future research, doxorubicin conjugated to AMACR might be a powerful treatment to target the overexpressed biomarker on the surface of colon cancer.

### **7.1.2 Application of AMACR conjugated doxorubicin to treat glioblastoma**

In glioblastoma, AMACR protein and mRNA levels were markedly increased. Cell proliferation was reduced by AMACR downregulation. The amount of AMACR expression was shown to be linked with the clinical outcome of glioma patients after thorough examination of the public REMBRANDT GBM dataset. As a result of these findings, which show that AMACR expression is elevated in a glioblastoma cell line and glioma patients, AMACR may be a viable diagnostic marker and therapeutic target for cancer, including glioma [2]. Hence, conjugating doxorubicin with AMACR could be helpful in targeting the overexpressed AMACR biomarker on the surface of glioblastoma in vitro and in vivo.

Hence, the enzyme  $\alpha$ -methylacyl CoA racemase (AMACR) is involved in the metabolism of branched-chain fatty acids and has been identified as a promising therapeutic target for prostate cancer, colon cancer and glioblastoma. Some of the ligands employed could include small compounds, peptides, antibodies, and aptamers; each having a unique affinity for

cellular receptor proteins, cancer-specific antigens, enzymes, and nucleic acids. Further research can help in the selection of ligands that are specifically directed against cancer, and it might also serve as inspiration for the ongoing development of novel conjugation techniques in various cellular and animal models.

### **7.1.3 Application of polymer based antimicrobial agent in food preservation**

Since pathogen/microbial infection is one of the biggest risks to human health, there has been an increase in the demand for antimicrobial polymers globally in recent years. However, as microbes can enter through polymer fissures, mechanical damage to antimicrobial polymers may reduce their protective efficacy. As a result, antimicrobial materials with self-healing capabilities, which allow mechanical damage to be repaired on its own, have higher dependability and a longer lifespan [3]. Commercialized cationic antibacterial compounds like poly(ethylene imine) (PEI) and cetyltrimethylammonium bromide are some of the substances that may be blended with polymers to enhance their antimicrobial capabilities (CTAB)[3]. Some other antimicrobial peptides that can be used due to their cationic properties based on their structure includes;  $\alpha$  – helical,  $\beta$  – sheet, or cyclic [4]. In conclusion, hybrid antimicrobial nanostructures or films can act as antimicrobials by themselves or deliver bioactive molecules for a variety of applications, including wound dressing, photodynamic antimicrobial therapy, food packing and preservation, and antifouling applications. Antimicrobial polymers can be grafted or self-assembled to inert or non-inert vehicles. [5]

## 7.2 References

- [1] Z. Jiang *et al.*, “A dietary enzyme:  $\alpha$ -methylacyl-CoA racemase/P504S is overexpressed in colon carcinoma,” *Cancer Detect. Prev.*, vol. 27, no. 6, pp. 422–426, 2003, doi: 10.1016/J.CDP.2003.07.003.
- [2] H. Lee *et al.*, “Alpha-Methylacyl-CoA Racemase (AMACR), a Potential New Biomarker for Glioblastoma,” *Front. Oncol.*, vol. 10, no. October, pp. 1–7, 2020, doi: 10.3389/fonc.2020.550673.
- [3] J. Du *et al.*, “Mechanically Robust, Self-Healing, Polymer Blends and Polymer/Small Molecule Blend Materials with High Antibacterial Activity,” *ACS Appl. Mater. Interfaces*, vol. 12, no. 24, pp. 26966–26972, 2020, doi: 10.1021/acsami.0c06591.
- [4] M. Diaz, A. Passi, M. Wilmes, S. Omardien, S. Brul, and S. A. J. Zaat, “Antimicrobial Activity of Cationic Antimicrobial Peptides against Gram-Positives: Current Progress Made in Understanding the Mode of Action and the Response of Bacteria,” *Front. Cell Dev. Biol. / www.frontiersin.org*, vol. 4, p. 111, 2016, doi: 10.3389/fcell.2016.00111.
- [5] A. M. Carmona-Ribeiro, L. Dias, and M. Carrasco, “Cationic Antimicrobial Polymers and Their Assemblies,” *OPEN ACCESS Int. J. Mol. Sci.*, vol. 14, p. 14, 2013, doi: 10.3390/ijms14059906.